

This article has been provided to you by the Information Delivery
Department at the Georgia Tech Library.
Please contact us at 404-894-4511 or delivery@library.gatech.edu if you
have any questions or concerns.

Notice: Warning Concerning Copyright Restrictions

The Copyright Law of the United States (Title 17, United States Code) governs the making of photocopies or other reproductions of copyrighted material.

Under certain conditions specified in the law, libraries and archives are authorized to furnish a photocopy or other reproduction.

This material may be protected by copyright law. Any reproduction or distribution of this material, in any format, may be an infringement of the Copyright Law. This reproduction is not to be "used for any purpose other than private study, scholarship, or research." If a user makes or later uses a photocopy or reproduction for purposes in excess of "Fair Use," that user may be liable for copyright infringement.

PURDUE UNIVERSITY
GRADUATE SCHOOL
Thesis Acceptance

This is to certify that the thesis prepared

By Sayed Hasan

Entitled

Electron Phonon Interaction in Carbon Nanotube Devices

Complies with University regulations and meets the standards of the Graduate School for originality and quality

For the degree of Doctor of Philosophy

Final examining committee members

Mark S. Lundstrom

, Chair

Muhammad Alam

Supriyo Datta

Ronald Reifenberger

Approved by Major Professor(s): Mark S. Lundstrom

Approved by Head of Graduate Program: Mark J. Smith

Date of Graduate Program Head's Approval: 01/08/2007

ELECTRON PHONON INTERACTION IN CARBON NANOTUBE DEVICES

A Thesis

Submitted to the Faculty

of

Purdue University

by

Sayed Hasan

In Partial Fulfillment of the

Requirements for the Degree

of

Doctor of Philosophy

May 2007

Purdue University

West Lafayette, Indiana

UMI Number: 3287193



UMI Microform 3287193

Copyright 2008 by ProQuest Information and Learning Company.
All rights reserved. This microform edition is protected against
unauthorized copying under Title 17, United States Code.

ProQuest Information and Learning Company
300 North Zeeb Road
P.O. Box 1346
Ann Arbor, MI 48106-1346

To my lovely wife Rimjheem.

ACKNOWLEDGMENTS

I would like to express my deepest gratitude to my thesis advisor, Professor Mark S. Lundstrom, for his continuous support, invaluable advice, critical and constructive evaluation towards this research. Without his active involvement this work wouldn't have been possible. His uncompromising attitude towards quality and professionalism helped me become a professional from a student. His kindness and considerateness to students helped me pass through some of the most difficult times during my study. Above all, he brought me to the world of cutting edge research, provided the necessary resources and connections and gave me the chance to work with some of the brilliant minds of the world. He is a remarkable person and I have truly benefited from working with him. I am also indebted to my co-advisor Professor Muhammad A. Alam. Professor Alam has this remarkable ability to simplify a complex problem into manageable segments, which helped me overcome some of the very difficult problems during my research. His warm and welcoming attitude towards his students helped me achieve more. I would also like to thank my committee members Professor Supriyo Datta, and Professor Ron Reifenberger, for kindly agreeing to be in my committee in the midst of their busy schedule. I would also like to add that, Professor Lundstrom and Professor Datta are two of my most favorite teachers, whom I always idolized.

My group and lab mates add endless joy to my Purdue memory. Brilliant, resourceful and witty, each of them are the very best students of their countries. In particular I would like to thank, Dr. Ramesh Venugopal, Dr. Anisur Rahman, Dr. Jung Hoon Rhew, Prof. Jing Guo, Dr. Jing Wang, Siyu Koswatta, Neophytos Neophytou, Yang Lui, Raseong Kim, Himadri Pal, Yunfei Gao, Sayeef Salahuddin, Lutfe Siddique, and Dr. Albert Liang. Special thanks goes to Kurtis Cantley for kindly proof-reading this thesis. I would also like to thank Dr. Diego Kinely, and Prof. Mani Vaidyanathan with whom I have had many technical discussions. Prof. Vaidyanathan

helped me sort out many of the issues of the AC response and Monte Carlo simulations.

I would also like to thank Dr. Dmitri Nikonov from Intel Corporation for insightful comments and critiques in the development of the electron phonon coupling calculations in CNTs and Dr. Eric Pop from Intel Corporation who provided some of the metallic tube data and shared valuable insight on electro-thermal transport. I also acknowledge Intel Corporation and the NSF funded Network for Computational Nanotechnology (NCN) for funding this research.

I would also like to express my appreciation to my beloved wife, my parents, my sister, and my daughter. My father's endless inspiration at the early part of my study helped me dream big and eventually obtain the highest degree in academia. This work hadn't been possible without the sacrifice and tremendous support of my lovely wife. During the course of my Ph.D., I have been immersed into my studies, while my wife quietly took care of everything and selflessly supported me. No language can express my gratefulness to her. Finally, I would like to thank my little daughter, many nights she had to play alone, because her daddy was busy with coding.

TABLE OF CONTENTS

	Page
LIST OF TABLES	ix
LIST OF FIGURES	x
ABSTRACT	xvii
1 INTRODUCTION	1
1.1 Overview	1
1.2 Simulation approach	3
1.2.1 The flowchart	3
1.2.2 Boltzmann Transport Equations	4
1.2.3 Collision integral and Phonon generation rate	5
1.2.4 Heat equation	7
1.3 Organization of the thesis	8
2 PHONONS AND ELECTRON-PHONON INTERACTION IN CARBON NANOTUBES	9
2.1 Introduction	9
2.2 Atomic Coordinates	10
2.2.1 Armchair tube	10
2.2.2 Zigzag tube	10
2.3 Electron States	13
2.4 Phonon States	13
2.5 Phonon Dispersion	14
2.5.1 Armchair tube	16
2.5.2 Zigzag tube	19
2.6 Electron phonon coupling	22
2.6.1 Interaction potential	22

	Page
2.6.2 Armchair tube	26
2.6.3 Zigzag tube	30
2.7 Summary	33
3 BTE SIMULATION OF COUPLED ELECTRON PHONON TRANSPORT IN CARBON NANOTUBES	34
3.1 Introduction	34
3.2 Simulation approach	35
3.3 Electron transport	35
3.3.1 Bandstructure	37
3.3.2 Free flight operator	37
3.3.3 Boundary conditions	41
3.3.4 Collision integral	42
3.4 Phonon transport	44
3.4.1 Free flight	46
3.4.2 Generation rate	46
3.4.3 Phonon relaxation	48
3.5 Power flow and heat equation	49
3.6 Summary	52
4 HOT PHONON EFFECT IN METALLIC CARBON NANOTUBES	53
4.1 Introduction	53
4.2 Bandstructure of the metallic tube	55
4.3 Electron phonon scattering	55
4.3.1 Twiston mode	59
4.3.2 LO mode	59
4.3.3 TO mode	59
4.4 Transport equations for electron, phonon and heat	60
4.5 Transport in metallic CNTs on substrate	63
4.5.1 Hot phonon effect	63

	Page
4.6 Transport in suspended metallic tubes	64
4.6.1 Origin of NDR	64
4.7 Self-heating of the tube	69
4.8 Summary	74
5 SIMULATION OF CARBON NANOTUBE MOSFETS INCLUDING HOT- PHONON AND SELF-HEATING EFFECTS	75
5.1 Introduction	75
5.2 Scattering in zigzag tubes	75
5.2.1 Bandstructure	75
5.2.2 Scattering rates	78
5.3 Simulation approach	78
5.4 Comparison with experiment	80
5.5 DC Characteristics of CNT MOSFETs	80
5.5.1 Hot phonon effect on Drain current	80
5.5.2 Self heating and hot spot	82
5.6 AC Characteristics	84
5.7 Summary	85
6 CONCLUSION AND FUTURE WORK	87
6.1 Summary	87
6.2 Future work	88
LIST OF REFERENCES	90
A CALCULATION OF DYNAMICAL MATRIX	97
A.1 Bond Triplets	97
A.1.1 Armchair tube	97
A.1.2 Zigzag tube	104
A.2 Bond Deformation	109
A.3 Potential Energy	110
A.3.1 Ring 1, 3, 4	110

	Page
A.3.2 Ring 2	111
A.4 Dynamical Matrix	112
A.5 Phonon Dispersion	112
VITA	114

LIST OF TABLES

Table	Page
2.1 Force constants of carbon nanotube. Values are given in N/m. These values are similar to Saito's only that $K_{4,t} = 11.34N/m$ instead of $K_{4,t} = 22.9N/m$. This value ensures the rotational symmetry of the nanotube, which requires that $\sum_{n=1\cdots 4} K_{n,t} = 0$. [67].	15

LIST OF FIGURES

Figure	Page
1.1 (a) Flowchart of the simulation scheme. Electron and phonon BTE, and Poisson equation are solved until steady-state is reached. Steady-state power density, IdV/dx is then used to calculate new T from heat equation, and the whole procedure is repeated until steady-state is reached. (b) Device structure of an ideal CNT MOSFET. Doped source (S) and drain (D) has been assumed. Here, L_G is the Channel length, and, L_{SD} is the S/D extension length. Metal gate is used with workfunction 4.7eV and a 3nm thick HfO_2 gate dielectric ($\epsilon = 16$) is also assumed.	3
1.2 The 4 in-scattering and 4 out-scattering processes. (a) In-scattering, (b) out-scattering.	6
2.1 Upper panel shows an unrolled (n, n) armchair tube in the (y, z) plane. Lower panel shows the rolled tube in the (x, y) plane. Here $\theta_1 = 2\theta_2 = 2\pi/3n$, $\mathbf{a}_1 = \sqrt{3}a (\cos \frac{\pi}{6}\hat{\mathbf{y}} + \sin \frac{\pi}{6}\hat{\mathbf{z}})$, $\mathbf{a}_2 = 3a\hat{\mathbf{y}}$, and $a = 1.42 \times 10^{-10}m$. . .	11
2.2 Upper panel: unrolled $(n, 0)$ tube in the (y, z) . Lower panel: the rolled tube in the (x, y) plane. Here, $\theta_z = 2\pi/n$, $\mathbf{a}_1 = \sqrt{3}a (\cos \frac{\pi}{3}\hat{\mathbf{y}} + \sin \frac{\pi}{3}\hat{\mathbf{z}})$, $\mathbf{a}_2 = \sqrt{3}a\hat{\mathbf{y}}$, and $a = 1.42 \times 10^{-10}m$	12
2.3 Atom A and its 4 nearest neighbors (4NN). Each NN is shown by a circle, thus on 1NN, there are 3 B atoms, and on 2NN, 3NN, 4NN, there are 6 A, 3 B, 6 B atoms respectively. A set of three force-constants are defined on each NN ring. These are for motion along the bond stretching (K_ℓ), and for in-plane (K_t), and out of plane transverse motions (K_o).	15
2.4 k-space of (a) armchair, and (b) zigzag tube. The dashed rectangle is the Brillouine zone (BZ). For an armchair tube, the zone boundary is at $\pm 3k_0/4$, and for a zigzag tube, it is at $\pm \sqrt{3}k_0/4$. Where, $k_0 = 4\pi/3\sqrt{3}a$, $a = 1.42 \times 10^{-10}m$	16
2.5 Phonon dispersion of (10,10) armchair tube. (a) All subbands, (b) first three subbands. Here, $k_0 = 4\pi/3\sqrt{3}a$, and $a = 1.42 \times 10^{-10}m$	17

Figure	Page
2.6	Top panel shows the phonon dispersion of a (10,10) armchair tube. Each of the bottom panel shows the eigenvectors of the corresponding phonon branch. For example, the eigenvectors of branch (d) is shown in lower panel (d). From these plots we make the following assignment to the phonon branches: (a)-LA, (b)-TW, (c)-RBM, (d)-oRBM, (e)-TO, (f)-LO. Note that all phonon branches have pure polarization at the Γ point. Here, k_0 is the graphene zone boundary $= 4\pi/3\sqrt{3}a$ 18
2.7	Phonon dispersion of (10,0) zigzag tube. (a) All subbands, (b) first three subbands. Note, the second branch of $\beta = 0$ subband (twiston mode), does not go to zero at Γ point. This is due to the use of graphene-force constants, which are obtained by fitting planar graphene data [65]. . . . 19
2.8	Top panel shows the phonon dispersion of a (13,0) zigzag tube for $\beta = 0$ phonon subband. This subband is responsible for intraband scattering in zigzag tubes. (a)-(f) shows phonon eigenvectors of phonon branches (a)-(f) respectively. At Γ point, all the phonon branches have pure polarization. Thus the following assignment is meaningful: (a)-LA, (b)-TW, (c)-RBM, (d)-oRBM, (d)-TO, and (f)-LO. 20
2.9	Top: phonon dispersion of (13,0) tube for $\beta = 13$ phonon subband. This subband is responsible for the zone-boundary scattering in zigzag tubes. No unambiguous labeling of the phonon branches based on their Γ point polarization is not possible for this subband. 21
2.10	(a) Phonon modes of (10,10) armchair tube for $\beta = 0$ subband. (b) Intra-band matrix elements for various ‘pure’ polarizations. (c) Inter-band matrix elements for various ‘pure’ polarizations. (d) Inter-band matrix elements due to the 6 phonon branches shown in (a), and (e) inter-band matrix elements due to these phonon branches. 27
2.11	(a) inter-band scattering, (b) intra-band scattering. 28
2.12	Scattering rates for br-2, br-5 and br-6. (a) Γ scattering (emission + absorption) for br-2. Since, br-2 is an acoustic mode both emission and absorptions at room temperature are considered. (b) K scattering for br-2. (c) Γ emission for br-6, (d) K emission for br-6. (e) Γ emission for br-5 and (f) K emission for br-5. Here k is electron wavevector. Final states, k_f and phonon wavevector $q = k_f - k$ are calculated using the electron and phonon dispersion relations according to the selection rule. 29
2.13	(a) Components of intra-band matrix elements with zone center phonon and (b) zone-boundary phonon. 30

Figure	Page
2.14 Phonon modes of (13,0) tube for (a) $\beta = 0$ subband (zone center phonons) and (b) $\beta = \pm 8$ subband (zone boundary phonons). (c) Interaction potential corresponding to phonon branches of (a) and (d) interaction potential due to phonon branches of (b).	31
2.15 Phonon dispersion branches of a (13,0) tube belonging to (a) $n=0$ phonon subband, and (b) $n= 8$ phonon subbands. (c) Total backscattering rates (em + abs) at room temperature. For LA mode both emission and absorption rates contribute, while for all other modes absorption is negligible at 300K.	32
3.1 (a) Flowchart of the simulation scheme. Electron and phonon BTEs, and the Poisson equation are solved until steady-state is reached. Steady-state power density, IdV/dx is then used to calculate new T from heat equation, and the whole procedure is repeated until steady-state is reached. (b) Device structure of an ideal CNT MOSFET. Doped source (S) and drain (D) has been assumed. Here, L_G is the Channel length, and, L_{SD} is the S/D extension length. Metal gate is used with workfunction 4.7eV and a 3nm thick HfO_2 gate dielectric ($\epsilon = 16$) is also assumed.	36
3.2 The lowest subbands ($\alpha = 9, 17$) of a (13,0) zigzag tube. (a) Normalized $E-k$, and (b) velocity plot. Here Fermi velocity, $v_F = 3at/2\hbar = 8.4 \times 10^5 \text{m/s}$, $t = 2.6\text{eV}$, and $k_0 = 4\pi/3\sqrt{3}a \sim 1.7/A$	38
3.3 A finite difference grid used to discretize the Boltzmann transport equation. The big circles on the boundary are outside the simulation domain and serves as boundary condition.	39
3.4 (a) In-scattering processes. Any state k is coupled with 4 states k_1^{em} , k_2^{em} , k_1^{ab} , and k_2^{ab} . The two emission points are the solution to the equation: $E(k) - E(k') + \hbar\omega(k - k') = 0$, and the two absorption points are solution to the equation: $E(k) - E(k') - \hbar\omega(k - k') = 0$. Here, k' is the variable. (b) Out-scattering processes. Here, k_1^{em} and k_2^{em} are the solution to the equation: $E(k') - E(k) - \hbar\omega(k' - k) = 0$ and k_1^{ab} and k_2^{ab} are the solution to the equation: $E(k') - E(k) + \hbar\omega(k' - k) = 0$	43
3.5 Phonon dispersion branches of a (13,0) tube belonging to (a) $n=0$ phonon subband, and (b) $n= 8$ phonon subbands. (c) Total backscattering rates (em + abs) at room temperature. For LA mode both emission and absorption rates contribute, while for all other modes absorption is negligible at 300K.	45
3.6 Phonon mode velocities of (13,0) tube. (a) For subband $\beta = 0$, and (b) for $\beta = \pm 8$	47

Figure	Page
3.7 Four end points that are related to phonon wavevector q of a particular phonon branch ν . For emission process, the initial and final states are k_i and $k_i + q$, for absorption process the initial and final states are $-k_i - q$ and $-k_i$. Note that, by determining k_i , which is obtained by solving the equation: $E(k_i + q) - E(k) + \hbar\omega(q) = 0$, all other states can be calculated from there.	48
3.8 Energy flow diagram. Power, VI , flows from battery to the electronic system. Electrons dissipate this power to the optical phonon system by electron-phonon scattering. Optical phonons then breakdown into intermediate-energy phonons and eventually into acoustic phonons. Acoustic phonons, which is nothing but heat, then flows out of the system and the power, VI , flows out as heat flux.	49
3.9 Modified energy flow diagram. Power, VI , flows from battery to the electronics to the optical phonons to the heat-equation and then to the environment. The local temperature, $T(x)$, obtained by solving the heat-equation is then fed back to the phonon BTEs.	51
4.1 Upper panel: Metallic band E-k in armchair tube. Here, $k_0 = 1.7 \times 10^{10} m^{-1}$. At the Γ point, conduction band energy is $E_c = -t_0 = -2.6 eV$. Crossing of the conduction and valence bands occur at $k_t = \pm 0.5 k_0$. Lower panel shows the k -space of the armchair tube. The dashed rectangular box is the Brillouine zone (BZ). E-k in the upper panel is drawn over the full range of the BZ.	56
4.2 Phonon dispersion of $n = 0$ phonon subband of a 2nm diameter armchair tube. Solid (dashed) lines have nonzero (zero) EPC. Note that, $q = k_0$ is the graphene Brioulline zone (BZ) boundary, where, $k_0 = 4\pi/3\sqrt{3}a_{cc} = 1.7 \times 10^{10} m^{-1}$. The TW, LO, and TO assignments are valid only near the Γ point, however, we will use these labes to represent the entire branch. .	57
4.3 (a) Inter-band scattering. (b) Intra-band scattering. The emission process involves both the zone-center and zone-boundary phonons, denoted by Γ_{em} and K_{em} respectively. Similarly the absorption process involves Γ_{ab} and K_{ab} processes.	58
4.4 Out scattering rates, $1/\tau(k, k_f)$ for TW, LO and TO branches. For TW and LO branches, inter-band scattering rates are shown (intra-band scattering rates are zero) and for TO branch, intra-band scattering rates are shown (inter-band scattering are zero in this case). These are full-band scattering rate calculation. All the left panels (a), (c), and (e) shows the rates involving Γ phonons and all the right panels show rates involving K phonons. Also, the solid lines are for emission processes, and the dashed lines are for absorption processes.	61

Figure	Page	
4.5	Scattering processes associated with same phonon mode. These are list of all such k_i and k_f sets that give $k_f - k_i = q$, where q is a particular phonon wavevector. In (a) inter-band conduction to valence band processes are shown. Similar processes exist for valence to conduction transition which are not shown here. In (b) intra-band conduction to conduction processes are shown, while similar processes between valence to valence transition exists but not shown here.	62
4.6	Tube on substrate I-V. Solid lines are simulation and symbols are experimental data [47]. (a) Comparison of cold-phonon and hot-phonon simulation, where, solution of only the electron BTE is called the cold-phonon simulation, and solution of the coupled electron-phonon BTE is called the hot-phonon simulation. In (b) simulation result is compared with measured data of various tube lengths. Here, $d = 2nm$, $g = 0.18W/m/K$, and $\tau = 1.5ps, 1.5ps, 2.5ps$ and $2.25ps$ have been used for $L = 85nm, 150nm, 300nm$ and $700nm$ respectively.	65
4.7	(a) Population of TO mode in a $300nm$ long tube at $1V$ bias. $1ps$ phonon lifetime have been assumed here. (b) Phonon distribution at the middle of the tube. Near zone-boundary, at $q = k_0 = 1.7 \times 10^{10}m^{-1}$, population becomes 1.5. (c) Shows the equilibrium population for this branch. Clearly phonon population becomes extremely hot especially near the contacts as is shown in (a).	66
4.8	Origin of NDR. (i) shows the I-V with the self-heating effect only. Here $\kappa_0 = 2800 W/m/K$, $d = 2nm$, $\tau = 0$ and $m = 2$ have been used. (ii) Similar calculation as (i) except $\kappa_0 = 2000 W/m/K$ has been used. (iii) Both self-heating and hot-phonon are present with. Parameters are similar as (i) except, $\tau = 2.25ps$	68
4.9	Simulation of suspended tubes of various lengths. Symbols are experimental data [80], solid lines are simulation. Following parameters are used for the simulation: $d = 2nm, 2nm$, and $3nm$ for $L = 2.1\mu m, 3\mu m$ and $11\mu m$ tube. In all cases, $\tau = 2.25ps$, $\kappa_0 = 2800 W/m/K$, and $m = 2$ have been used.	69
4.10	Burning bias vs. tube length. Symbols are measured data [81], solid line is simulation. Value of thermal coupling parameter, g is extracted to be $0.18 W/m/K$	72

Figure	Page
4.11 (a) Temperature profile of 700nm on-substrate (solid line) and suspended (dashed line) tube at a fixed power input of $20\mu W$. (b) Scaling of peak temperature with length at various input power. Solid lines are for on-substrate tubes, and the dashed line is for suspended tube with $20\mu W$ power input. In all cases, $m = 1$ has been used in the heat equation (Eq. 4.10).	72
4.12 Effect of thermal conductivity exponent. The top dashed lines are with $m = 1$ and the solid line is with $m = 2$. Symbols are experimental data.	73
5.1 First subband of a (13,0) tube is doubly degenerate and corresponds to subband indices are $m = 9$ and 17. Four possible scattering mechanisms, fs_{ab} , fs_{em} , bs_{ab} , and bs_{em} are shown.	76
5.2 Phonon dispersion branches of a (13,0) tube belonging to (a) $n=0$ phonon subband, and (b) $n=8$ phonon subbands. (c) Total backscattering rates ($bs_{em} + bs_{ab}$) at room temperature. For LA mode both emission and absorption rates contribute, while for all other modes absorption is negligible at 300K.	77
5.3 (a) Flowchart of the simulation scheme. Electron and phonon BTE, and Poisson equation are solved until steady-state is reached. Steady-state power density, IdV/dx is then used to calculate new T from heat equation, and the whole procedure is repeated until steady-state is reached. (b) Device structure of an ideal CNT MOSFET. Doped source (S) and drain (D) of doping $10^9/m$ 1 has been assumed which corresponds to ~ 1 dopants in every 100 carbon atoms. Channel length, L_G , and S/D extension lengths, L_{SD} are 20nm. Metal gate is used with workfunction 4.7eV and a 3nm thick HfO_2 gate dielectric ($\epsilon = 16$) is also assumed.	79
5.4 (a) Bias needed to burn (V_{BD}) for metallic tube at different tube lengths. Symbols show experimental data from [81], and solid line is simulation assuming, $\tau = 3ps$, $g = 0.18W/m/K$. (b) I-V simulation for a 300nm long metallic tube. Symbols are measured data from [47], solid lines are simulation. Equilibrium phonon simulation is done assuming equilibrium phonon population at 300K, which results in unrealistically high current. For hot phonon simulation phonon decay time τ , is used as fitting parameter, and the best fit is obtained for $\tau = 3ps$ [78]	81
5.5 (a) Ballisticity with η . Ballisticity gradually reduces with increasesing value of η and at $V_{GS} = 0.5V$ for which $\eta = 110meV$ ballisticity = 77%. (b) shows the output characteristics with scattering. The upper curve is ballistic, the middle one is with scattering assuming equilibrium phonons, and the lower one is with hot-phonons. At $V_{ds}=0.5V$, ballisticity becomes 77% with equilibrium phonons, and 67% with hot-phonons.	83

Figure	Page
5.6 Temperature profile along the tube. Gate voltage is fixed at $V_{gs}=0.5V$, and drain voltage is varied from 0-0.5V, with a step of 0.055V. Peak temperature occurs near drain channel junction where maximum voltage drop occurs. Inset shows the variation of quasi-fermi level, note that maximum voltage drop occurs near the drain-channel junction.	84
5.7 Step response corresponding to a 100mV gate pulse under $V_{GS} = 0.5V$, $V_{DS} = 0.5V$ condition. Ballistic, equilibrium phonon, and hot phonon cases are considered separately.	86
5.8 Step response of the transconductance. Step calculated using the method of Hockney et al. [87]. The top curve is under ballistic transport, the middle one is with equilibrium phonon scattering and the bottom one is with hot-phonon scattering. The dashed line shows the idealized input admittance with frequency.	86
A.1 Upper panel shows an unrolled (n, n) armchair tube in the (y, z) plane. Lower panel shows the rolled tube in the (x, y) plane. Here $\theta_1 = 2\theta_2 = 2\pi/3n$, $\mathbf{a}_1 = \sqrt{3}a \left(\cos \frac{\pi}{6} \hat{\mathbf{y}} + \sin \frac{\pi}{6} \hat{\mathbf{z}} \right)$, $\mathbf{a}_2 = 3a \hat{\mathbf{y}}$, and $a = 1.42 \times 10^{-10}m$. . .	98
A.2 (a) If atom B_n creates θ_n angle with the x axis, then the associate bond creates, $\pi/2 + \theta_n/2$ angle with the x axis. Thus the x and y components of the bond are proportional to, $- \sin \theta_n/2 $ and $\text{sign}(\theta_n) \cos \theta_n/2$. The $\hat{\mathbf{O}}$ direction makes an angle of $\theta_n/2$ thus its components are: $(\cos \theta_n/2, \sin \theta_n/2, 0)$. (b) Shows the bond from a different angle.	99
A.3 Upper panel: unrolled $(n, 0)$ tube in the (y, z) . Lower panel: the rolled tube in the (x, y) plane. Here, $\theta_z = 2\pi/n$, $\mathbf{a}_1 = \sqrt{3}a \left(\cos \frac{\pi}{3} \hat{\mathbf{y}} + \sin \frac{\pi}{3} \hat{\mathbf{z}} \right)$, $\mathbf{a}_2 = \sqrt{3}a \hat{\mathbf{y}}$, and $a = 1.42 \times 10^{-10}m$	104

ABSTRACT

Hasan, Sayed Ph.D., Purdue University, May, 2007. Electron Phonon Interaction in Carbon Nanotube Devices. Major Professors: Mark S. Lundstrom and Muhammad A. Alam.

With the end of silicon technology scaling in sight, there has been a lot of interest in alternate novel channel materials and device geometry. Carbon nanotubes, the ultimate one-dimensional (1D) wire, is one such possibility. Since the report of the first CNT transistors, lots has been learned about CNT device physics, their scaling properties, and their advantage and disadvantages as a technology. Most of the analysis, however, treats the nanotube as a ballistic device or use some simplified form of phonon scattering. It is an experimental fact that phonon scattering is particularly strong in CNTs, yet every attempt to explain the experimental I-V using the theoretically calculated electron-phonon scattering rates has failed. In this work, we show that experimental I-V can be reproduced if the non-equilibrium phonon population is considered.

In the first part of this work, a simple yet reasonably accurate method to calculate electron phonon scattering rates over the full band is developed, along with a direct solution scheme of the coupled electron-phonon Boltzmann transport equations (BTE). This coupled transport model is then applied to the study of metallic single walled carbon nanotubes, both supported on a solid substrate and suspended over a trench. It is shown that for on-substrate tubes, the current saturation at high bias is the result of the significant build up of optical phonons, which is captured by the phonon BTE. For suspended tubes, there is the additional self-heating effect which is responsible for the negative differential resistance (NDR).

After showing the importance of hot-phonon and self-heating effects in metallic tubes and the success of the calculated scattering rates, this model is then applied to the assessment of CNT-MOSFETs. It is found that the self-heating does not play an important role in a single tube CNT-MOSFETs, but that hot-phonons have a significant effect, both on DC and AC characteristics.

1. INTRODUCTION

1.1 Overview

The success of the microelectronics industry has been the success of Moore's law [1], according to which number of transistors on a microprocessor chip doubles every 18 months. The continuous scaling of transistors lead us to the nanoelectronics regime, where their performance is starting to be limited by the device physics [2, 3]. It is estimated that after 2020, the conventional Silicon technology will face a tough challenge to sustain it's scaling trend [4] and some challenges are already formidable. In order to sustain Moore's law, unconventional device geometry or different channel materials are being actively pursued, Carbon nanotubes (CNTs) are one such example [5–10].

Carbon nanotubes are molecular carbon cylinders with very high mobility [11]. The first transistor using CNTs appeared in 1998 [12, 13]; since then progress in the field of CNT based field effect transistors (CNTFET) has been rapid, both in understanding the device physics [6, 14–20], and in fabrication [21–27]. At the same time, many theoretical works have been done to assess the DC [28–30] and AC [31–38] performance of CNTFETs. All these early works assumed a ballistic transport (which is appropriate for very short channel devices) for simplicity. In real devices, scattering should be present, and the potential of CNTFETs should be re-evaluated including the effect of scattering. The surface of CNT should be more regular than conventional Si surface, hence surface roughness scattering is expected to be minimal. Phonon and impurity scattering are the main source of scattering. In this work, we concentrate on phonon scattering in CNTs. At room temperature, the resistivity at low bias is believed to be due to acoustic phonon scattering [39], which has mean free path of the order of microns. More experimental and theoretical work done by other groups also

confirm this [40–45]. At high bias, on the other hand, current saturation is observed in long ($L \geq 1\mu$) metallic tubes [46]. This is attributed to the high energy scattering by optical phonons, with an extracted mean free path of $\sim 10nm$. Later Javey et al. [47] and Park et al. [48] also found such a small optical phonon mean free path at high bias. Theoretical calculation done by various groups [48–50], however, found optical phonon mean free paths which are at least an order of magnitude longer than the experiment. Thus CNTs have weak acoustic phonon scattering but a very strong optical phonon scattering under high bias.

To see the effect of phonon scattering on electronic transport in semiconducting tubes, Pennington et al. [51–53] did Monte Carlo (MC) simulation of bulk CNTs (here, bulk simulation means neglecting the spatial derivative term in electron BTE). The scattering rates are calculated using a continuum model as in [45]. A similar study was reported by Perebeinos et al. [54], where they used tight binding theory to calculate the scattering rates. The effect of the radial breathing mode (RBM) on transport is reported by Verma et al. [55]. They also reported their version of MC [56] including the RBM mode, and the continuum theory based scattering rate calculation. All of these works assume a bulk tube thus are not directly applicable to CNT based devices. Study of phonon scattering in CNTFETs is reported in [57–59] and shows that although electron optical phonons have a strong coupling, the optical phonon scattering does not have significant effect on on-current at moderate gate-biases due to electrostatic barrier at the channel drain side. This explains why very short nanotubes show near ballistic transport [60]. All these previous works either used theoretically calculated scattering rates, which cannot reproduce the experimental data, or used experimentally observed very short optical phonon mean free paths without explaining why they are so short.

In this work, we first try to explain the discrepancy between the theoretically calculated optical phonon mean free path (mfp) and the experimentally observed value. It is shown that when the non equilibrium phonon population and the heating of the tube are included in the transport calculation, the measured data can be reproduced

remarkably well using the calculated scattering rates. A simple yet accurate tight binding method to calculate the scattering rates over the full-band in armchair and zigzag tubes are also provided. After showing that hot-phonon and self-heating effects can be important in metallic tubes, their effect is then evaluated on the performance of CNT MOSFETs.

1.2 Simulation approach

1.2.1 The flowchart

Figure 1.1 shows the simulation scheme and the device geometry for semiconducting tubes. For a metallic tube, we do not need to solve the Poisson equation because the electric field in the metallic tube does not vary with position. Starting with an

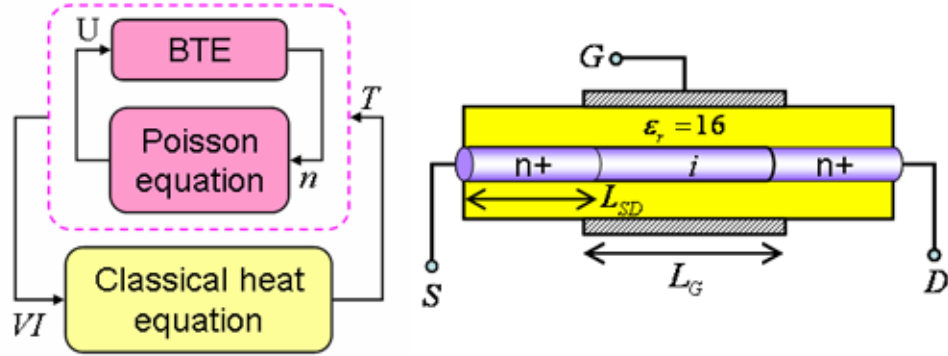


Fig. 1.1. (a) Flowchart of the simulation scheme. Electron and phonon BTE, and Poisson equation are solved until steady-state is reached. Steady-state power density, IdV/dx is then used to calculate new T from heat equation, and the whole procedure is repeated until steady-state is reached. (b) Device structure of an ideal CNT MOSFET. Doped source (S) and drain (D) has been assumed. Here, L_G is the Channel length, and, L_{SD} is the S/D extension length. Metal gate is used with workfunction 4.7eV and a 3nm thick HfO_2 gate dielectric ($\epsilon = 16$) is also assumed.

initial guess for temperature profile and potential profile, the coupled electron-phonon BTEs are first solved. Electron and phonon BTE are coupled because the electron-

phonon scattering rate depends on phonon population while the phonon generation rate depends on electron-phonon scattering. After time step dt a new electron distribution function f , phonon distribution n_ν of branch ν and electron density $n(x)$ are obtained. Using the new $n(x)$ the Poisson equation is solved in cylindrical coordinates

$$\nabla(\epsilon(r)\nabla)U(r,z) = -q\left(N_D - \frac{\delta(r-r_0)}{2\pi r_0}n(z)\right), \quad (1.1)$$

where, r_0 is the tube radius. Due to the cylindrical symmetry, the potential does not depend on θ . The dielectric constant is assumed to be following

$$\epsilon(r) = \begin{cases} 1, & r < r_0 \\ 16, & r > r_0. \end{cases} \quad (1.2)$$

The solution of the Poisson equation gives the potential profile on the tube surface, $U(r_0, z)$ from which electric field is calculated $\mathcal{E} = -dU(r_0, z)/dz$, which is then used to solve the electron-phonon BTE for another time step dt . The whole process is repeated until steady-state is reached.

1.2.2 Boltzmann Transport Equations

Carrier transport is simulated by solving their respective Boltzmann transport equations (BTEs) for electrons and phonons. If there are 5 phonon branches of interest, one BTE for electron and 5 BTEs for phonon are involved,

$$\partial_t f = -v_k \partial_z f + \frac{q\mathcal{E}}{\hbar} \partial_k f + \hat{C}f \quad (1.3)$$

$$\partial_t n_\nu = -v_\nu \partial_z n_\nu + G_\nu - \frac{n_\nu - n_{0,\nu}(T)}{\tau}, \quad (1.4)$$

where, $\nu = 1, 2 \dots 5$ are the phonon branches of interest, v_k and v_ν are electron and phonon group velocities calculated using their respective dispersion relations, G_ν is the phonon generation rate due to electron phonon scattering, $\hat{C}f$ is the collision integral, and τ is the lifetime of anharmonic phonon decay. The collision integral, $C\hat{f}$, is the sum of individual collision integrals, $\hat{C}_\nu f$, due to each phonon branche

ν . These coupled partial differential equations (PDEs) are solved iteratively in time. Starting with an initial electron and phonon distribution functions, f , n_ν , Eqs. 1.3, 1.4 describe the change in their distribution functions after one time step dt . The updated distribution functions are

$$f(t + dt) = f(t) + \partial_t f dt \quad (1.5)$$

$$n_\nu(t + dt) = n_\nu(t) + \partial_t n_\nu dt. \quad (1.6)$$

Using the updated electronic distribution function, the electron density, $n(z)$ is next calculated as

$$n(z, t) = 4 \int \frac{dk}{2\pi} f(z, k, t), \quad (1.7)$$

where, the pre-factor accounts for 2 fold valley and 2 fold spin degeneracy. Electron density is then put into the Poisson equation to calculate the potential profile and the new electric field and the whole process is iterated until a steady state solution is obtained.

1.2.3 Collision integral and Phonon generation rate

The collision integral used in the BTEs is the net in-scattering rate for occupying a particular phase-space volume due to scattering. Considering Fig. 1.2, we see that for an electron at a particular state, k , there are four out-scattering and 4 in-scattering probabilities. Among these 8 possibilities there are emission as well as absorption processes involved. So the net generation rate is the (total emission - total absorption) rates. All these scattering rates, which are actually the transition probabilities [61] are calculated using Fermi's golden rule. In order to calculate these, the matrix elements for each of these processes are calculated first. The basic principle is very simple, first the phonon modes of armchair and zigzag tubes are calculated using a spring-mass model, which gives the phonon modes and phonon eigenvectors. These phonon eigenvectors are then projected along the bonds to calculate the bond deformations. The scattering potential, which is the transition matrix element, is proportional to

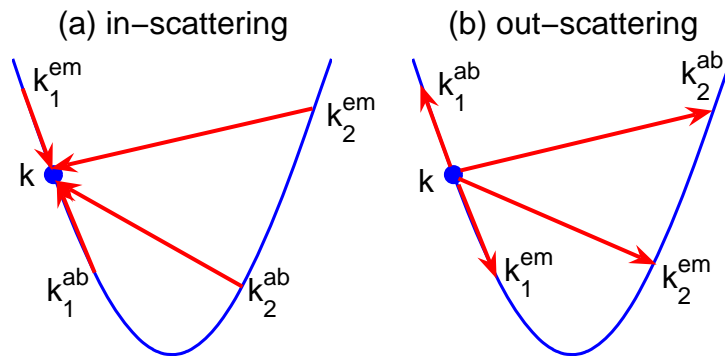


Fig. 1.2. The 4 in-scattering and 4 out-scattering processes. (a) In-scattering, (b) out-scattering.

the bond deformation with the proportionality constant of 5.3 eV/Å [49]. Details of this calculation can be found in Chapter 2.

1.2.4 Heat equation

Finally we solve the classical heat equation to obtain the temperature profile of the device. In phonon BTE (Eq. (1.4)), the third term represents the decay of phonon population due to anharmonic (cubic term in lattice potential) phonon-phonon scattering, and is modeled by a relaxation time approximation (RTA). The alternative to RTA is to use a microscopic theory of phonon-phonon scattering similar to electron-phonon scattering as has been developed in this thesis. The theory of phonon-phonon scattering, however, requires i) the determination of the strength of the anharmonic potential that couples different phonon states, ii) the calculation of phonon-phonon matrix elements, and finally iii) the figuring out the respective phonon branches that are coupled by phonon-phonon scattering. This could be a much harder problem and a thesis problem in itself. In RTA, we assume that the phonon-phonon scattering tend to bring the phonon population towards a Bose-Einstein distribution, which is evaluated at the local temperature. To determine this local temperature, the heat-equation is solved, which is

$$\nabla (A\kappa(T) \nabla T) - g(T - T_0) = -I \frac{-dF_n}{dx}, \quad (1.8)$$

where, the first term is the diffusion term with thermal conductivity, $\kappa(T)$ which varies inversely with temperature, T , the second term is the vertical flow of heat from tube to substrate, with tube-substrate thermal coupling parameter of $g = 0.18 \text{ W/m/K}$, and the right hand side is the Joule heating power density. For metallic tubes, the gradient of quasi-Fermi level is the electric field, $-dF_n/dx = \mathcal{E}$, for semiconducting tubes, the gradient depends on local electron density and is calculated self-consistently with the Poisson equation. Since, κ varies with temperature, the above equation becomes non-linear, and is solved on a finite difference grid iteratively. For a suspended metallic tube on the other hand, the tube-substrate thermal

coupling is approximately zero, $g \approx 0$ (radiation is negligible since it depends on T^4 . Due to convection, g will have some non-zero value but it is much smaller than 0.18 W/m/K and qualitatively it makes no difference) and the resulting heat equation can be solved analytically.

1.3 Organization of the thesis

Here is how the thesis is organized. In chapter 2, the calculation of phonon modes and the electron-phonon matrix elements are discussed. A new method of calculating the phonon modes and a full band electron-phonon coupling calculation is presented along with the scattering rates for semiconducting tubes. Chapter 3 provides a description of the formulation of the electron and phonon Boltzmann transport equations. In chapter 4, the method is applied to the study of metallic single walled carbon nanotubes, both supported on substrate and suspended tubes. Here it has been shown that, the current saturation in long on-substrate metallic tube is due to the hot-phonon effects, and also the negative differential resistance (NDR) in suspended tube is due to the self-heating effect in suspended tube, however, in suspended tube both hot-phonon and self-heating effects are necessary to explain the measured data. Finally in chapter 5, the method is applied to the study of hot-phonon and self-heating effects in CNT-MOSFETs. Chapter 6 summarizes the conclusions and presents recommendation for future work.

2. PHONONS AND ELECTRON-PHONON INTERACTION IN CARBON NANOTUBES

2.1 Introduction

In this chapter, we calculate the electron phonon coupling (EPC) in carbon nanotube (CNT) using Mahan's approach [49]. Mahan's work provides a basic framework for EPC calculation provided the phonon eigenvectors are known. To accurately calculate the EPC over the full band, a method of phonon mode calculation, compatible with the EPC calculation scheme is needed. Hence, a suitable and reasonably accurate method for calculating the phonon dispersion in armchair and zigzag tube has been developed first. For simplicity we concentrate on armchair and zigzag tubes, however, the method can easily be extended to chiral tubes.

In transport calculations, only a few phonon subbands are of interest. A method of phonon mode calculation is required, which can produce the phonon dispersion of a particular phonon subband in question. The zone folding method, developed by Jishi et al. [62] seems suitable for this, but it cannot capture the radial breathing mode (RBM). The force constant method [63], which incorporates nanotube curvature effect into account, can capture the RBM correctly, but it cannot sort out phonon dispersions into subbands. Though they can capture the RBM and give the phonon dispersion of a particular subband, the elastic continuum theory based models [45,64] are also not suitable, since they fail to capture the high-energy optical modes. A suitable phonon dispersion calculation method thus needs to be developed, which is accurate enough to capture the known features of phonon dispersion in CNTs, and provide result of a particular phonon subband of interest. To achieve this, we introduce azimuthal symmetry in Saito's force constant method. This method, which

is as accurate as the force-constant one, is completely compatible with Mahan's EPC calculation scheme.

2.2 Atomic Coordinates

2.2.1 Armchair tube

Figure 2.1 shows an unrolled graphene lattice for an (n, n) armchair tube. Here the unit cell consists of A and B atoms. The 2-D translation vectors are: $\mathbf{R}_{\mathbf{ml}}^{\mathbf{A}} = m\mathbf{a}_2 + l\mathbf{a}_1$, and $\mathbf{R}_{\mathbf{ml}}^{\mathbf{B}} = \mathbf{R}_{\mathbf{ml}}^{\mathbf{A}} + a\hat{\mathbf{y}}$, with \mathbf{a}_1 and \mathbf{a}_2 being the basis vectors (see Fig. 2.1 for definition). Defining $\theta_1 = 2\pi/3n$, and the tube radius, $R = 3na/2\pi$, the cartesian coordinates of these atoms on the nanotube surface become

$$\mathbf{R}_{\mathbf{ml}}^{\mathbf{A}} = [R \cos \theta_{ml}, R \sin \theta_{ml}, cl], \quad (2.1)$$

$$\mathbf{R}_{\mathbf{ml}}^{\mathbf{B}} = [R \cos (\theta_{ml} + \theta_1), R \sin (\theta_{ml} + \theta_1), cl]. \quad (2.2)$$

Here, $\theta_{ml} = 3\theta_1 (m + l/2)$, $c = \sqrt{3}a/2$, and $a = 1.42 \times 10^{-10}m$ is the c-c bonding length in graphene [65]. Figure 2.1 also shows the 18 neighbors of an A atom, and their (m, l) indices.

2.2.2 Zigzag tube

Figure 2.2 shows the graphene lattice for an $(n, 0)$ zigzag tube, with A and B atoms within the unit cell. Here, the 2-D translation vectors are: $\mathbf{R}_{\mathbf{ml}}^{\mathbf{A}} = m\mathbf{a}_2 + l\mathbf{a}_1$ and $\mathbf{R}_{\mathbf{ml}}^{\mathbf{B}} = \mathbf{R}_{\mathbf{ml}}^{\mathbf{A}} + (\mathbf{a}_1 + \mathbf{a}_2)/3$, with $\mathbf{a}_1, \mathbf{a}_2$ being the basis. Defining $\theta_z = 2\pi/n$ and $R = \sqrt{3}na/2\pi$, the atomic coordinates on nanotube surface in cartesian coordinate system become

$$\mathbf{R}_{\mathbf{ml}}^{\mathbf{A}} = [R \cos \theta_{ml}, R \sin \theta_{ml}, cl], \quad (2.3)$$

$$\mathbf{R}_{\mathbf{ml}}^{\mathbf{B}} = [R \cos (\theta_{ml} + \theta_z/2), R \sin (\theta_{ml} + \theta_z/2), cl + a/2], \quad (2.4)$$

where $\theta_{ml} = \theta_z (m + l/2)$ and $c = 3a/2$. The indices, m, l of the 18 nearest neighbors are also shown in Fig. 2.2.

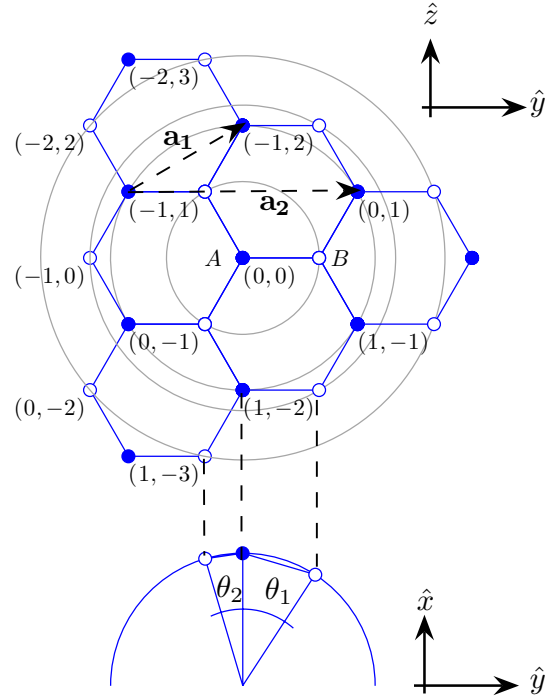


Fig. 2.1. Upper panel shows an unrolled (n, n) armchair tube in the (y, z) plane. Lower panel shows the rolled tube in the (x, y) plane. Here $\theta_1 = 2\theta_2 = 2\pi/3n$, $\mathbf{a}_1 = \sqrt{3}a (\cos \frac{\pi}{6} \hat{y} + \sin \frac{\pi}{6} \hat{z})$, $\mathbf{a}_2 = 3a \hat{y}$, and $a = 1.42 \times 10^{-10} m$.

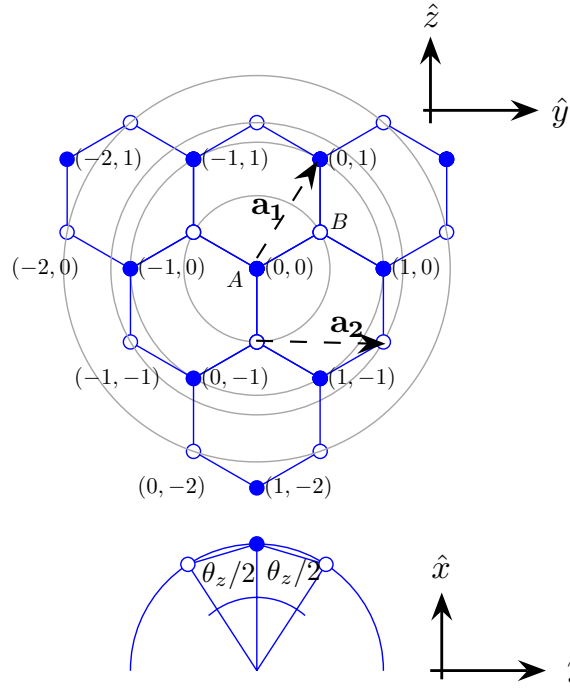


Fig. 2.2. Upper panel: unrolled $(n, 0)$ tube in the (y, z) . Lower panel: the rolled tube in the (x, y) plane. Here, $\theta_z = 2\pi/n$, $\mathbf{a}_1 = \sqrt{3}a (\cos \frac{\pi}{3} \hat{y} + \sin \frac{\pi}{3} \hat{z})$, $\mathbf{a}_2 = \sqrt{3}a \hat{y}$, and $a = 1.42 \times 10^{-10} m$.

2.3 Electron States

The electron in the nanotube can be expressed as

$$C_{A,ml} = \frac{1}{\sqrt{nN}} \sum_{k\alpha} C_{A,k\alpha} e^{i(kcl + \alpha\theta_{ml})}, \quad (2.5)$$

$$C_{B,ml} = \frac{1}{\sqrt{nN}} \sum_{k\alpha} C_{B,k\alpha} e^{i(kcl + \alpha\theta_{ml})} e^{\gamma}, \quad (2.6)$$

where, k is the wavevector, α is the azimuthal quantum number (subband index), γ is the relative phase between A and B atoms, n is the number of unit cells that can fit in the circumference, and N is the number of unit cells per unit length. For armchair tube, $\gamma = \alpha\theta_1$, and for zigzag tube $\gamma = ka/2 + \alpha\theta_z/2$.

2.4 Phonon States

Since the nanotube has cylindrical symmetry (for tube on substrate, the cylindrical symmetry could be broken but in this treatment we ignore this and assume the tube to be isolated), the atomic displacements are expressed in a local cylindrical coordinate system as

$$\mathbf{Q}_{A,ml} = (Q_{A\rho,ml}, Q_{A\theta,ml}, Q_{Az,ml}), \quad (2.7)$$

$$\mathbf{Q}_{B,ml} = (Q_{B\rho,ml}, Q_{B\theta,ml}, Q_{Bz,ml}), \quad (2.8)$$

where, $Q_{A\rho}$, $Q_{A\theta}$, and Q_{Az} are the radial, azimuthal, and axial components. The displacements within an (m, l) unit cell are related to the reference unit-cell at $(0, 0)$ by a phase factor (Bloch's theorem [66])

$$\mathbf{Q}_{A,ml} = \sum_{q\beta} (Q_{A\rho}, Q_{A\theta}, Q_{Az}) e^{i(qcl + \beta\theta_{ml})}, \quad (2.9)$$

$$\mathbf{Q}_{B,ml} = \sum_{q\beta} (Q_{B\rho}, Q_{B\theta}, Q_{Bz}) e^{i(qcl + \beta\theta_{ml})} e^{\gamma}, \quad (2.10)$$

where, q is the phonon wavevector and β is the azimuthal quantum number (phonon subband index) for phonons. Similar to the electronic states, $\gamma = \beta\theta_1$ for armchair

tube and $\gamma = qa/2 + \beta\theta_z/2$ for zigzag tube. Since, these are expressed in local coordinates, the Q_ρ component at different unit cells are pointed along different directions. To transform them into a global cartesian coordinate system we use the following transformation

$$\begin{pmatrix} Q'_x \\ Q'_y \\ Q'_z \end{pmatrix} = \begin{pmatrix} \cos \theta & -\sin \theta & 0 \\ \sin \theta & \cos \theta & 0 \\ 0 & 0 & 1 \end{pmatrix} \begin{pmatrix} Q_\rho \\ Q_\theta \\ Q_z \end{pmatrix}, \quad (2.11)$$

$$Q'_i = U_{ij}(\theta) Q_j, \quad (2.12)$$

where, θ is the azimuthal angle of the atom, whose displacements are being transformed.

2.5 Phonon Dispersion

Phonon dispersion in carbon nanotube is calculated using a spring mass model including interaction upto the fourth nearest neighbors (4NN). For each NN, a set of three force constants are defined characterizing the stretching and bending (in-plane and out-of plane) of the bond as shown in Fig. 2.3. Since there are 4 NNs, a set of 12 force constants are needed, which are obtained from [62,65] as listed in table 2.1. This particular set of force-constants are extracted by fitting the graphene phonon-dispersion data [62], and can predict nanotube Raman intensities with good accuracy [63]. Rotational symmetry in nanotube requires that $\sum_{n=1}^4 K_{n,t} = 0$ [67]. The original force constants [62,63,65] do not have this symmetry. We modified the value of K_t on the 4th ring, (K_{4t}), to enforce this. This modification is somewhat arbitrary, but the phonon dispersion is not too sensitive to this. Previous calculations using this elaborate set of force-constants [63,65], did not utilize the azimuthal symmetry of the tube, and are not suitable to calculate EPC using Mahan's approach. By expressing the forces on A and B atoms in a local cylindrical coordinates, azimuthal symmetry can be incorporated. The resulting phonon mode eigenvectors are then directly usable in the EPC calculation. Details of this can be found in Appendix A.

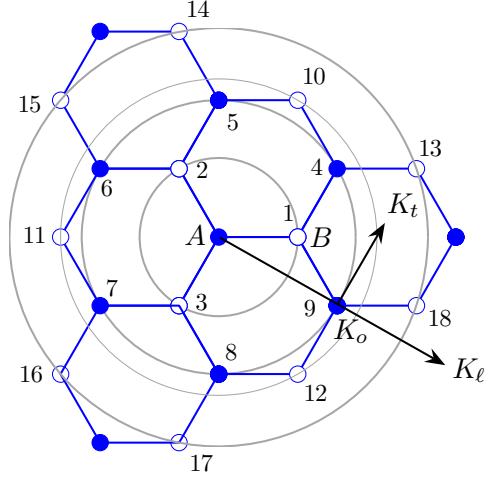


Fig. 2.3. Atom A and its 4 nearest neighbors (4NN). Each NN is shown by a circle, thus on 1NN, there are 3 B atoms, and on 2NN, 3NN, 4NN, there are 6 A, 3 B, 6 B atoms respectively. A set of three force-constants are defined on each NN ring. These are for motion along the bond stretching (K_ℓ), and for in-plane (K_t), and out of plane transverse motions (K_o).

Table 2.1

Force constants of carbon nanotube. Values are given in N/m. These values are similar to Saito's only that $K_{4,t} = 11.34N/m$ instead of $K_{4,t} = 22.9N/m$. This value ensures the rotational symmetry of the nanotube, which requires that $\sum_{n=1 \dots 4} K_{n,t} = 0$. [67].

NN	K_ℓ	K_t	K_o
1	365	245	98.2
2	88	-32.3	-4
3	30	-52.5	1.5
4	-19.2	11.34	-5.8

2.5.1 Armchair tube

Using the above method, the phonon dispersion of a (10,10) armchair tube is calculated. Figure 2.4 shows the Brillouine zone (BZ) of an armchair tube over which the dispersion of all phonon subbands is calculated and shown in Fig. 2.5a. Acoustic modes are shown in Fig. 2.5b. These are exactly the same as one would obtain

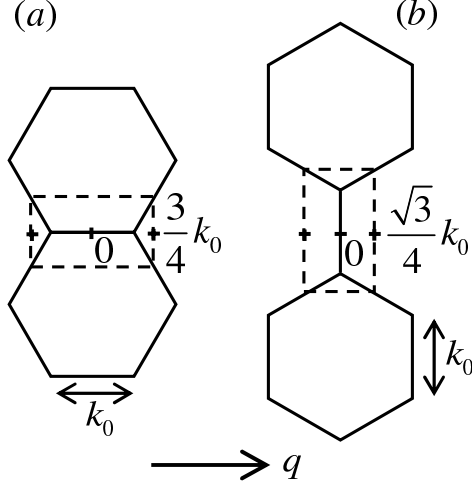


Fig. 2.4. k -space of (a) armchair, and (b) zigzag tube. The dashed rectangle is the Brillouine zone (BZ). For an armchair tube, the zone boundary is at $\pm 3k_0/4$, and for a zigzag tube, it is at $\pm \sqrt{3}k_0/4$. Where, $k_0 = 4\pi/3\sqrt{3}a$, $a = 1.42 \times 10^{-10}m$.

using Saito's method [65]. Within the metallic bands of an armchair tube, only $\beta = 0$ phonon subband contribute to scattering. Phonon dispersion and the polarization of each of its branches are shown in Fig. 2.6. The top panel shows the dispersion, and the 6 bottom panels are the corresponding phonon eigenvectors. Consider branch (a), whose eigenvectors are shown in Fig. 2.6a. Note that, Q_z is the dominant polarization at Γ point for this branch, hence it is called the LA branch. Inspecting the phonon eigenvectors at the Γ point for the rest of the branches, we label branch (b), (c), (d), (e), and (f) as TW, RBM, oRBM, TO, and LO respectively, where, TW is twiston or torsional mode, RBM is radial breathing mode, oRBM is optical RBM etc.

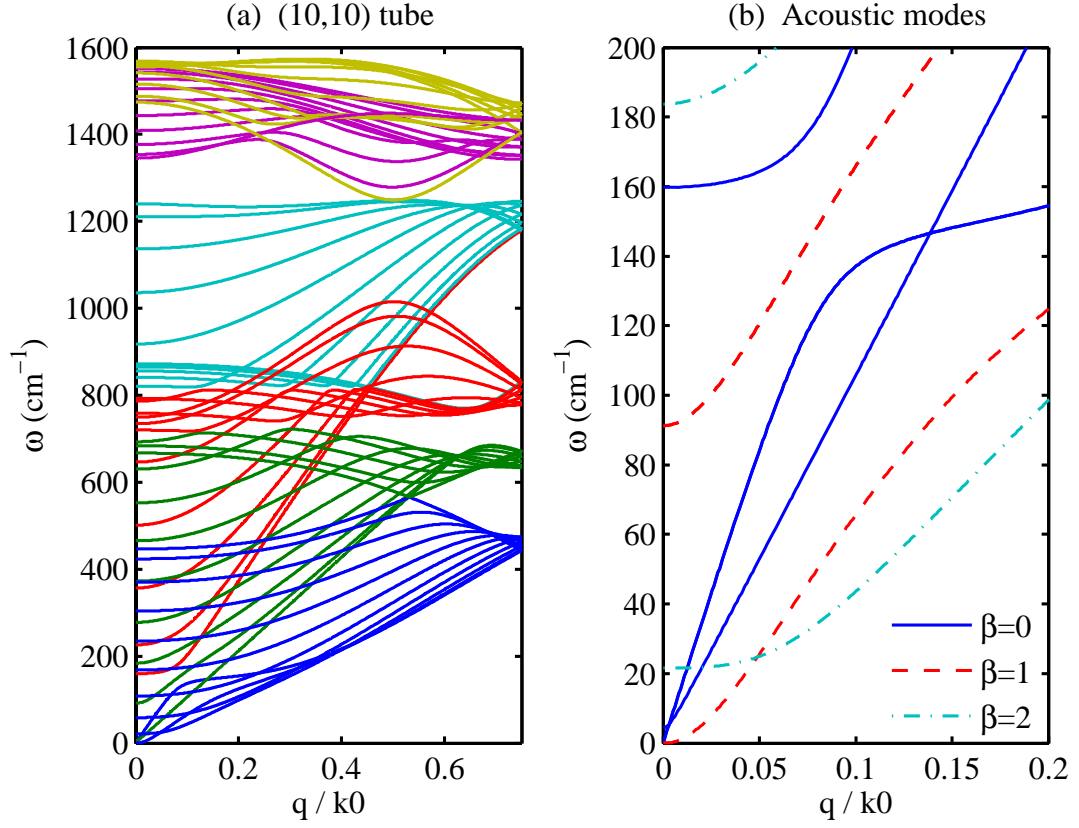


Fig. 2.5. Phonon dispersion of (10,10) armchair tube. (a) All subbands, (b) first three subbands. Here, $k_0 = 4\pi/3\sqrt{3}a$, and $a = 1.42 \times 10^{-10}m$.

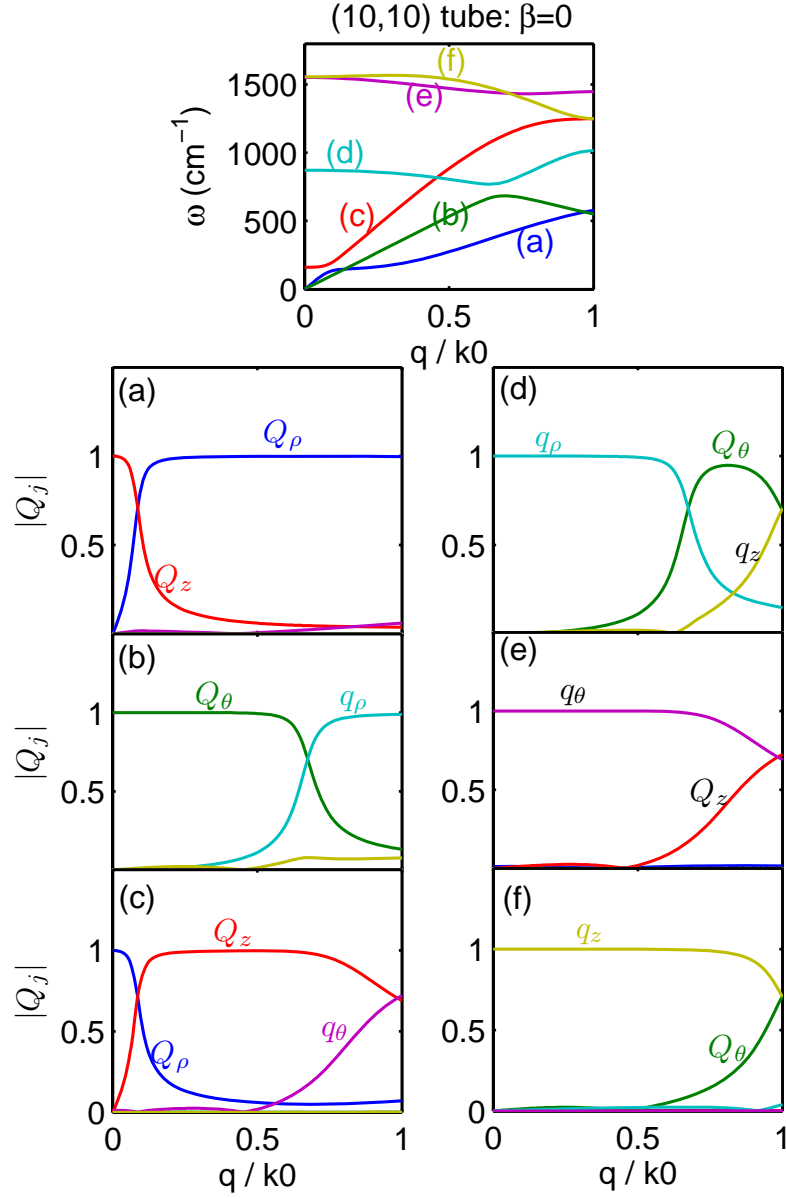


Fig. 2.6. Top panel shows the phonon dispersion of a (10,10) armchair tube. Each of the bottom panel shows the eigenvectors of the corresponding phonon branch. For example, the eigenvectors of branch (d) is shown in lower panel (d). From these plots we make the following assignment to the phonon branches: (a)-LA, (b)-TW, (c)-RBM, (d)-oRBM, (e)-TO, (f)-LO. Note that all phonon branches have pure polarization at the Γ point. Here, k_0 is the graphene zone boundary $= 4\pi/3\sqrt{3}a$.

2.5.2 Zigzag tube

Figure 2.7 shows the phonon dispersion of a (10,0) zigzag tube. Phonon eigenvectors for a (13,0) tube for $\beta = 0$ and $\beta = 8$ are shown in Figs. 2.8, 2.9 respectively. $\beta = 0$ subband gives intra-band scattering while, $\beta = \pm 8$ give zone boundary scatter-

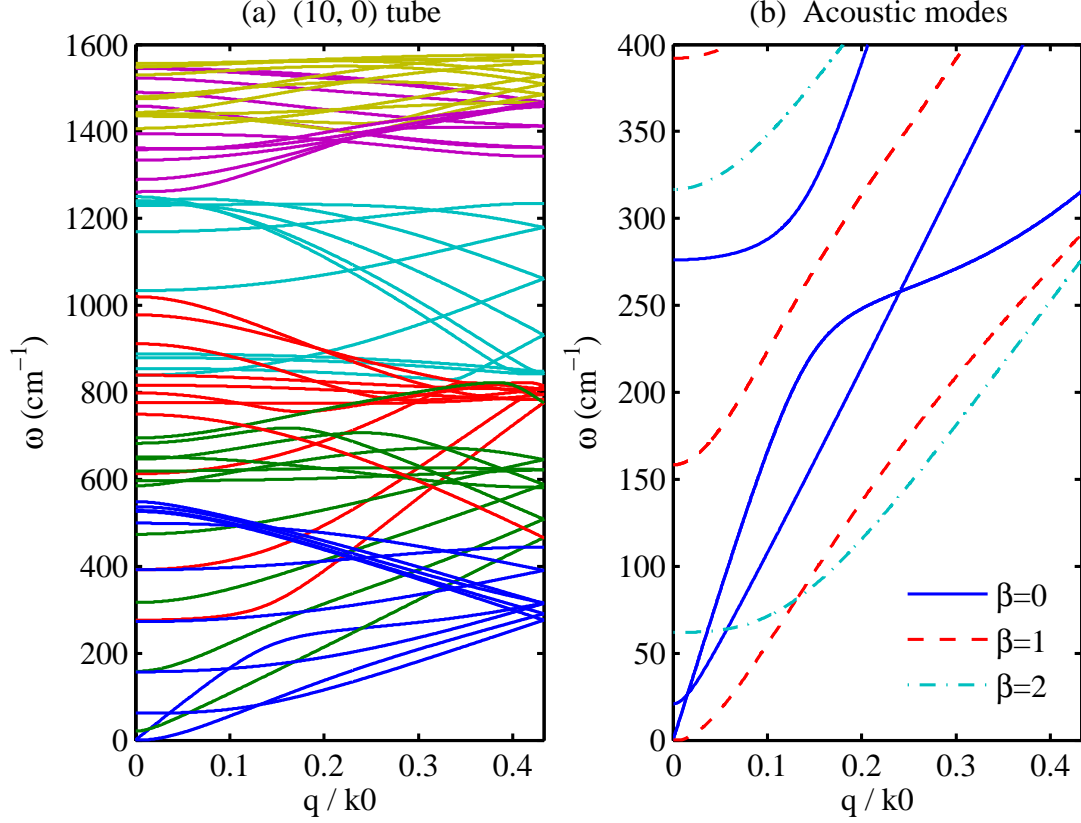


Fig. 2.7. Phonon dispersion of (10,0) zigzag tube. (a) All subbands, (b) first three subbands. Note, the second branch of $\beta = 0$ subband (twistion mode), does not go to zero at Γ point. This is due to the use of graphene-force constants, which are obtained by fitting planar graphene data [65].

ing in a (13,0) zigzag tube. Note that for the $\beta = 0$ subband, phonon eigenvectors at $\Gamma = 0$ point have pure polarization, and labeling of the branches are possible based on the polarization information. For zone boundary phonon, however, eigenvectors

are mixed as shown in in Fig. 2.9. This shows the importance of knowing the phonon eigenvector in order to calculate the electron phonon coupling.

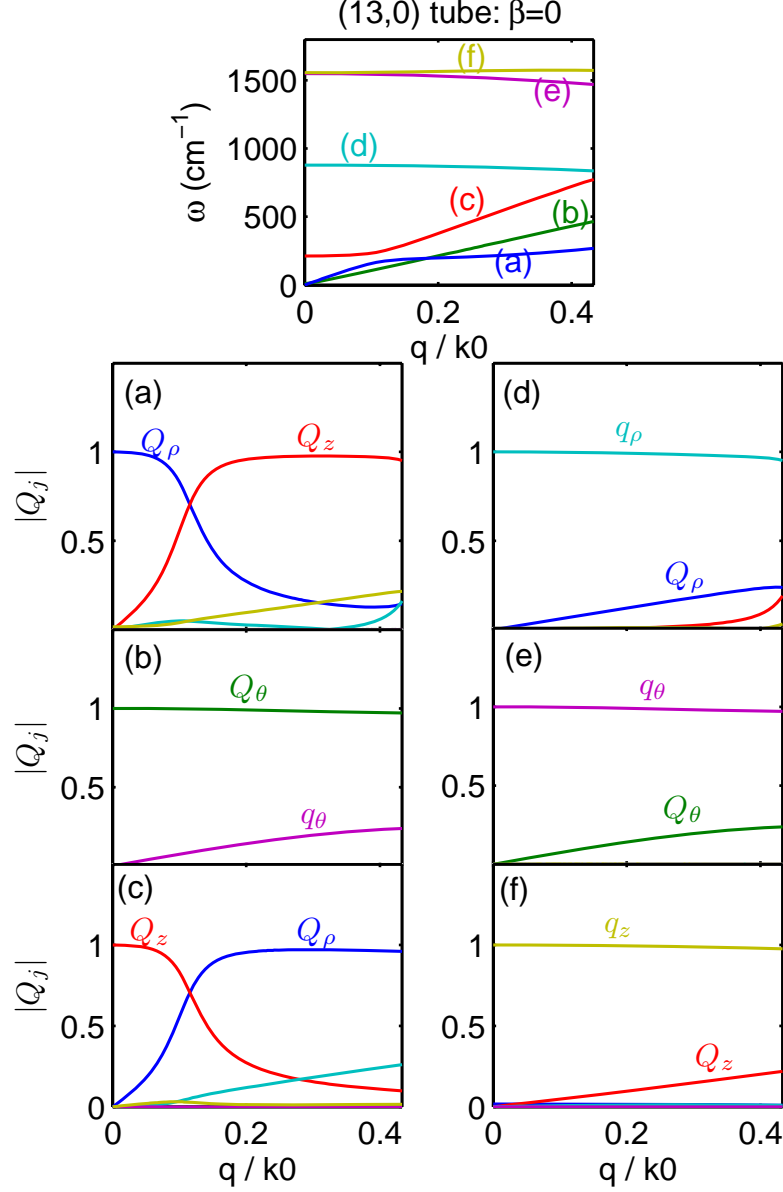


Fig. 2.8. Top panel shows the phonon dispersion of a (13,0) zigzag tube for $\beta = 0$ phonon subband. This subband is responsible for intraband scattering in zigzag tubes. (a)-(f) shows phonon eigenvectors of phonon branches (a)-(f) respectively. At Γ point, all the phonon branches have pure polarization. Thus the following assignment is meaningful: (a)-LA, (b)-TW, (c)-RBM, (d)-oRBM, (d)-TO, and (f)-LO.

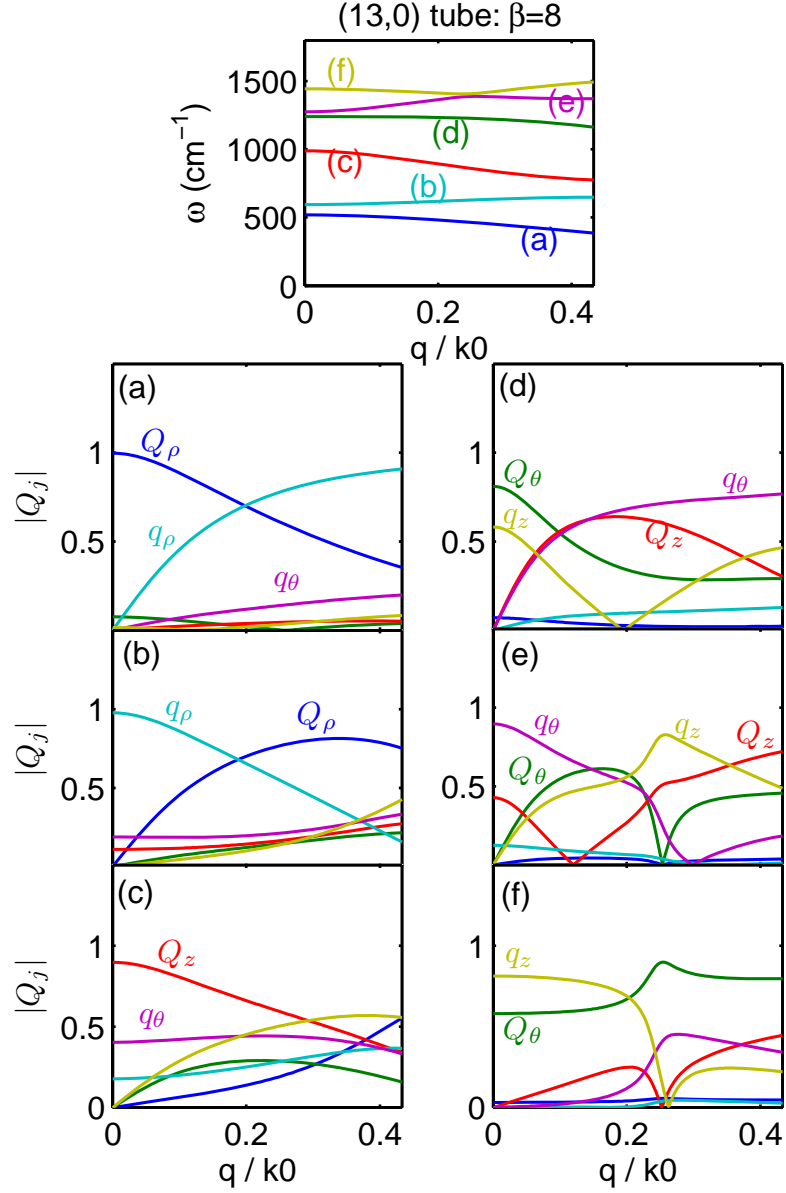


Fig. 2.9. Top: phonon dispersion of (13,0) tube for $\beta = 13$ phonon subband. This subband is responsible for the zone-boundary scattering in zigzag tubes. No unambiguous labeling of the phonon branches based on their Γ point polarization is not possible for this subband.

2.6 Electron phonon coupling

Now that we have calculated the phonon modes and phonon eigenvectors, we are ready to calculate the electron phonon coupling (EPC) of various phonon modes. The electron-phonon interaction is based on the phonon modulation of the hopping interaction. The hopping interaction depends on bond length, which changes due to lattice vibration. As a result of this lattice vibration, change in hopping parameter occur. This change in hopping interaction appears as a scattering potential, which we want to calculate. For small vibration, the change in hopping interaction can be written as: $J(Q) \approx J_0 + J_1 \hat{\ell} \cdot \delta \mathbf{Q}$, [49, 68] where, $\hat{\ell} \cdot \delta \mathbf{Q}$ is the change in bond length due to the relative displacements, $\delta \mathbf{Q}$, of neighboring atoms. Value of J_0 are $\sim 2.4 - 3.1 \text{ eV}$ [49], and we use a value of 2.6 eV [69] in this work. Since, $J_1/J_0 \sim 2 \text{ \AA}^{-1}$ [49, 70] we use $J_1 = 5.3 \text{ eV \AA}^{-1}$.

2.6.1 Interaction potential

Electron phonon interaction potential can be written as

$$V_{ep} = J_1 \sum_{ml\delta} \hat{\ell}_{ml+\delta} \cdot (\mathbf{Q}_{\mathbf{B}, \mathbf{ml}+\delta} - \mathbf{Q}_{\mathbf{A}, \mathbf{ml}}) \left(C_{A,ml}^\dagger C_{B,ml+\delta} + C_{B,ml+\delta}^\dagger C_{A,ml} \right). \quad (2.13)$$

Here, m, l runs through the entire lattice, and for any lattice site, m, l , δ is the displacements to its 1NN atoms, $\hat{\ell}_{ml+\delta}$ are the unit vectors along bonding direction for the first NN ring. Due to the axial symmetry, the result of the above dot product is independent of m, l , except for a phase factor, which the phonon states accumulates due to translation. Thus performing the dot product at the origin we get

$$\hat{\ell}_{ml+\delta} \cdot (\mathbf{Q}_{\mathbf{B}, \mathbf{ml}+\delta} - \mathbf{Q}_{\mathbf{A}, \mathbf{ml}}) = \sum_{q\beta} \hat{\ell}_\delta \cdot (\mathbf{Q}_{\mathbf{B}, \mathbf{q}\beta} e^{i\gamma_\delta} - \mathbf{Q}_{\mathbf{A}, \mathbf{q}\beta}) e^{i(qcl + \beta\theta_{ml})}, \quad (2.14)$$

where, γ_δ is the phase factor of the first NN ring and are defined in Eqs. (A.5) and (A.25). To calculate these phases, we use the phonon wavevector and its azimuthal quantum number, q and β . Similarly for electrons,

$$\begin{aligned} C_{A,ml} &= \frac{1}{\sqrt{nN}} \sum_{k\alpha} C_{A,k\alpha} e^{i(kcl + \alpha\theta_{ml})}, \\ C_{B,ml+\delta} &= \frac{1}{\sqrt{nN}} \sum_{k\alpha} C_{B,k\alpha} e^{i(kcl + \alpha\theta_{ml})} e^{i\beta_\delta}, \end{aligned} \quad (2.15)$$

where, β_δ is obtained by replacing phonon states (q, β) in Eqs. (A.5) or (A.25), with electronic states (k, α) . Substituting Eqs. (2.14) and (2.15) in Eq. (2.13), and carrying out the summation over m, l indices we obtain

$$V_{ep} = J_1 \sum_{k\alpha q\beta} \left(C_{A,k+q,\alpha+\beta}^\dagger C_{B,k,\alpha} M_1 + C_{B,k+q,\alpha+\beta}^\dagger C_{A,k,\alpha} M_2 \right), \quad (2.16)$$

where

$$M_1 = \ell_{1\delta i} (U_{\delta ij} Q_{Bq\beta,j} e^{i\gamma_\delta} - Q_{Aq\beta,j}) e^{i\beta_\delta}, \quad (2.17)$$

$$M_2 = \ell_{1\delta i} (U_{\delta ij} Q_{Bq\beta,j} e^{i\gamma_\delta} - Q_{Aq\beta,j}) e^{-i\beta_\delta} e^{-i\gamma_\delta}, \quad (2.18)$$

here, summation over δ, i , and j indices is assumed. Above summation can be recast as matrix multiplication if we notice that, $\ell_{1\delta i}$ is an element of \mathbf{L}_1 matrix defined by Eqs. (A.2) (for armchair tube)

$$\mathbf{L}_1 = \begin{bmatrix} -\sin\theta_a/2 & \cos\theta_a/2 & 0 \\ -1/2 \sin\theta_a/4 & -1/2 \cos\theta_a/4 & \sqrt{3}/2 \\ -1/2 \sin\theta_a/4 & -1/2 \cos\theta_a/4 & -\sqrt{3}/2 \end{bmatrix}, \quad (2.19)$$

and (A.21) (for zigzag tube)

$$\mathbf{L}_1 = \begin{bmatrix} -\sqrt{3}/2 \sin\theta_z/4 & \sqrt{3}/2 \cos\theta_z/4 & 1/2 \\ -\sqrt{3}/2 \sin\theta_z/4 & -\sqrt{3}/2 \cos\theta_z/4 & 1/2 \\ 0 & 0 & -1 \end{bmatrix}. \quad (2.20)$$

Similarly, $\ell_{1\delta i} U_{\delta i j} = L_{1\delta i} U_{ij}(\theta_{1\delta})$ can be thought of as the δ, j element of a matrix, $\mathbf{\Lambda}_1$. For an armchair tube, with $\theta_a = 2\pi/3/n$, $\mathbf{\Lambda}_1$ becomes

$$\mathbf{\Lambda}_1 = \begin{bmatrix} \sin(\theta_a/2) & \cos(\theta_a/2) & 0 \\ 1/2 \sin(\theta_a/4) & -1/2 \cos(\theta_a/4) & \sqrt{3}/2 \\ 1/2 \sin(\theta_a/4) & -1/2 \cos(\theta_a/4) & -\sqrt{3}/2 \end{bmatrix}, \quad (2.21)$$

and for a zigzag tube, with $\theta_z = 2\pi/n$, we have

$$\mathbf{\Lambda}_1 = \begin{bmatrix} \sqrt{3}/2 \sin(\theta_z/4) & \sqrt{3}/2 \cos(\theta_z/4) & 1/2 \\ \sqrt{3}/2 \sin(\theta_z/4) & -\sqrt{3}/2 \cos(\theta_z/4) & 1/2 \\ 0 & 0 & -1 \end{bmatrix}. \quad (2.22)$$

Finally, defining the two diagonal phase matrices, π and σ , for electrons and phonons, where, for armchair tube

$$\pi = \begin{bmatrix} e^{i\alpha\theta_z} & & \\ & e^{i(kc-\alpha\theta_a/2)} & \\ & & e^{i(-kc-\alpha\theta_a/2)} \end{bmatrix}, \sigma = \begin{bmatrix} e^{i\beta\theta_z} & & \\ & e^{i(qc-\beta\theta_a/2)} & \\ & & e^{i(-qc-\beta\theta_a/2)} \end{bmatrix}, \quad (2.23)$$

and for zigzag tube

$$\pi = \begin{bmatrix} e^{i(ka/2+\alpha\theta_z/2)} & & \\ & e^{i(ka/2-\alpha\theta_z/2)} & \\ & & e^{-ika} \end{bmatrix}, \sigma = \begin{bmatrix} e^{i(qa/2+\beta\theta_z/2)} & & \\ & e^{i(qa/2-\beta\theta_z/2)} & \\ & & e^{-iqa} \end{bmatrix}, \quad (2.24)$$

where, $c = \sqrt{3}a/2$ for armchair tube. Using these matrices, M_1 and M_2 becomes

$$M_1 = \left[- \sum_{\text{all rows}} \pi \mathbf{L}_1, \quad \sum_{\text{all rows}} \pi \sigma \mathbf{\Lambda}_1 \right] \mathbf{Q}' = \mathbf{\Xi}'_1 \mathbf{Q}', \quad (2.25)$$

$$M_2 = \left[- \sum_{\text{all rows}} \sigma^\dagger \pi^\dagger \mathbf{L}_1, \quad \sum_{\text{all rows}} \pi^\dagger \mathbf{\Lambda}_1 \right] \mathbf{Q}' = \mathbf{\Xi}'_2 \mathbf{Q}', \quad (2.26)$$

where, $Q' = (Q_{A\rho}, Q_{A\theta}, Q_{Az}, Q_{B\rho}, Q_{B\theta}, Q_{Bz})^T$. Finally it is convenient to express phonons in center of mass coordinates, thus

$$M_1 = \Xi'_1 \mathbf{U}_{\text{cm}}^\dagger \mathbf{U}_{\text{cm}} \mathbf{Q}' = \Xi_1 \mathbf{Q}, \quad (2.27)$$

$$M_2 = \Xi'_2 \mathbf{U}_{\text{cm}}^\dagger \mathbf{U}_{\text{cm}} \mathbf{Q}' = \Xi_2 \mathbf{Q}, \quad (2.28)$$

with \mathbf{U}_{cm} is defined by Eq. (A.63) in Appendix A, and

$$\Xi_1 = \left[- \sum_{\text{all rows}} \pi \mathbf{L}_1, \quad \sum_{\text{all rows}} \pi \sigma \mathbf{\Lambda}_1 \right] \mathbf{U}_{\text{cm}}^\dagger, \quad (2.29)$$

$$\Xi_2 = \left[- \sum_{\text{all rows}} \sigma^\dagger \pi^\dagger \mathbf{L}_1, \quad \sum_{\text{all rows}} \pi^\dagger \mathbf{\Lambda}_1 \right] \mathbf{U}_{\text{cm}}^\dagger. \quad (2.30)$$

Rearranging Eq. (2.16) we get,

$$V_{ep} = J_1 \sum_{k\alpha q\beta} \frac{M_1 + M_2}{2} \left(C_{A,k+q,\alpha+\beta}^\dagger C_{B,k,\alpha} + C_{B,k+q,\alpha+\beta}^\dagger C_{A,k,\alpha} \right) + \frac{M_1 - M_2}{2} \left(C_{A,k+q,\alpha+\beta}^\dagger C_{B,k,\alpha} - C_{B,k+q,\alpha+\beta}^\dagger C_{A,k,\alpha} \right). \quad (2.31)$$

Now, using

$$C_{A,k} = \frac{1}{\sqrt{2}} (u_{k,\alpha} + v_{k,\alpha}), \quad (2.32)$$

$$C_{B,k} = \frac{1}{\sqrt{2}} (u_{k,\alpha} - v_{k,\alpha}) \quad (2.33)$$

in Eq. (2.31) we obtain,

$$V_{ep} = J_1 \sum_{k\alpha q\beta} \frac{M_1 + M_2}{2} \left(u_{k+q,\alpha+\beta}^\dagger u_{k,\alpha} - v_{k+q,\alpha+\beta}^\dagger v_{k,\alpha} \right) + \quad (2.34)$$

$$\frac{M_1 - M_2}{2} \left(v_{k+q,\alpha+\beta}^\dagger u_{k,\alpha} - u_{k+q,\alpha+\beta}^\dagger v_{k,\alpha} \right). \quad (2.35)$$

Here the term $(u_{k+q,\alpha+\beta}^\dagger u_{k,\alpha} - v_{k+q,\alpha+\beta}^\dagger v_{k,\alpha})$ represents the intra-band transition, while, $(v_{k+q,\alpha+\beta}^\dagger u_{k,\alpha} - u_{k+q,\alpha+\beta}^\dagger v_{k,\alpha})$ is the inter-band transition, and the coefficient $(M_1 + M_2)/2$, and $(M_1 - M_2)/2$ are intra and inter band transition matrix elements respectively.

2.6.2 Armchair tube

In armchair tube, we are interested in scattering in metallic bands, for which $\alpha = \beta = 0$. Putting these in Eq. (2.31), we get for intra-band scattering $V_{ep,1} = J_1 (M_1 + M_2) / 2$,

$$\begin{aligned} V_{ep,1}/J_1 = & \sqrt{2} (\sin(\theta_a/2) + \sin(\theta_a/4) \cos(qc/2) \cos(kc + qc/2)) Q_\rho + \\ & \sqrt{6}i (\sin(qc/2) \cos(kc + qc/2)) Q_z + \cdot \quad (2.36) \\ & \sqrt{2} (\cos(\theta_a/4) \cos(qc/2) \cos(kc + qc/2) - \cos(\theta_a/2)) q_\theta \end{aligned}$$

Similarly for inter-band scattering $V_{ep,2} = J_1 (M_1 - M_2) / 2$,

$$\begin{aligned} V_{ep,2}/J_1 = & \sqrt{2} (\cos(\theta_a/4) \sin(qc/2) \sin(kc + qc/2)) Q_\theta + \\ & \sqrt{2} (\sin(\theta_z/4) \sin(qc/2) \sin(kc + qc/2)) q_\rho - \cdot \quad (2.37) \\ & \sqrt{6}i (\cos(qc/2) \sin(kc + qc/2)) q_z \end{aligned}$$

Assuming $k = 4\pi/3\sqrt{3}a$ and varying q over the BZ, the components of intra-band and inter-band matrix elements are plotted in Fig. 2.10b,c. As shown in Fig. 2.10b, and in Eq. (2.36), the intra-band matrix elements depend on TO (q_θ), LA (Q_z) and RBM (Q_ρ), with RBM being the weakest scattering mode. For the inter-band matrix element, $V_{ep,2}$, on the other hand, only LO and TW modes contribute to scattering. The eigenvectors of actual phonon modes, however, have mixed polarization as shown in Fig. 2.6 for $\beta = 0$ subband of a (10,10) armchair tube. Using these eigenvectors in Eqs. (2.36) and (2.37) the intra and inter-band matrix elements are next calculated as shown in Fig. 2.10d,e. Here, br-5 gives intra-band scattering with interaction potential of 11.23eV/A and 15.9eV/A at Γ ($q = 0$) and K ($q = 4\pi/3\sqrt{3}a$) points respectively. br-3 also gives intra-band scattering but it has negligible interaction potential near the Γ and K points, and can be neglected. br-6 gives inter-band scattering with interaction potential of 11.23eV/A at Γ point (this gives backscattering) and 0 at K point (at K this is forward scattering). TW mode gives inter-band acoustic phonon scattering with deformation constant of $J_1\sqrt{6}a/4 \cos(\theta_a/4) \sin(2\pi/3) \approx 4eV$.

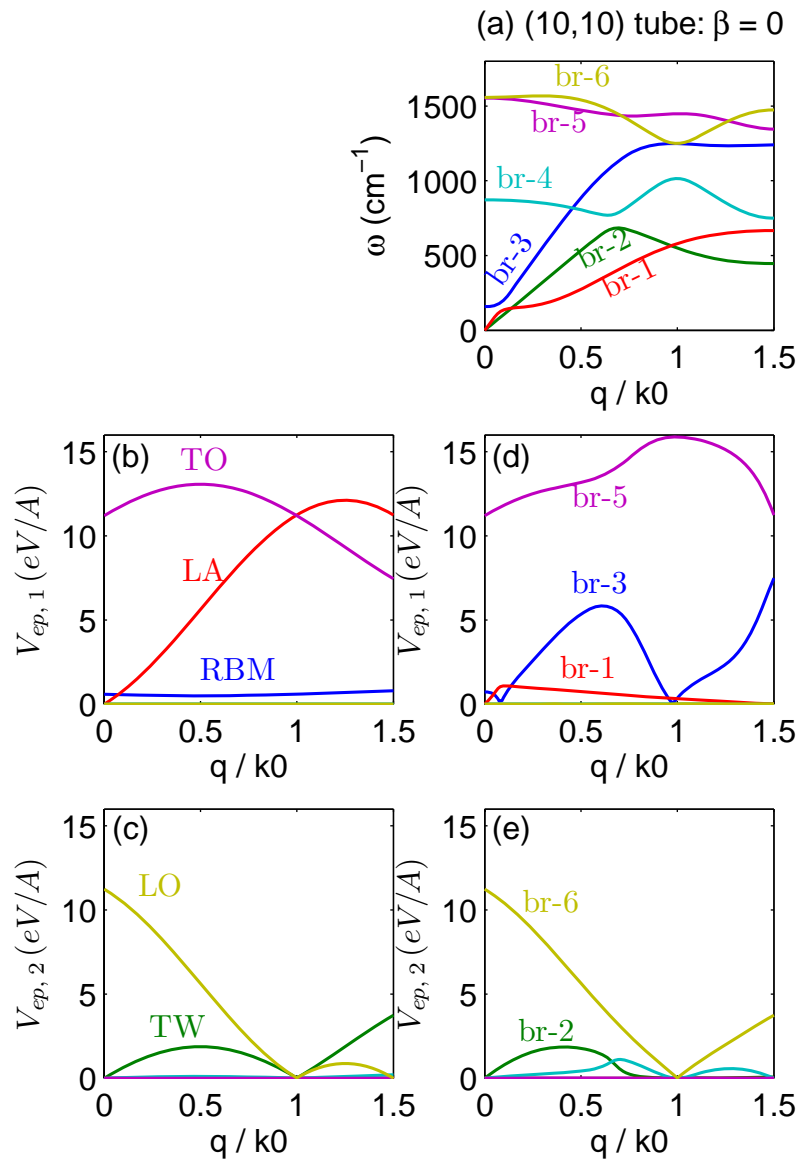


Fig. 2.10. (a) Phonon modes of (10,10) armchair tube for $\beta = 0$ sub-band. (b) Intra-band matrix elements for various 'pure' polarizations. (c) Inter-band matrix elements for various 'pure' polarizations. (d) Intra-band matrix elements due to the 6 phonon branches shown in (a), and (e) inter-band matrix elements due to these phonon branches.

Scattering rates

Using the Fermi's golden rule [61], the scattering rates for the above processes can be calculated as

$$\frac{1}{\tau(k, k_f)} = \frac{2\pi}{\hbar} |\chi V_{ep}(k, k_f)|^2 \text{DOS}(k_f), \quad (2.38)$$

where, $V_{ep} \rightarrow V_{ep,1}$ or $V_{ep,2}$ is the interaction potential, $k_f = k + q$, $\text{DOS}(k_f)$ is the density of final states, and phonon mode amplitude,

$$\chi = \sqrt{\frac{\hbar}{2m_c n N_u \omega}} (1 + N). \quad (2.39)$$

Here, n is the chirality, N_u is the number of unit-cells (A, B pairs) per unit length, and N is phonon mode population. A simple calculation shows that, for tube with diameter, d_t ,

$$\chi = \sqrt{\frac{3\hbar a^2}{4\pi m_c d_t \omega}} (1 + N), \quad (2.40)$$

with $N = 1/(\exp(\hbar\omega/k_B T) - 1)$ is the Bose-Einstein factor, $m_c = 2 \times 10^{-26}$ Kg is the mass of a carbon atom. For each phonon branch, an electron can be scattered either by a zone center phonon (Γ process) or by a zone boundary phonon (K process) as shown in Fig. 2.11 The calculated scattering rates for br-2, br-5 and br-6 for each of

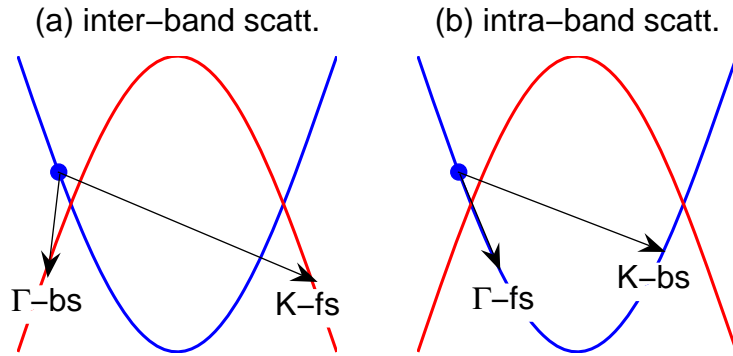


Fig. 2.11. (a) inter-band scattering, (b) intra-band scattering.

these Γ and K processes are shown in Fig. 2.12

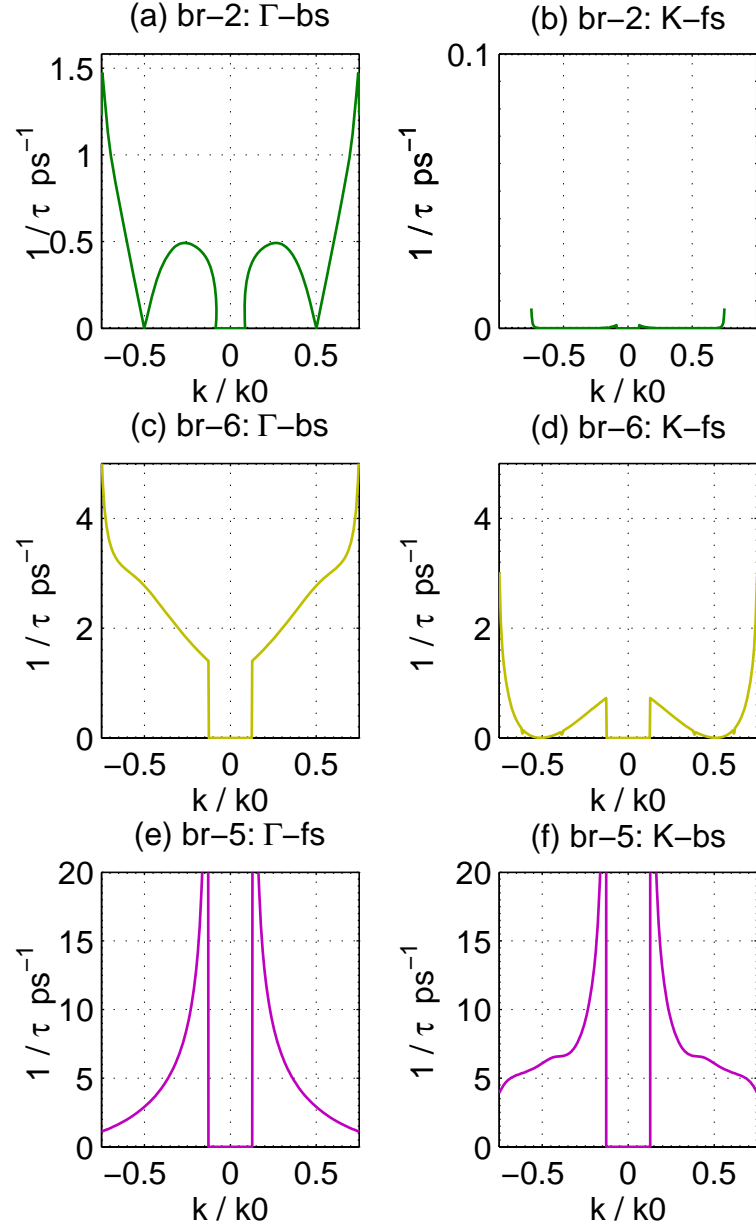


Fig. 2.12. Scattering rates for br-2, br-5 and br-6. (a) Γ scattering (emission + absorption) for br-2. Since, br-2 is an acoustic mode both emission and absorptions at room temperature are considered. (b) K scattering for br-2. (c) Γ emission for br-6, (d) K emission for br-6. (e) Γ emission for br-5 and (f) K emission for br-5. Here k is electron wavevector. Final states, k_f and phonon wavevector $q = k_f - k$ are calculated using the electron and phonon dispersion relations according to the selection rule.

2.6.3 Zigzag tube

Next, we look at zigzag tubes with considerable bandgap. For electronic transport, the inter-band transition is not important (since the phonons do not have much smaller energy than the bandgap, they cannot initiate transition between conduction to valence bands), thus we only care about $V_{ep,1}$. For zigzag tubes the zone-center scattering occurs with $\beta = 0$ phonon subband, and the zone boundary scattering occurs with $\beta = \pm 8$ phonon subband. The variation of the matrix elements with ‘pure’ polarizations are shown in Fig. 2.13. Figure 2.14 shows the variation of the actual

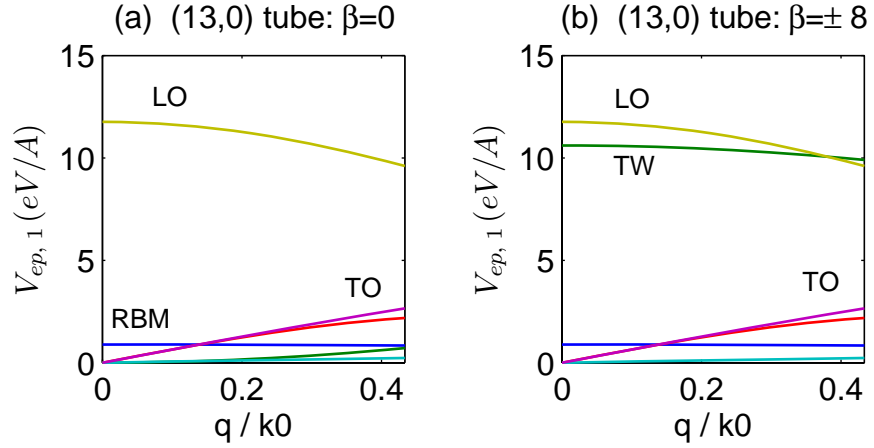


Fig. 2.13. (a) Components of intra-band matrix elements with zone center phonon and (b) zone-boundary phonon.

variation of the matrix elements with phonon branches. For zone-center phonon br-6 (LO at Γ point) gives the strongest EPC with interaction potential of 11.75eV/A. Scattering by br-3 (RBM) is much weaker with a deformation potential of 1.078eV/A, while the br-1 (LA) is the only acoustic mode with deformation constant of 4eV/A. For zone boundary phonons, br-6 of Fig. 2.14b gives the strongest scattering with deformation potential of 15.9eV/A. Another K-phonon with much smaller deformation potential is branch 4, with interaction potential of 1.82eV/A. The scattering rates for all of these modes are shown in Fig. 2.15.

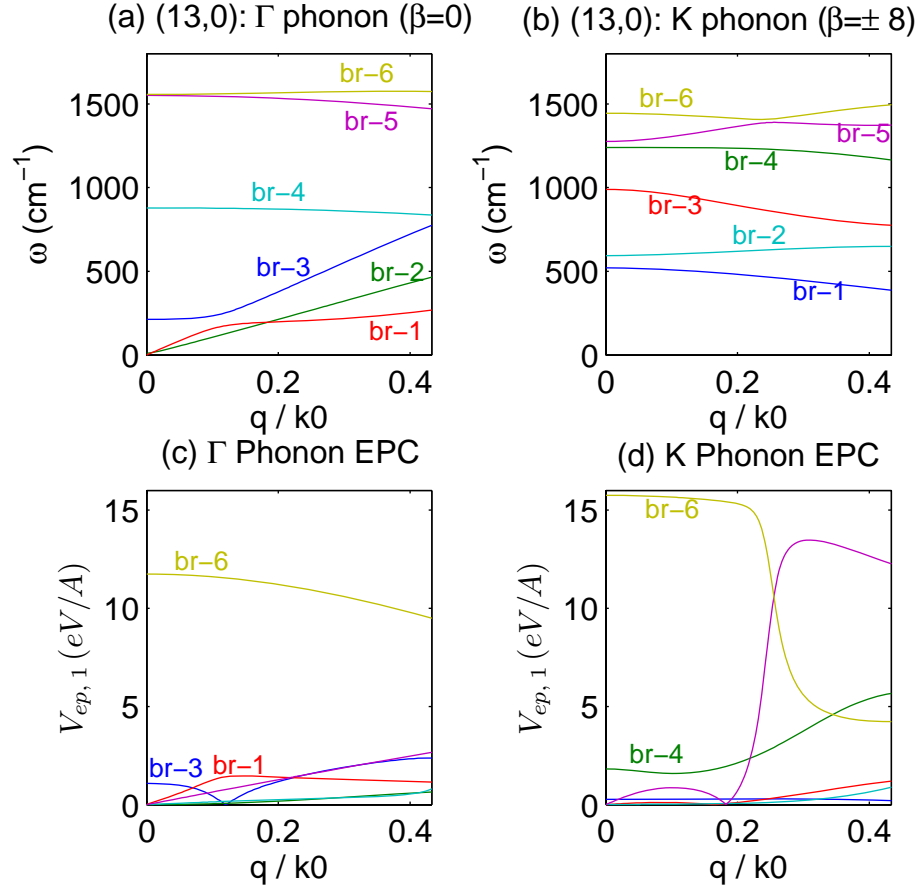


Fig. 2.14. Phonon modes of (13,0) tube for (a) $\beta = 0$ subband (zone center phonons) and (b) $\beta = \pm 8$ subband (zone boundary phonons). (c) Interaction potential corresponding to phonon branches of (a) and (d) interaction potential due to phonon branches of (b).

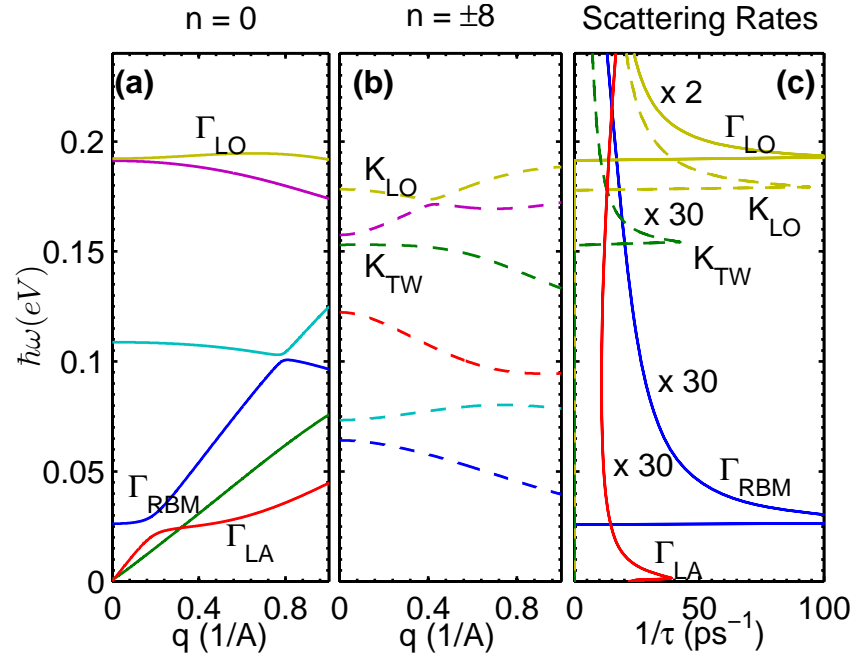


Fig. 2.15. Phonon dispersion branches of a (13,0) tube belonging to (a) $n=0$ phonon subband, and (b) $n=8$ phonon subbands. (c) Total backscattering rates (em + abs) at room temperature. For LA mode both emission and absorption rates contribute, while for all other modes absorption is negligible at 300K.

2.7 Summary

A symmetry based phonon mode calculation method has been developed for arm-chair and zigzag tubes. The method is as accurate as the force constant method. Next, a method to calculate electron phonon coupling (EPC) in these tubes has been developed based on Mahan's original work [49]. In the following chapters the phonon eigenvectors obtained from phonon dispersion calculation is coupled with the EPC calculation scheme to calculate the electron phonon scattering rate over the full band.

3. BTE SIMULATION OF COUPLED ELECTRON PHONON TRANSPORT IN CARBON NANOTUBES

3.1 Introduction

In the previous chapter, a detailed study of the electron-phonon interaction and a calculation of scattering rates have been done. In this chapter, we describe a transport solver for coupled carrier transport in CNTs. Semiconducting tubes will be considered in this chapter, metallic tubes are the subject of the next chapter. It has shown in Chapter 4 that to describe the I-V characteristics of a metallic tube, both self-heating and hot-phonon effects need to be considered. The same should be true for the semiconducting tubes as well, thus, we develop a coupled electron-phonon transport solver which is self-consistently combined with the Poisson and heat-equations. For electron and phonon transport, a direct solution of the Boltzmann transport equation (BTE) is used. Recently, the Monte-Carlo (MC) method of solving BTE has been reported in the literature [51–53, 55, 56, 71], however, MC simulation has the disadvantage of being noisy. Since carbon nanotubes (CNT) are a 1D system, their phase space in the $x - k$ plane forms a two-dimensional space, and the direct solution of the BTE is practical. In fact, the BTE has already been solve directly by Yao et al. [46] for metallic tubes. Semiconducting tubes, however, have the additional complication due to their non-linear bandstructure. Besides, application of BTE to semiconducting devices has not done yet. Unlike the bulk, devices provide two additional complications: i) the distribution function needs to be resolved into space ($\partial_x \neq 0$), and ii) electrostatics within the device needs to be solved in order to know the electric field ($\mathcal{E} \neq V/L$). In this chapter, we develop a coupled electron-phonon BTE solver for CNT-MOSFETs.

3.2 Simulation approach

We assume an idealized, co-axially gated device geometry with ideal MOSFET like source/drain (s/d) contacts. Schottky barrier type devices will not be treated in this study. We start by assuming an internal electric field within the device, \mathcal{E} . Using this and an initial temperature profile $T(x)$, the electron BTE is solved for a time step, dt , which gives a new distribution function, f . The phonon BTE is also solved simultaneously to get a new phonon population, n_ν . Keeping $T(x)$ fixed, these time dependent electron-phonon BTEs and the Poisson equations are solved until steady-state is reached. Here, an explicit time-stepping method (Euler's method) has been used to solve the time dependent BTEs for simplicity. To obtain a stable solution, sufficiently short time step should be used, which is determined in the following way: starting with a large time step dt , we solve the electron and phonon BTEs. Since, dt is large it creates oscillation and the distribution functions become either greater than one or less than zero. If this happens we reduce dt by 2 $dt \rightarrow dt/2$ and restart solving the BTEs with this new time-step from the beginning. Continuing this way a suitable time step is obtained which is large enough to reach the steady-state faster yet small enough to ensure stability. Next, using the steady-state power density as input in the heat-equation, a new temperature is calculated and the whole process is repeated until self-consistently is achieved. Figure 3.1 shows the device structure and the simulation scheme.

3.3 Electron transport

Since carbon nanotubes are quasi-one dimensional (1D) conductors, the evolution of an electronic state (k, α) can be described by a 1D Boltzmann transport equation (BTE) [61]

$$\partial_t f = (-v_k \partial_x + q\mathcal{E}/\hbar \partial_k) f + \hat{C}f, \quad (3.1)$$

where, $v_k = \partial E/\hbar \partial k$ is the group velocity of a particular subband, \mathcal{E} is the electric field, and $\hat{C}f$ is the collision integral. For different tube chiralities and diameters, the

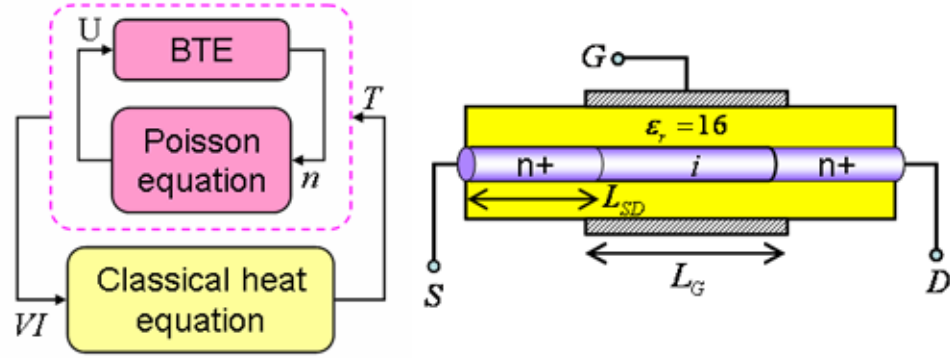


Fig. 3.1. (a) Flowchart of the simulation scheme. Electron and phonon BTEs, and the Poisson equation are solved until steady-state is reached. Steady-state power density, IdV/dx is then used to calculate new T from heat equation, and the whole procedure is repeated until steady-state is reached. (b) Device structure of an ideal CNT MOSFET. Doped source (S) and drain (D) has been assumed. Here, L_G is the Channel length, and, L_{SD} is the S/D extension length. Metal gate is used with workfunction 4.7eV and a 3nm thick HfO_2 gate dielectric ($\epsilon = 16$) is also assumed.

group velocity and the collision integral terms change according to the bandstructure. In this work, we consider only the zigzag tube as representative of semiconducting tubes for simplicity. Chiral tubes can be treated similarly by using the appropriate bandstructure.

3.3.1 Bandstructure

Zigzag tubes are considered as an example of semiconducting tubes. The bandstructure of a zigzag tube is [65]:

$$E_\alpha = \pm t_0 \sqrt{1 + 4 \cos\left(\frac{\pi\alpha}{n}\right) \cos\left(\frac{3ka}{2}\right) + 4 \cos^2\left(\frac{\pi\alpha}{n}\right)}, \quad (3.2)$$

with n – being the chiral index of the $(n, 0)$ tube, and α is the subband index. Positive (negative) sign is for the conduction (valence) band. Velocity is obtained by differentiating the E-k

$$v_k^\pm = 2v_F \cos(\pi\alpha/n) \left\{ \frac{\sin(3ka/2)}{E/t} \right\}, \quad (3.3)$$

where, $v_F = 3at/2\hbar \approx 8.45 \times 10^5 m/s$. For a zigzag tube, the BZ extends from $-\sqrt{3}k_0/4$ to $\sqrt{3}k_0/4$. Figure 3.2 shows the E-k and the velocity of a $(13, 0)$ zigzag tube for the lowest subband ($\alpha = 9$). Here the size of BZ is $\sqrt{3}k_0/2$, while the periodicity of the band is $\sqrt{3}k_0$ – twice the BZ.

3.3.2 Free flight operator

In the BTE, the time evolution of electronic state between two successive scattering events is described by the linear operator $(-v_k \partial_x + q\mathcal{E}/\hbar \partial_k)$. This operator is discretized on a finite difference (FD) grid, resulting a Matrix operator, called ‘free-flight’ operator. In this section, we will describe how to set up this matrix. To illustrate the mechanics, let us consider the grid in Fig. 3.3. Each point in the phase-space has its grid coordinate: (i, j) , where, i is the x -grid coordinate, and j is the k -grid coordinate. A single number is also assigned to each point (i, j) , according

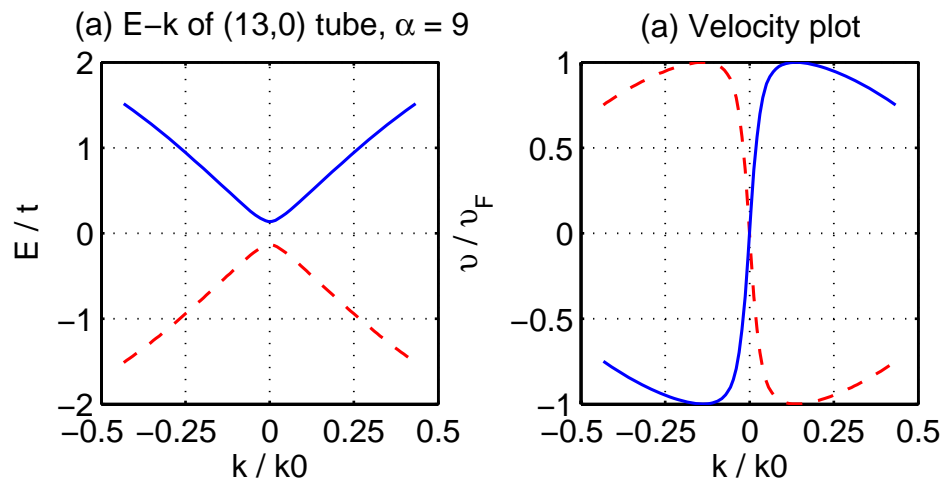


Fig. 3.2. The lowest subbands ($\alpha = 9, 17$) of a (13,0) zigzag tube. (a) Normalized E-k, and (b) velocity plot. Here Fermi velocity, $v_F = 3at/2\hbar = 8.4 \times 10^5 m/s$, $t = 2.6 eV$, and $k_0 = 4\pi/3\sqrt{3}a \sim 1.7/A$.

to $l \rightarrow (i-1)N_x + j$. At any point (i, j) , which has positive velocity (i.e. $v_j > 0$),

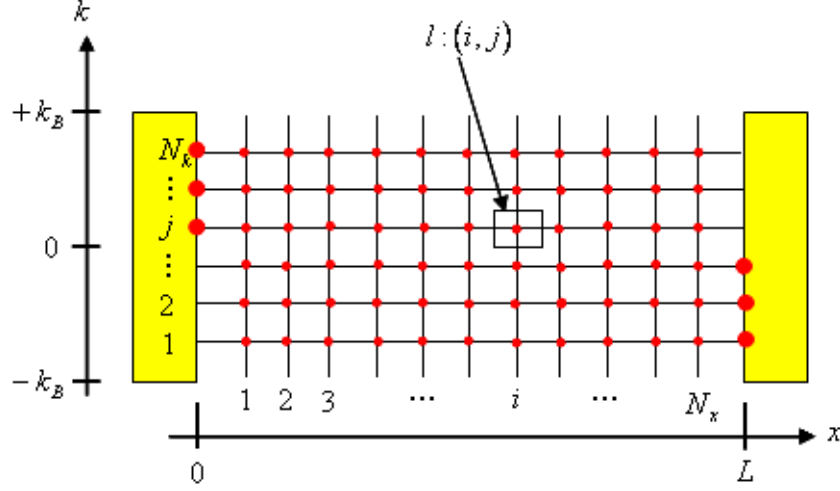


Fig. 3.3. A finite difference grid used to discretize the Boltzmann transport equation. The big circles on the boundary are outside the simulation domain and serves as boundary condition.

electrons move from left to right, and the $-\partial_x$ operator for it can be approximated by a backward difference scheme, similarly for any negative moving carrier with, $v_j < 0$, its $-\partial_x$ operator is approximated by a forward difference scheme. In the same way, if $\mathcal{E}_i < 0$ at x -grid, i , then electron's wavevector increases and $-\partial_k$ is replaced by forward difference, and for positive electric field, the backward difference is used. Thus for an electron at (i, j)

$$-v_k \frac{\partial f}{\partial x} \approx \begin{cases} (f_{i-1,j} - f_{i,j}) |v_j / \Delta x|, & \text{if } v_j > 0 \\ (f_{i+1,j} - f_{i,j}) |v_j / \Delta x|, & \text{if } v_j < 0 \end{cases} \quad (3.4)$$

$$-\frac{q\mathcal{E}}{\hbar} \frac{\partial f}{\partial k} \approx \begin{cases} (f_{i,j-1} - f_{i,j}) |q\mathcal{E}_i / \hbar \Delta k|, & \text{if } \mathcal{E}_i < 0 \\ (f_{i,j+1} - f_{i,j}) |q\mathcal{E}_i / \hbar \Delta k|, & \text{if } \mathcal{E}_i > 0 \end{cases} \quad (3.5)$$

Alternate methods such as Scharfetter-Gummel scheme [72] or central difference scheme [73] are also available which eliminate the need for explicit sign checking

as done above. Applying this discretization scheme to all equations on the phase space and arranging them into a matrix form, Eq. (3.1) we get

$$\frac{\{f^{n+1}\} - \{f^n\}}{dt} = [\mathbf{U}] \{f^n\} + \{f_B\} + \{\hat{C}f\}. \quad (3.6)$$

Since, the collision integral, $\{\hat{C}f\}$, is a non-linear term, the above equation has to be solved iteratively. In Eq (3.6) the terms $\{f^{n+1}\}$ and $\{f^n\}$, are the distribution functions at $n+1$ and n iterations, $\{f_B\}$ is the boundary term arising from the ∂_x, ∂_k operators, and \mathbf{U} is the FD operator that incorporates the above mentioned forward and backward differences. For a total of $N = N_x \times N_k$ grid points, \mathbf{U} is a 4 diagonal sparse matrix of size $N \times N$. Consider a regular point $l : (i, j)$, which is not on x or k boundaries. Then the l^{th} row of \mathbf{U} corresponding to this point, have the following entries

$$U_{l,l} = -\frac{|v_j|}{\Delta x} - \frac{|q\mathcal{E}_i|}{\hbar\Delta k}, \quad (3.7)$$

if $v_j > 0$:

$$U_{l,l-1} = |v_j|/\Delta x, \quad (3.8)$$

if $v_j < 0$:

$$U_{l,l+1} = |v_j|/\Delta x, \quad (3.9)$$

if $\mathcal{E}_i < 0$:

$$U_{l,l-N_x} = |q\mathcal{E}_i|/\hbar\Delta k, \quad (3.10)$$

if $\mathcal{E}_i > 0$:

$$U_{l,l+N_x} = |q\mathcal{E}_i|/\hbar\Delta k. \quad (3.11)$$

If l is one of the left x -boundary points: $i = 1, N_x + 1 \cdots (N_k - 1) N_x + 1$, then we ignore it's left neighboring term, $U_{l,l-1}$. If l is one of the right x -boundary points: $N_x, 2N_x \cdots N_k N_x$, then the right neighboring term, $U_{l,l+1}$ is ignored. Similarly for the bottom k -boundary points: $1, 2 \cdots N_x$ all the $U_{l,l-N_x}$ terms, and for the top k -boundary points, all the $U_{l,l+N_x}$ terms are ignored. These boundary points since, that are not included in the matrix, \mathbf{U} , constitute the boundary condition vector $\{f_B\}$.

3.3.3 Boundary conditions

The boundary condition $\{f_B\}$ arise from the ∂_x operator. Physically it represents the flux input from the left and right contacts. The left contact can only fill up the k states at $l = 1, N_x + 1 \cdots N_x N_k - N_x + 1$, and the right contact can only fill up the states at $l = N_x, 2N_x \cdots N_x N_k - N_x$. Thus the boundary condition becomes

$$f_B(l_m) = \left\{ 1 + \exp \left(\frac{E(k_m) - \mu_L}{k_B T} \right) \right\}^{-1} (v_m > 0), \quad (3.12)$$

$$f_B(l_m + N_x) = \left\{ 1 + \exp \left(\frac{E(k_m) - \mu_R}{k_B T} \right) \right\}^{-1} (v_m < 0), \quad (3.13)$$

where, $l_m = 1 + (m - 1)N_x$, μ_L and μ_R are the left and right contact Fermi levels respectively. By varying $m = 1 \cdots N_k$ all the non-zero entries of $\{f_B\}$ vector are obtained. Note that in evaluating the elements, we used a logical operation $(v_m > 0)$, which yields either 0 or 1 value according to whether v_m is positive or negative.

For the ∂_k operator, the periodic boundary condition (p.b.c.) is used. This ensures the conservation of particles. Physically carriers undergo Bloch oscillation [74] when they reach the end of the band. Periodic boundary conditions do not yield any terms to $\{f_B\}$, rather this add some additional terms to \mathbf{U} in the following way

$$U_{p, N - N_x + p} = \frac{|q\mathcal{E}_p|}{\hbar \Delta k} (\mathcal{E}_p < 0), \quad (3.14)$$

$$U_{N - N_x + p, p} = \frac{|q\mathcal{E}_p|}{\hbar \Delta k} (\mathcal{E}_p > 0), \quad (3.15)$$

where, $p = 1 \cdots N_x$, and $N = N_k N_x$.

One more boundary condition is left to be specified. Since the BTE is solved in time, we need an initial guess of the distribution function. For this, the equilibrium ballistic distribution function is used, which is obtained in the following way. Under zero applied bias, solution of the Poisson equation gives the built-in potential and the internal electric fields, \mathcal{E}_i , at each node. Using these, the free-flight operator, \mathbf{U} , under the equilibrium condition. At steady-state putting $S = 0$ (ballistic), the equilibrium ballistic solution becomes

$$\{f^0\} = - [\mathbf{U}^{-1}] \{f_B\}, \quad (3.16)$$

where, $\{f^0\}$ is the initial guess.

3.3.4 Collision integral

The collision integral is the net rate of increase of $f(x, k, t)$ due to collision and is calculated in the following way [61]

$$\hat{C}f = \sum_{k' \uparrow} f(k') (1 - f(k)) S(k', k) - \sum_{k' \uparrow} f(k) (1 - f(k')) S(k, k'), \quad (3.17)$$

where, the first term is the total rate of in-scattering to state k and the second term is the total rate of out-scattering from state k . Here the sum is performed over a single spin since phonon scattering does not change the spin [61]. The term $S(k_1, k_2)$ represents the transition rate from $k_1 \rightarrow k_2$ and is calculated using the Fermi's Golden rule [61]

For in-scattering,

$$S(k', k) = \frac{2\pi}{\hbar} |H_{k,k'}|^2 \delta \{E(k) - E(k') \pm \hbar\omega(k - k')\} \left(\frac{1}{2} \pm \frac{1}{2} + n_\nu(k - k') \right), \quad (3.18)$$

For out-scattering,

$$S(k, k') = \frac{2\pi}{\hbar} |H_{k',k}|^2 \delta \{E(k') - E(k) \mp \hbar\omega(k' - k)\} \left(\frac{1}{2} \pm \frac{1}{2} + n_\nu(k' - k) \right). \quad (3.19)$$

Here, $H_{k,k'}$, $H_{k',k}$ are the electron-phonon matrix elements, which are calculated in the previous chapter, and n_ν is the phonon population. The upper (lower) signs above represent emission (absorption), and the delta function comes from the conservation of energy and momentum in the scattering process [75]. Using the property of the delta function [76]: $\delta \{g(x)\} = \sum_i \delta(x - x_i) / |g'(x_i)|$, where, x_i are the zeros of $g(x)$, the above delta functions for in-scattering are simplified as

$$\delta \{E(k) - E(k') + \hbar\omega(k - k')\} = 2\pi \sum_{i=1,2} \delta(k - k_i^{em}) \mathcal{D}(E_i^{em}), \quad (3.20)$$

$$\delta \{E(k) - E(k') - \hbar\omega(k - k')\} = 2\pi \sum_{i=1,2} \delta(k - k_i^{ab}) \mathcal{D}(E_i^{ab}), \quad (3.21)$$

similarly for out-scattering

$$\delta \{E(k') - E(k) - \hbar\omega(k' - k)\} = 2\pi \sum_{i=1,2} \delta(k - k_i^{ab}) \mathcal{D}(E_i^{ab}), \quad (3.22)$$

$$\delta \{E(k') - E(k) + \hbar\omega(k' - k)\} = 2\pi \sum_{i=1,2} \delta(k - k_i^{em}) \mathcal{D}(E_i^{em}), \quad (3.23)$$

where, k_i^{em} , k_i^{ab} are the zeros of the arguments of the delta functions and are shown in Fig. 3.4, and $\mathcal{D}(E)$, the various density of states (DOS), are the derivatives of the

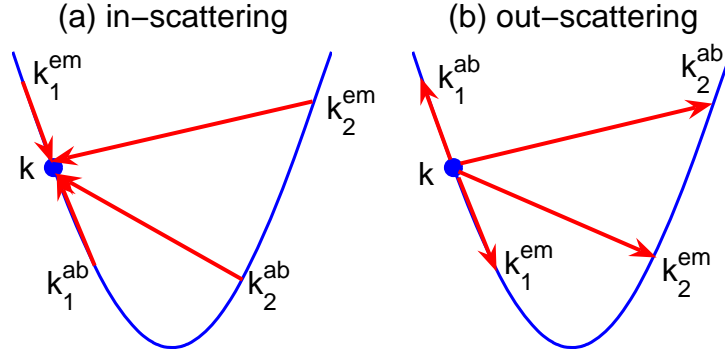


Fig. 3.4. (a) In-scattering processes. Any state k is coupled with 4 states k_1^{em} , k_2^{em} , k_1^{ab} , and k_2^{ab} . The two emission points are the solution to the equation: $E(k) - E(k') + \hbar\omega(k - k') = 0$, and the two absorption points are solution to the equation: $E(k) - E(k') - \hbar\omega(k - k') = 0$. Here, k' is the variable. (b) Out-scattering processes. Here, k_1^{em} and k_2^{em} are the solution to the equation: $E(k') - E(k) - \hbar\omega(k' - k) = 0$ and k_1^{ab} and k_2^{ab} are the solution to the equation: $E(k') - E(k) + \hbar\omega(k' - k) = 0$.

arguments. For the in-scattering process

$$\begin{aligned} &\text{Defining } g(k') = E(k) - E(k') \pm \hbar\omega(k - k'), \\ &\Rightarrow g'(k'_i) = -\hbar \left\{ \frac{dE(k'_i)}{\hbar dk'} \pm \frac{d\omega(k - k'_i)}{d(k - k')} \right\} \approx -\hbar v_{k'}. \end{aligned} \quad (3.24)$$

Here, the second term within the bracket, which is phonon's group velocity, is dropped out because it is at least 2 orders of magnitude smaller than electron's group velocity [66], $v_{k'}$. Thus

$$\left| \frac{1}{g'(k'_i)} \right| \approx 2\pi \mathcal{D}(E(k'_i)). \quad (3.25)$$

The exact same equation holds for the out-scattering processes. Note that, k'_i is an initial state for in-scattering process and a final state for an out-scattering process, thus, for calculating the transition rates for in-scattering process, the initial-DOS is used while in calculating the transition rates for out-scattering process the final-DOS is used; this ensures the detailed balance at equilibrium. The above assumption of considering only electronic DOS fails near the Van-Hoove singularities ($dE/\hbar dk = 0$), where the phonon DOS (the $dq/d\omega$ term) must be considered to get a finite value of the scattering rates.

Since each subband in zigzag tube is doubly degenerate (for $\alpha_{1,2} = \text{round}(2n/3)$, $\text{round}(4n/3)$), two phonon branches are required for scattering. Phonon subband, $\beta_1 = \alpha_1 - \alpha_1 = \alpha_2 - \alpha_2 = 0$ gives intra-valley scattering and subband, $\beta_2 = \pm(\alpha_2 - \alpha_1)$ gives the inter-valley scattering. There 12 branches as shown in Fig. 3.5, only 5 of them contribute to scattering, the rest of the branches have negligible scattering rates compared to these five branches. For each of the five phonon branches, the 4 neighboring states k_1^{em} , k_2^{em} , k_1^{ab} , k_2^{ab} are calculated for in-scattering and out-scattering processes. Next the matrix elements for each of these scattering paths are calculated and finally the transition probabilities are calculated using Eq. (3.17). Below we show the transition rates for out-scattering emission processes for k_2^{em} states which give backscattering. Other processes have similar rates.

3.4 Phonon transport

Next we consider the phonon BTE which is similar to the electron BTE except there is no field dependent term. Thus

$$\partial_t n_\nu(x, q, t) = -v_q \partial_x n_\nu(x, q, t) + G_\nu(x, q, t) - \frac{n_\nu - n_{\nu,0}}{\tau}, \quad (3.26)$$

where n_ν is the distribution function of phonon branch ν , $v_q = d\omega_\nu/dq$ is the phonon group velocity, $G_\nu(x, q, t)$ is the generation rate of phonons by electron-phonon scattering, and the last term takes care of the anharmonic decay of the phonon. Here we have used a relaxation time approximation (RTA) with $n_{\nu,0}$ is the equilibrium popu-

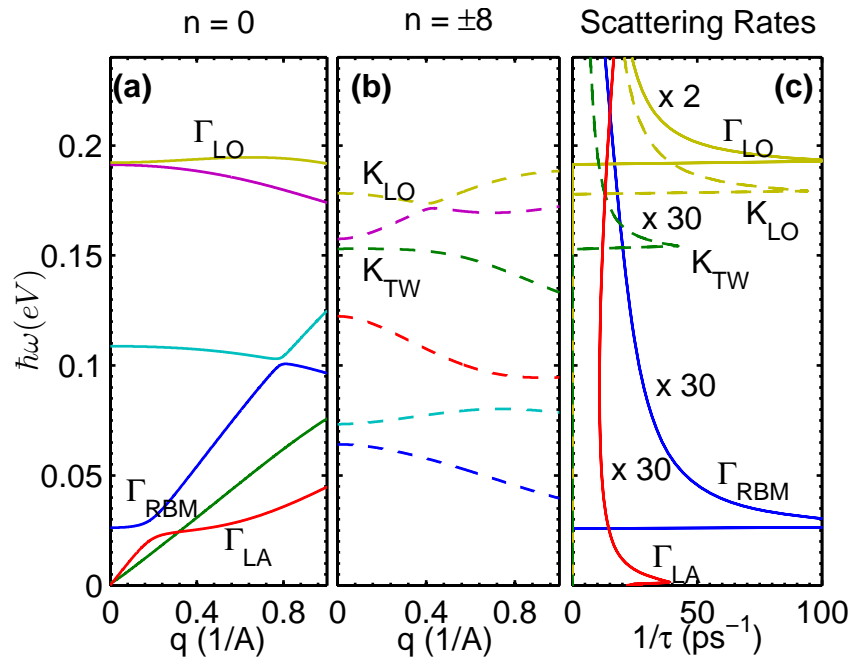


Fig. 3.5. Phonon dispersion branches of a (13,0) tube belonging to (a) $n=0$ phonon subband, and (b) $n= \pm 8$ phonon subbands. (c) Total backscattering rates (em + abs) at room temperature. For LA mode both emission and absorption rates contribute, while for all other modes absorption is negligible at 300K.

lation of branch ν and τ is the relaxation time, which is used as a fitting parameter. Alternative to RTA is to use a microscopic theory of phonon-phonon scattering which requires i) the determination of the anharmonic lattice potential, ii) calculation of the matrix elements for phonon-phonon coupling, and iii) inclusion of all the phonon subbands that are coupled by the phonon-phonon scattering.

3.4.1 Free flight

As in the case with electron BTE, there is a free-flight term for the phonon BTE also. We use the same finite difference scheme to discretize the phonon BTE, which become

$$\frac{\{n_\nu\}^{p+1} - \{n_\nu\}^p}{dt} = [\mathbf{U}_\nu] \{n_\nu^p\} + \{n_{\nu,B}\} + \{G^p\} - \frac{\{n_\nu^p\} - \{n_o\}}{\tau}, \quad (3.27)$$

where, n_ν^{p+1} and n_ν^p are phonon distribution functions at $p + 1$ and p^{th} iteration respectively and $n_{\nu,B}$ is the boundary term. Operator \mathbf{U}_ν is calculated exactly the same way as done for electron, except for the fact that the electric field terms are zero. Only 5 out of 12 phonon branches have significant scattering rates, hence only their velocities are calculated (see Fig. 3.6), which are then used to calculate \mathbf{U}_ν .

3.4.2 Generation rate

The phonon generation rate, $G(x, q, t)$ is the difference between the phonon emission rate and the phonon absorption rate

$$\begin{aligned} G(x, q, t) = & \frac{2\pi}{\hbar} \sum_{k,\uparrow} |H_{k,k+q}|^2 \delta \{E(k+q) - E(k) + \hbar\omega(q)\} \times \\ & f(k) (1 - f(k+q)) (1 + n_\nu(q)) - \\ & \frac{2\pi}{\hbar} \sum_{k,\uparrow} |H_{-k-q,-k}|^2 \delta \{E(-k) - E(-k-q) + \hbar\omega(q)\} \times \\ & f(-k-q) (1 - f(-k)) n_\nu(q), \end{aligned} \quad (3.28)$$

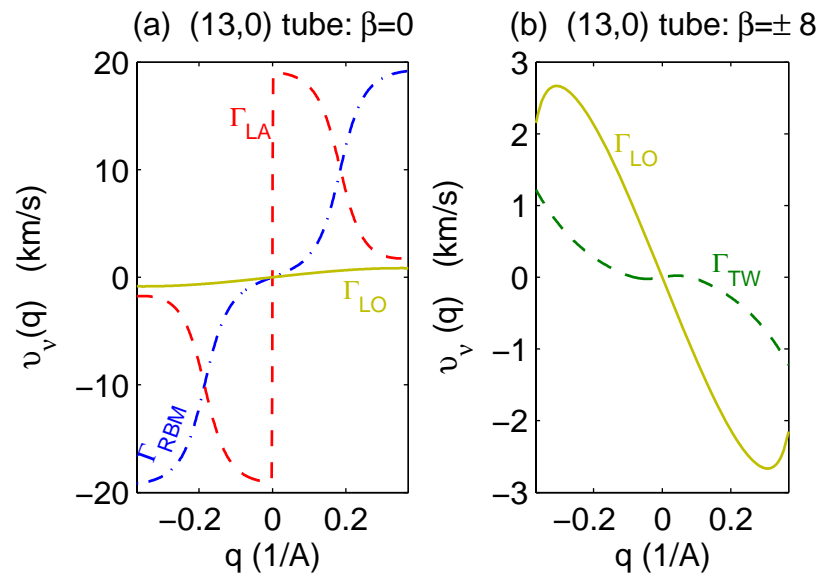


Fig. 3.6. Phonon mode velocities of (13,0) tube. (a) For subband $\beta = 0$, and (b) for $\beta = \pm 8$.

where, the first term is the emission and the second term is for the absorption processes. Thus for a particular q , a k is searched, which is such that,

$$E(k + q) = E(k) - \hbar\omega(q). \quad (3.29)$$

Once, k associated with a particular q is obtained the 4 end points for emission and absorptions are immediately calculated as shown in Fig. 3.7. These are shown in Fig. 3.7. The evaluation of the delta function for phonons is slightly different as shown

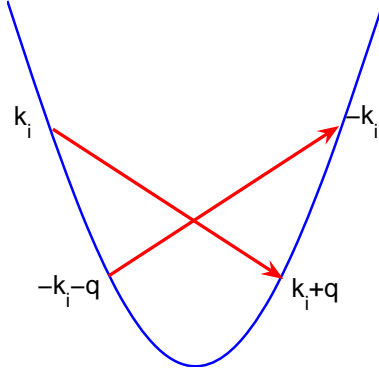


Fig. 3.7. Four end points that are related to phonon wavevector q of a particular phonon branch ν . For emission process, the initial and final states are k_i and $k_i + q$, for absorption process the initial and final states are $-k_i - q$ and $-k_i$. Note that, by determining k_i , which is obtained by solving the equation: $E(k_i + q) - E(k) + \hbar\omega(q) = 0$, all other states can be calculated from there.

below

$$\delta \{E(k + q) - E(k) + \hbar\omega(q)\} = \frac{2\pi}{2\pi\hbar |v(k_i + q) - v(k_i)|}. \quad (3.30)$$

Similarly for the absorption process

$$\delta \{E(-k) - E(-k - q) - \hbar\omega(q)\} = \frac{2\pi}{2\pi\hbar |v(-k_i) - v(-k_i - q)|}. \quad (3.31)$$

3.4.3 Phonon relaxation

Finally we consider the phonon relaxation term, $(n_\nu - n_{\nu,0})/\tau$, which represents the decay of the phonons due to anharmonicity [66]. By fitting the metallic tube

experimental data, the optical phonon relaxation time, was estimated to be $3ps$ which is in good agreement with the experimentally observed values [77,78]. Also, the term $n_{\nu,0}$ represents the equilibrium phonon population at a given temperature T . These are calculated for each phonon branch using their respective dispersion relations and the Bose-Einstein statistics.

3.5 Power flow and heat equation

Let us now consider the power flow in the system. This is shown schematically in Fig. 3.8. The whole system is divided into five sub-systems. These are: the elec-

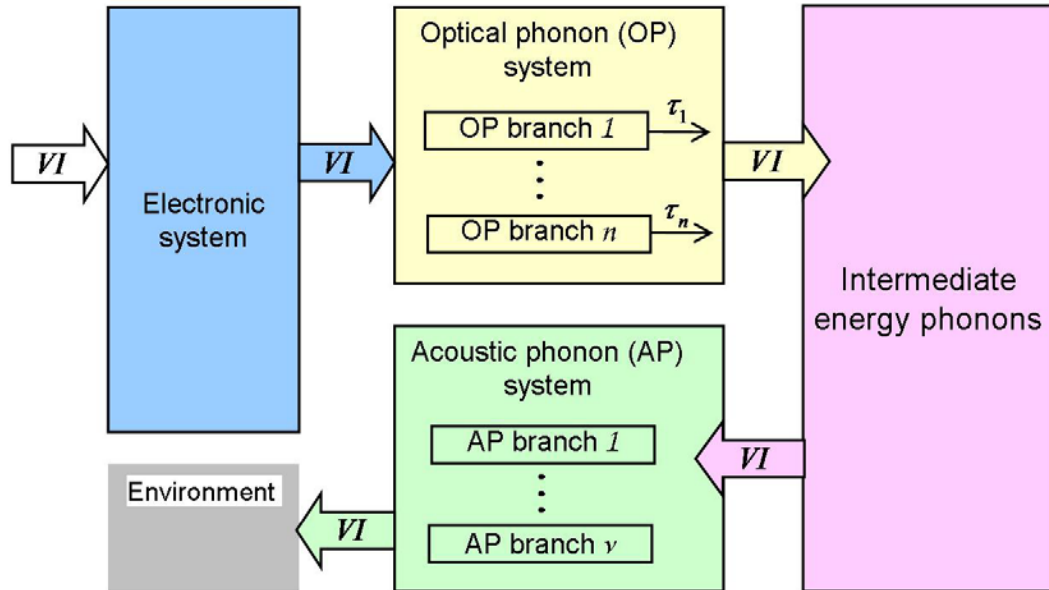


Fig. 3.8. Energy flow diagram. Power, VI , flows from battery to the electronic system. Electrons dissipate this power to the optical phonon system by electron-phonon scattering. Optical phonons then breakdown into intermediate-energy phonons and eventually into acoustic phonons. Acoustic phonons, which is nothing but heat, then flows out of the system and the power, VI , flows out as heat flux.

tronic system, the optical phonon system, the intermediate energy phonon branches, the acoustic phonon system, and the environment. Power, VI , first flows from battery to the electrons, which dissipate this power to the optical phonon system by

emitting optical phonons. The optical phonons then breakdown into intermediate energy phonons by anharmonic phonon-phonon coupling [66] and eventually into different branches of acoustic phonons and leave the system as heat. The population of the optical phonons depend predominantly on the optical phonon generation rate and thus on electron-phonon coupling. Population of the acoustic phonons, on the other hand, depends on the fraction of optical phonons that in-scatter to a particular acoustic phonon branch. To calculate this properly, BTE of all the intermediate phonon branches, through which an optical phonon decays to a particular acoustic branch needs to be solved. This is clearly a much harder problem. Enormous simplification is possible if we note that, the transport of acoustic phonons is nothing but the heat-flow, with Joule-heating power of VI . Next we assume that the population of the acoustic phonons is essentially given by a Bose-Einstein distribution evaluated at the temperature obtained by solving the heat-equation. Note that this comes automatically from the BTE of Eq. (3.26). For example, at steady-state the left hand side of Eq. (3.26) is zero and for the acoustic phonon branch, $G_\nu \approx 0$, thus we get

$$n_{\nu,ss} \approx G_\nu \tau + n_{\nu,0}(T) \approx n_{\nu,0}(T). \quad (3.32)$$

This scheme is shown in Fig. 3.9 For carbon nanotubes, the heat-equation takes the following form,

$$\nabla_x (\kappa(T) \nabla_x T) - g(T - T_0) = -I \frac{-dF_n}{dx}, \quad (3.33)$$

where, g is tube-substrate thermal coupling and is found to be $0.18W/m/K$ by fitting the tube burning data. The thermal conductivity, $\kappa(T)$ is assumed to be varying with the temperature as $\kappa(T) = \kappa_0(T_0/T)$, due to Umklapp process (U-process) [66], where, $\kappa_0 = 3000W/m/K$, [79] and $T_0 = 300K$. The right hand side is the Joule heating density calculated using the current and the quasi-Fermi level, $-dF_n/dx$. The quasi-Fermi level is calculated by equating the charge density obtained self-consistently, to the 1D equilibrium distribution and then back-calculating the Fermi-level from there. The heat equation is solved by discretizing on a finite difference grid.

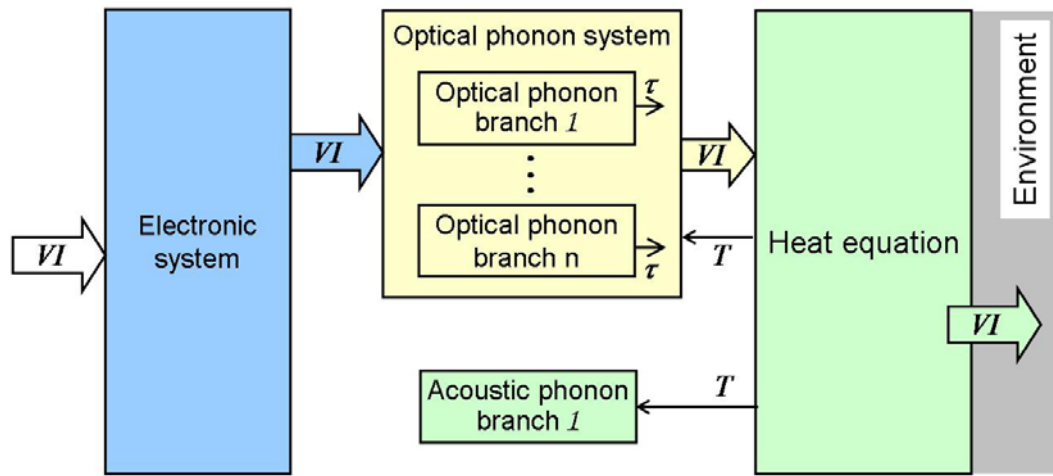


Fig. 3.9. Modified energy flow diagram. Power, VI , flows from battery to the electronics to the optical phonons to the heat-equation and then to the environment. The local temperature, $T(x)$, obtained by solving the heat-equation is then fed back to the phonon BTEs.

3.6 Summary

In this chapter a coupled electron-phonon BTE solver was described. The full expressions for the bandstructure for electron and phonon are used to describe their dynamics. For electrons, microscopic full-band scattering rates are used involving two phonon subbands and five relevant phonon branches. For phonon-phonon scattering and to capture the lattice anharmonicity, a macroscopic relaxation rate approximation has been used. Phonon life-times are calibrated using the experimental data of metallic tubes. To assess the self-heating of the tube, heat-equation is also solved and is calibrated using the tube burning data. The model will be used in Chapter 5 to evaluate the performance of an idealized CNT-MOSFET.

4. HOT PHONON EFFECT IN METALLIC CARBON NANOTUBES

4.1 Introduction

Phonon scattering plays an important role in determining electronic, optoelectronic, and heat transport properties in carbon nanotubes (CNTs). Correct determination of electron phonon coupling (EPC) is essential in explaining these transport experiments. The EPC calculated in the previous chapter will now be used with the Boltzmann transport equation (BTE) to analyze the I-V characteristics of metallic single walled carbon nanotubes (mSWNTs) under high-field conditions. Two types of experiments, one for tubes supported on a solid substrate [46–48] and the other for tubes suspended over a trench [80] have been reported in the literature. The physical condition of the tube is different in these experiments. The presence of substrate could change the phonon life-time (due to anharmonic effect) of the tube, as well as its thermal coupling to the substrate, as a result a change in electrical characteristics is expected.

We start with on-substrate tubes, where, by calibrating the tube-substrate thermal coupling using the burning data [47,81], we show that the heating has minimal effect on the I-V. We also show that, the current saturation observed in longer ($L \geq 300nm$) tubes around $\sim 20\mu A$, [46–48] results from an increased phonon scattering. This hot-phonon effect, necessary to explain the measured data, is captured by solving a coupled phonon BTE. Ignoring the hot-phonon effect requires an artificially high EPC, equivalent to a mean free path (mfp) of $10 - 15nm$ [46–48], which is an order of magnitude shorter than the theoretically calculated value [49,50,82]. Recent work by Lazzeri et al. [83] also showed this by solving a coupled electron-phonon BTE, but for longer tube length ($300nm$) only. Their work, like the previous ones, assumed

linear crossing bands for the metallic tubes around the Fermi points. When the tube length is smaller ($L < 300nm$), this linear band approximation breaks down because electrons start to occupy the non-linear portion of the band, and it is not enough just to include the hot phonon effect to reproduce the measured data. To reproduce the measured data of smaller tubes using the same set of physical parameters as was used for longer tubes, the complete metallic bands have to be considered.

Next, we look at the suspended tubes where, long tubes ($> 800nm - 11\mu m$) are free standing over a trench. Experiments by Pop et al. [80] show that current in a suspended tube is much smaller than in similar substrate supported tubes (same length and diameter). Moreover, suspended tubes show negative differential resistance (NDR) at high-fields. Using a phenomenological model, Pop et al. attributed these to the hot-phonon effects. Here, we separate the role of hot-phonon and self-heating effects and show that, the NDR results from poor heat-removal of the suspended tube, thus is the manifestation of the self-heating effect, while the hot-phonons reduce the overall current level. Although self-heating gives NDR, it alone cannot reproduce the experimental data. Better match with the experiment is possible only by including the non-equilibrium optical phonon population with life-time similar to that of tube on substrate. Reproduction of the measured data using the self-heating effect [84] is only possible by assuming optical phonon mean-free path of $\sim 25nm$ (corresponding relaxation time: $\tau = \ell/v = 30fs$) and simultaneously assuming a much smaller thermal conductivity of : $2000W/m/K$, which is well below the experimentally reported range of: $2800 - 3900W/m/K$ [79].

The chapter is organized in the following way: in Secs. 4.2 and 4.3 the physics of phonon scattering in metallic CNT is discussed and the rates for various scattering processes are calculated. Transport equations are described in Sec. 4.4. Next the developed model is applied to the analysis of on-substrate metallic tube data in Sec. 4.5 followed by a discussion of suspended tube transport in Sec. 4.6. Finally in Sec. 4.7 tube burning and the variation of thermal conductivity with temperature is discussed.

4.2 Bandstructure of the metallic tube

Let us begin with the bandstructure of an armchair tube. Only an armchair type metallic tube is considered in this work for simplicity, the effect of chirality will be explored in future work. In the tight binding p_z orbital description the bandstructure of an armchair tube is [65]:

$$E = \pm t_0 \sqrt{1 + 4 \cos\left(\frac{\nu\pi}{n}\right) \cos\left(\frac{k\sqrt{3}a_{cc}}{2}\right) + 4 \cos^2\left(\frac{k\sqrt{3}a_{cc}}{2}\right)} \quad (4.1)$$

where, $t_0 = 2.6eV$ is the hopping parameter, $a_{cc} = 1.42 \times 10^{-10}m$ is the c-c bonding distance, and the $+$ and $(-)$ signs are used for the conduction and valence bands respectively. When, $\nu = 0$ the conduction and valence bands cross each other near the Fermi points, $k_F = \pm 2\pi/3\sqrt{3}a_{cc}$ giving the metallic nature to the armchair tube. Putting $\nu = 0$, and making the substitution, $k = k_t + 3k_0/2$ in Eq. 4.1, we get:

$$E = \pm t_0 \left(1 - 2 \cos\left(\frac{k_t\sqrt{3}a_{cc}}{2}\right) \right), \quad (4.2)$$

where, $k_0 = 2k_F = 4\pi/3\sqrt{3}a_{cc} \approx 1.7 \times 10^{10}m^{-1}$. Figure 4.1 shows these metallic bands, the k -space, and the Brillouine zone of armchair tube.

4.3 Electron phonon scattering

Scattering within the metallic bands does not change the transverse momentum, hence only phonons with zero transverse momentum are involved in such scattering. These phonons belong to the $n = 0$ phonon subband, where there are 6 phonon branches. Only 3 of these 6 branches: twiston (TW), longitudinal optical (LO), and transverse optical (TO) have nonzero EPC. Among them, TW is responsible for the acoustic phonon scattering, while LO and TO are responsible for the high-energy optical phonon scattering. Unlike semiconducting tubes, the radial breathing mode (RBM) does not have strong EPC in metallic tubes. Figure 4.2 shows dispersion of these phonon branches.

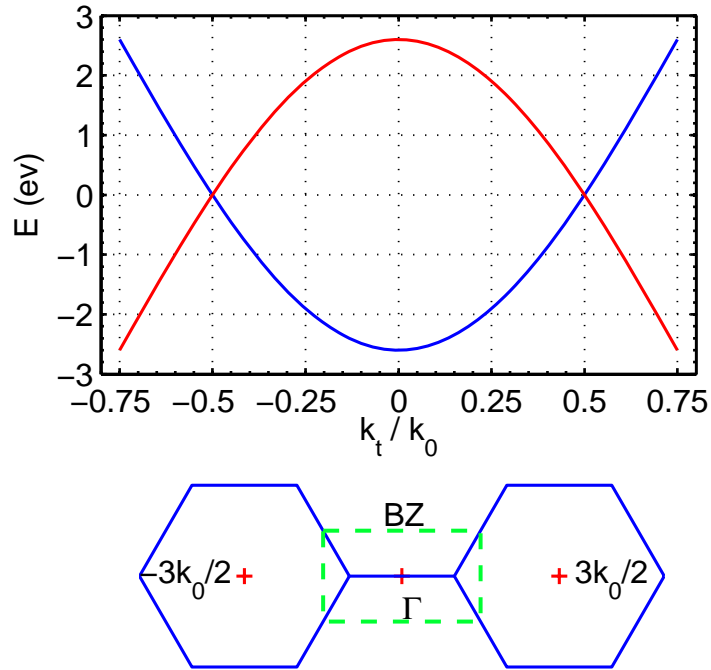


Fig. 4.1. Upper panel: Metallic band E - k in armchair tube. Here, $k_0 = 1.7 \times 10^{10} m^{-1}$. At the Γ point, conduction band energy is $E_c = -t_0 = -2.6 eV$. Crossing of the conduction and valence bands occur at $k_t = \pm 0.5 k_0$. Lower panel shows the k -space of the armchair tube. The dashed rectangular box is the Brillouine zone (BZ). E - k in the upper panel is drawn over the full range of the BZ.

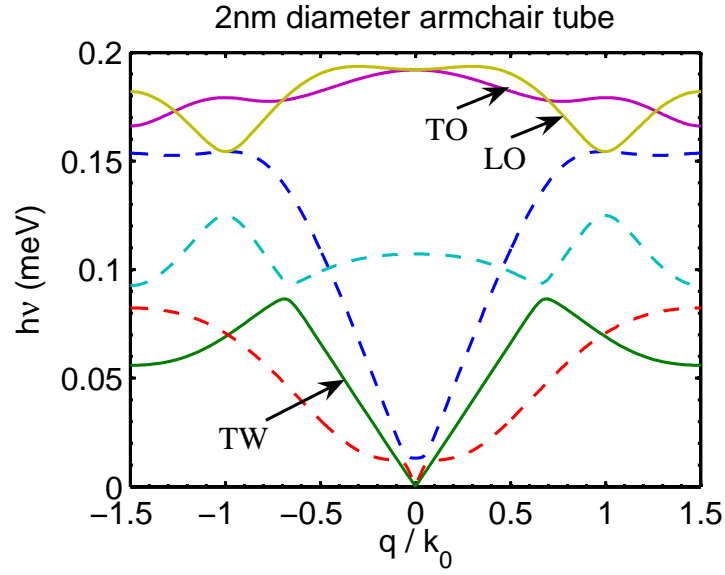


Fig. 4.2. Phonon dispersion of $n = 0$ phonon subband of a 2nm diameter armchair tube. Solid (dashed) lines have nonzero (zero) EPC. Note that, $q = k_0$ is the graphene Brioulline zone (BZ) boundary, where, $k_0 = 4\pi/3\sqrt{3}a_{cc} = 1.7 \times 10^{10}m^{-1}$. The TW, LO, and TO assignments are valid only near the Γ point, however, we will use these labes to represent the entire branch.

Phonons can cause the electron to scatter within the conduction or the valence band (intra-band scattering) or it can cause scattering from conduction to valence or valence to conduction band (inter-band scattering). Possible outscattering for intra and inter-band processes are shown in Fig. 4.3. Here, processes involving zone-

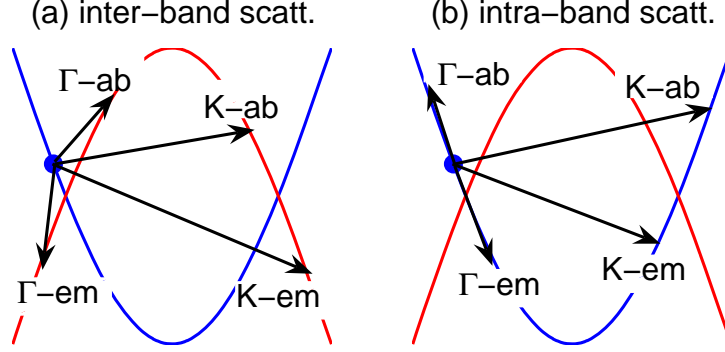


Fig. 4.3. (a) Inter-band scattering. (b) Intra-band scattering. The emission process involves both the zone-center and zone-boundary phonons, denoted by Γ_{em} and K_{em} respectively. Similarly the absorption process involves Γ_{ab} and K_{ab} processes.

center phonons are labeled as Γ processes ($\Gamma - ab$, $\Gamma - em$) and processes involving zone-boundary phonons are labeled as K processes (K-em, K-ab). It is found that TW and LO branches cause inter-band scattering only while the TO branch causes intra-band scattering. The final states of scattering are calculated using the energy and momentum conservation rules, for which the full electron and phonon dispersion relations of Figs. 4.1 and 4.2 have been used. The scattering rate of these processes are calculated using the Fermi's Golden rule (FGR) [61]:

$$\frac{1}{\tau(k, k_f)} = \frac{2\pi}{\hbar} |\Xi(k, k_f)|^2 DOS(k_f), \quad (4.3)$$

where, k and k_f are the initial and final states of scattering, $\Xi = \chi V_{ep}$ (χV_{ep} are defined in Eq. (2.38)) is the EPC of the associated phonon branch, and $DOS(k_f)$ is the density at the final states. Figure 4.4 shows the calculated scattering rates for TW, LO and TO branches.

4.3.1 Twiston mode

Scattering rates of the TW branch are shown in Figs. 4.4a, 4.4b. Only inter-band scattering rates are shown, since, intra-band scattering rates are zero. It is seen that, TW only causes zone-center scattering. At room temperature, acoustic phonon population becomes: $n(q) \approx (1 + n(q)) \approx k_B T / \hbar \omega = k_B T / \hbar q v_s$, where, v_s is the sound velocity. Using this phonon population and the calculated relaxation rates, the non-degenerate outscattering mfp for a Fermi point electron becomes: $\ell_{TW}^\Gamma = v_F \tau = 900nm$, Where,

$$\frac{1}{\tau} = \left\{ \frac{1}{\tau(k_F, k_{\Gamma-em})} + \frac{1}{\tau(k_F, k_{\Gamma-ab})} \right\} \frac{k_B T}{\hbar q v_s}, \quad (4.4)$$

$v_F = 3a_{cc}t_0/2\hbar = 8.45 \times 10^5 m/s$ is the Fermi velocity, and v_s is calculated from Fig. 4.2. We found that this mfp is proportional to diameter and in general, for a tube with diameter d , the acoustic phonon mfp would be $450d$.

4.3.2 LO mode

Like TW, the LO branch also causes the inter-band scattering and also the zone-boundary scattering is weak compared to the Γ phonon scattering. At the Fermi point, the mfp due to Γ phonon emission is: $\ell_{LO}^\Gamma = v_F \tau(k_F, k_{\Gamma-em}) \approx 300nm$ for a 2nm diameter tube. If the diameter is d the, $\ell_{LO}^\Gamma = 150d$. Energy of the LO mode at Γ point is 0.195eV.

4.3.3 TO mode

Finally we consider the TO mode scattering which is shown in Figs. 4.4e, 4.4f. Unlike TW and LO, TO causes intra-band scattering and here both zone-center and zone-boundary phonons are important. At the Fermi point, the mfp for the zone-center phonon scattering is, $\ell_{TO}^\Gamma = 290nm$, and for the zone-boundary phonon scattering is, $\ell_{TO}^K = 140nm$, both for a 2nm diameter tube. If tube diameter is d then,

$\ell_{TO}^\Gamma = 145d$ and $\ell_{TO}^K = 70d$. Energy of the TO mode near zone-center and zone-boundary are 0.195eV and 0.183eV respectively.

4.4 Transport equations for electron, phonon and heat

In metallic tube, the electrons in conduction and valence bands are described by two coupled BTEs. Each BTE is then coupled with the 3 phonon BTEs (for TW, LO, TO branches) through the collision integral, and finally the electron and phonon BTEs are coupled with the heat equation. We consider the electron BTE first:

$$\partial_t f_c = -v_c \partial_x f_c + \frac{q\mathcal{E}}{\hbar} \partial_k f_c + \sum_{\alpha} S_{c,\alpha}, \quad (4.5)$$

$$\partial_t f_v = -v_v \partial_x f_v + \frac{q\mathcal{E}}{\hbar} \partial_k f_v + \sum_{\alpha} S_{v,\alpha}, \quad (4.6)$$

where, subscript c (v) denotes the conduction (valence) band, f , v , and S are the electronic distribution function, group velocity ($\partial E/\hbar \partial k$), and collision integral respectively. Subscript α with the collision integral denotes the associated phonon branch which stands for TW, LO, or TO. The collision integral for a particular branch is calculated by summing the net in-scattering rates over all possible scattering process. For example, with TW branch, there are only $\Gamma - em$ and $\Gamma - ab$ processes (see Figs. 4.4a, 4.4b, and 4.3a) and the net in-scattering along these two paths are:

$$\begin{aligned} S_{c,TW} = & \frac{1}{\tau(k_{\Gamma-em}, k)} f_v(k_{\Gamma-em}) (1 - f_c(k)) n_{tw}(k - k_{\Gamma-em}) \\ & + \frac{1}{\tau(k_{\Gamma-ab}, k)} f_v(k_{\Gamma-ab}) (1 - f_c(k)) (1 + n_{tw}(k - k_{\Gamma-ab})) \\ & - \frac{1}{\tau(k, k_{\Gamma-ab})} f_c(k) (1 - f_v(k_{\Gamma-ab})) n_{tw}(k - k_{\Gamma-em}) \\ & - \frac{1}{\tau(k, k_{\Gamma-em})} f_c(k) (1 - f_v(k_{\Gamma-em})) (1 + n_{tw}(k_{\Gamma-em} - k)), \end{aligned} \quad (4.7)$$

where, $k_{\Gamma-em}$ and $k_{\Gamma-ab}$ are the final state due to $\Gamma - em$ and $\Gamma - ab$ processes, and n_{tw} is the TW mode phonon population. The collision integral for other branches are calculated similarly.

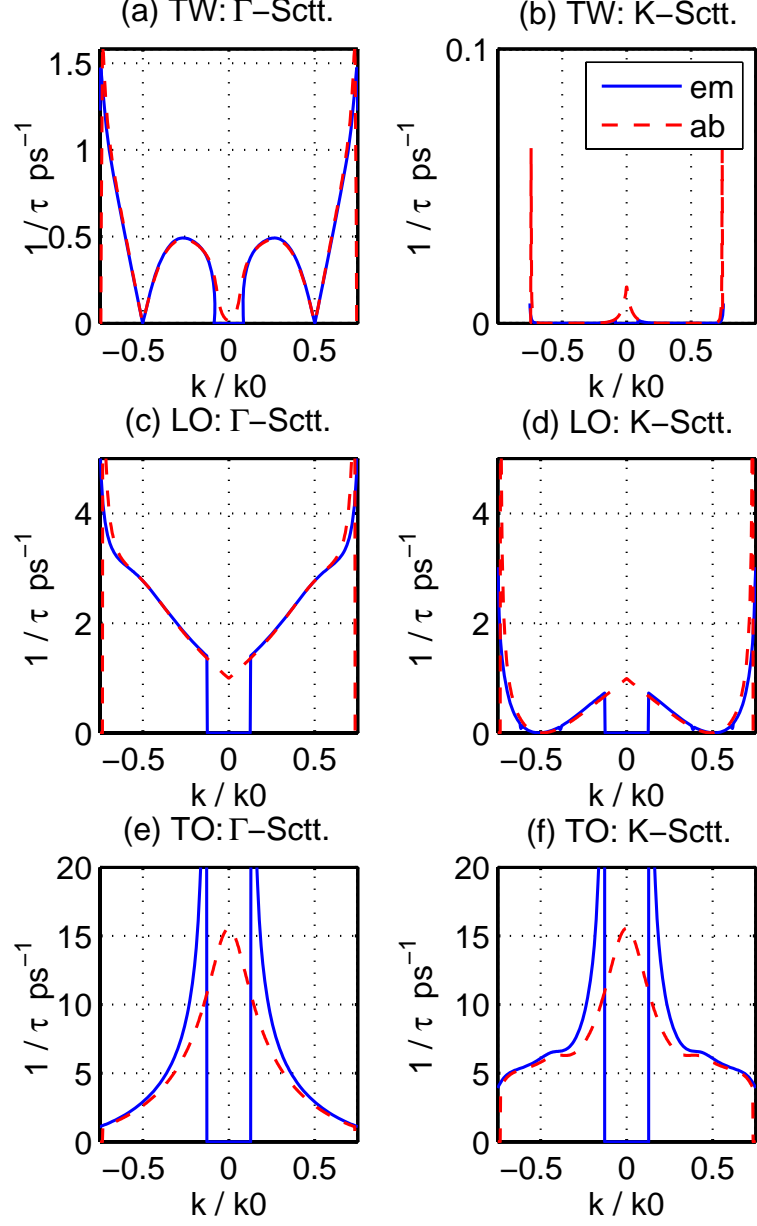


Fig. 4.4. Out scattering rates, $1/\tau(k, k_f)$ for TW, LO and TO branches. For TW and LO branches, inter-band scattering rates are shown (intra-band scattering rates are zero) and for TO branch, intra-band scattering rates are shown (inter-band scattering are zero in this case). These are full-band scattering rate calculation. All the left panels (a), (c), and (e) shows the rates involving Γ phonons and all the right panels show rates involving K phonons. Also, the solid lines are for emission processes, and the dashed lines are for absorption processes.

Next we consider the phonon BTE of a particular phonon branch α :

$$\partial_t n_\alpha = -v_\alpha \partial_x n_\alpha + G_\alpha - \frac{n_\alpha - n_o}{\tau_{op}}, \quad (4.8)$$

where, v_α is phonon group-velocity ($v_\alpha = \partial\omega_\alpha/\partial q$) calculated using phonon dispersion relation of Fig. 4.2, n_o is the equilibrium phonon population at a given temperature, τ_{op} is optical phonon lifetime, and G_α is the phonon generation rate due to electron-phonon scattering. Calculation of G_α is shown here for the TO branch. TO branch causes intra-band scattering as discussed earlier. A particular phonon mode, q , of TO branch is associated with 4 scattering processes two of them within the conduction band as shown in Fig. 4.5b giving a net generation rate of G_{TO}^c and the rest two within the valence band giving a net generation rate of G_{TO}^v . Total TO branch generation

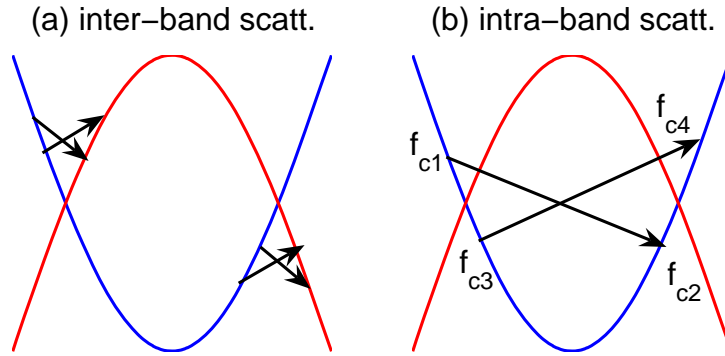


Fig. 4.5. Scattering processes associated with same phonon mode. These are list of all such k_i and k_f sets that give $k_f - k_i = q$, where q is a particular phonon wavevector. In (a) inter-band conduction to valence band processes are shown. Similar processes exist for valence to conduction transition which are not shown here. In (b) intra-band conduction to conduction processes are shown, while similar processes between valence to valence transition exists but not shown here.

rate is thus $G_{TO} = G_c^{TO} + G_v^{TO}$, where,

$$\begin{aligned} G_c^{TO} &= \frac{1}{\tau(k_1, k_2)} f_c(k_1) (1 - f_c(k_2)) (1 + n_{to}(q)) \\ &- \frac{1}{\tau(k_3, k_4)} f_c(k_3) (1 - f_c(k_4)) n_{to}(q). \end{aligned} \quad (4.9)$$

Here, $q = k_2 - k_1 = k_4 - k_3$. G_v^{TO} can be calculated in the similar manner but within the valence band. For inter-band scattering processes, there are 8 ways in which a particular phonon mode can be generated, 4 of which, shown in Fig. 4.5, are due to conduction to valence band scattering, and rest 4 are for valence to conduction band scattering. The generation rates for these processes are calculated in the similar way.

Finally to capture self-heating effect the heat equation is solved:

$$\frac{d}{dx} \left(A\kappa(T) \frac{dT}{dx} \right) - g(T - T_0) = -\frac{VI}{L}. \quad (4.10)$$

where, $\kappa(T) = \kappa_0 (T_0/T)^m$, with $\kappa_0 = 2800 \text{ W/m/K}$ [79], $T_0 = 300 \text{ K}$, and g is the tube-substrate thermal coupling parameter, and $A = \pi 0.34 \times 10^{-9} d$ is the heat conduction cross-section. Thermal conductivity exponent, m , can be either 1 or 2 depending on whether the thermal conductivity is limited by one or two phonon U-process respectively [66]. Value of g is estimated to be 0.18 W/m/K from the burning data of the tube. Starting with an initial temperature guess, the coupled electron-phonon BTEs are solved until steady-state is reached. The steady-state Joule heating, VI , is then used to calculate the new temperature and the whole process is repeated until self-consistency is achieved.

4.5 Transport in metallic CNTs on substrate

4.5.1 Hot phonon effect

We now apply the above model to the substrate supported metallic tubes. In Fig. 4.6a the effect of hot-phonons is examined. When only the electron BTE is solved, ignoring the scattering generated optical phonons, the simulation result cannot capture the current saturation behavior (unless we artificially reduce the mean-free path as has been done [46, 47]). The calculated scattering rate with equilibrium phonon population are not strong enough to reduce the current as observed in the experiments. The current saturation is observed in the simulation when the phonon BTE is included with the electron BTE. Inclusion of the phonon BTE takes the scattering

generated phonons into account, which drives the phonon population strongly out of equilibrium as shown in Fig. 4.7. This higher phonon population increases the scattering rates and leads to current saturation (Fig. 4.6a). Complete comparison of this model with experiment is shown in Fig. 4.6b with the optical phonon lifetime, τ , being the only fitting parameter. For completeness, self-heating is also included in these simulations, although its effect is not significant (for details see Sec. 4.7). In the thermal model, the tube-substrate thermal coupling parameter, g , is taken to be $0.18W/m/K$ – a value extracted from the tube burning data [81]. Four different tube lengths: $85nm$, $159nm$, $300nm$ and $700nm$ have been compared in Fig. 4.6b, using the phonon lifetimes $\tau = 1.5ps$, $1.5ps$, $2.5ps$, and $2.25ps$ to obtain the best fit. For all tubes, a $2nm$ tube diameter has been assumed. These values of phonon lifetime are consistent with the previously reported ones [77,78,85]. Note that the slight variation of τ in the simulation is expected due to the uncertainty in tube diameters.

4.6 Transport in suspended metallic tubes

4.6.1 Origin of NDR

We consider the suspended tubes now. Experimentally, the suspended tubes show much lower currents compared to similar tubes on substrate and also show negative differential resistance (NDR) [80]. In this section the origin of this NDR effect and the current lowering is investigated. There are two possible causes of NDR, one is the possibility of longer phonon life-times in suspended tubes. In principle this could happen since the tube is not in direct contact with the substrate so its dynamical behavior is not affected by it, leading to less anharmonicity and increased τ . The second possible cause could be the sharp rise in self-heating in suspended tube, due to the absence of tube-substrate thermal coupling ($g = 0$ for suspended tube). Both of these effects tend to increase the steady-state phonon population which can be approximated as (putting, $\partial_t n_\alpha = 0$ and $v_\alpha \partial_x n_\alpha \approx 0$ in Eq. 4.6): $n_{\alpha,ss} \approx n_0 + G_\alpha \tau$. Where, $n_{\alpha,ss}$ is the steady-state population of phonon branch α . Increased τ leads to

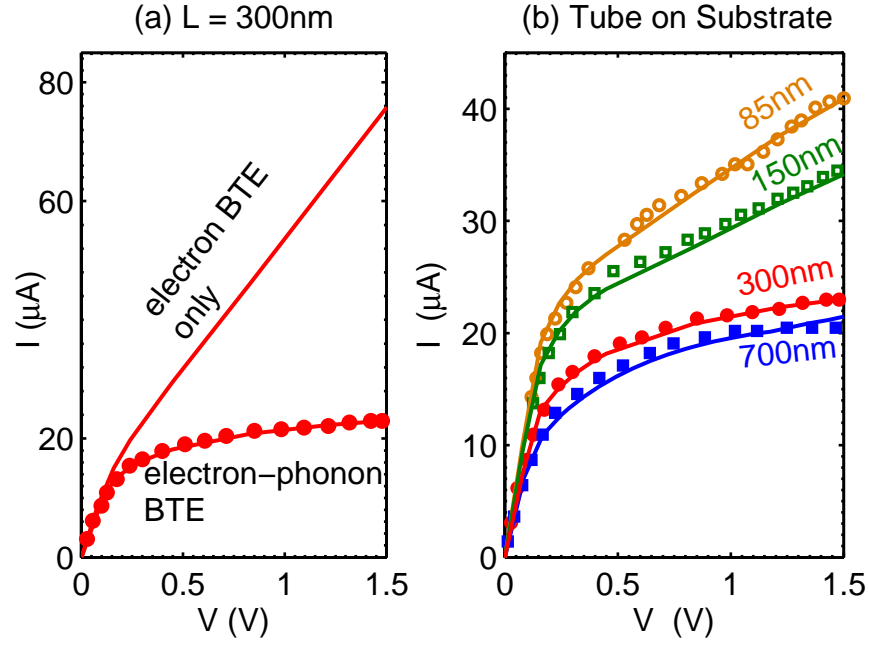


Fig. 4.6. Tube on substrate I-V. Solid lines are simulation and symbols are experimental data [47]. (a) Comparison of cold-phonon and hot-phonon simulation, where, solution of only the electron BTE is called the cold-phonon simulation, and solution of the coupled electron-phonon BTE is called the hot-phonon simulation. In (b) simulation result is compared with measured data of various tube lengths. Here, $d = 2\text{nm}$, $g = 0.18\text{W/m/K}$, and $\tau = 1.5\text{ps}, 1.5\text{ps}, 2.5\text{ps}$ and 2.25ps have been used for $L = 85\text{nm}, 150\text{nm}, 300\text{nm}$ and 700nm respectively.

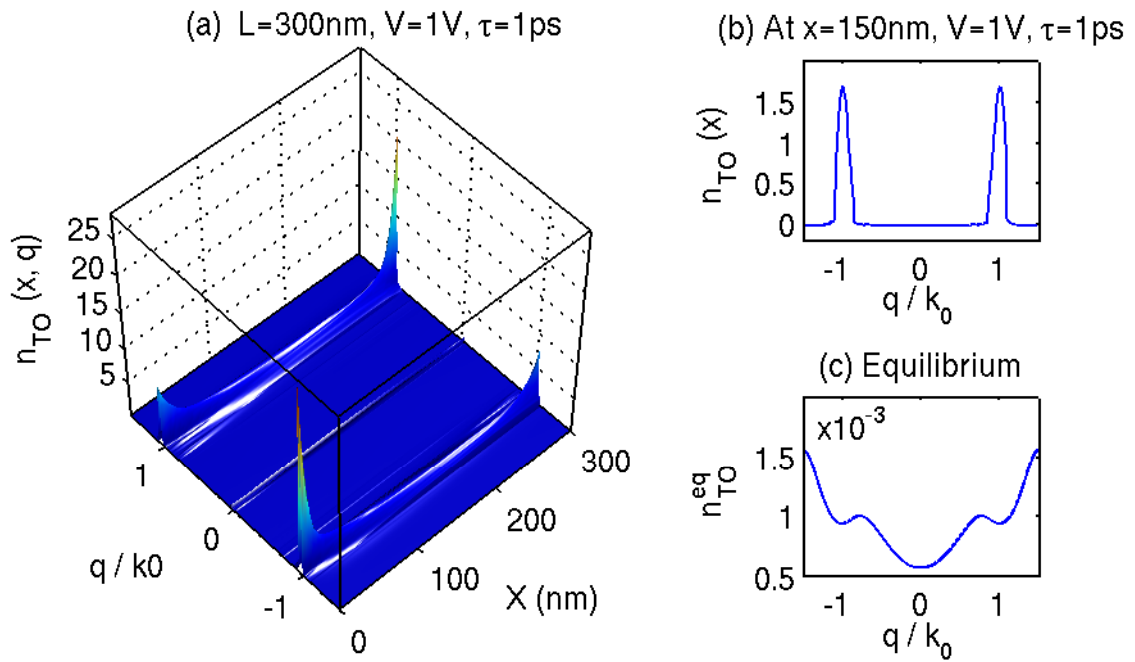


Fig. 4.7. (a) Population of TO mode in a 300nm long tube at 1V bias. 1ps phonon lifetime have been assumed here. (b) Phonon distribution at the middle of the tube. Near zone-boundary, at $q = k_0 = 1.7 \times 10^{10}\text{m}^{-1}$, population becomes 1.5. (c) Shows the equilibrium population for this branch. Clearly phonon population becomes extremely hot especially near the contacts as is shown in (a).

increased $G_\alpha\tau$, and increased T increases the thermally excited phonon population, n_0 . To check the relative importance of these two effects, let us start by putting $\tau = 0$, which means all the scattering generated phonons immediately decay out ($G\tau \rightarrow 0$) and only thermally generated hot-phonons remain in the system ($n_{ss} = G\tau + n_0(T) \approx n_0(T)$). The top curve labeled by (i) in Fig. 4.8 shows the simulation result under this condition, which clearly shows the NDR effect. Thus self-heating is responsible for the NDR. The reason self-heating gives NDR can be understood in the following way: In the heat equation (Eq. 4.10), putting $g = 0$ we get

$$\begin{aligned} T(x) &= T_0 \exp \left[\frac{VIL}{8\kappa_0 A T_0} \left(1 - \frac{4x^2}{L^2} \right) \right]; \quad m = 1, \\ T(x) &= \frac{T_0}{\left[1 - \frac{VIL(m-1)}{8\kappa_0 T_0 A} \left(1 - \frac{4x^2}{L^2} \right) \right]^{1/(m-1)}}; \quad m \neq 1, \end{aligned} \quad (4.11)$$

Here, m is either 1 or 2 depending on whether the thermal conductivity, κ , is limited by one phonon or two phonon U-processes [66] and A is the heat conduction cross-section. For a tube with diameter, d_t , and assuming the p_z orbital width is $b = 3.4\text{\AA}$, cross-section becomes, $A = \pi d_t b$. We see from Eq. 4.12 that the temperature varies exponentially (or even more sensitively for case of $m = 2$) with Joule heating. With the increased applied voltage current initially increases, however, the exponential rise in temperature eventually generates enough hot-phonons that the current starts to decrease giving the NDR.

Comparing with the experimental data (symbols in Fig. 4.8) we see that self-heating alone cannot give the match. Although recent work by Kuroda et al. [84] reproduced experiments using self-heating effect only, they had to use a much lower thermal conductivity of $\kappa_0 = 2000\text{W/m/K}$ [84] along with a very short optical phonon mfp of $\sim 25\text{nm}$. This value of thermal conductivity is well outside the experimentally estimated range ($2800 - 3900\text{W/m/K}$ [79]). Using this lower value of thermal conductivity with the calculated scattering rates, the dashed line labeled as (ii) in Fig.4.8 is obtained, which also does not give the fit. When $\tau = 2.25\text{ps}$ is used, however, the current drops down to the desired level giving good agreement with the measured data (curve (iii) in Fig.4.8). Thus in suspended tubes, both self-heating

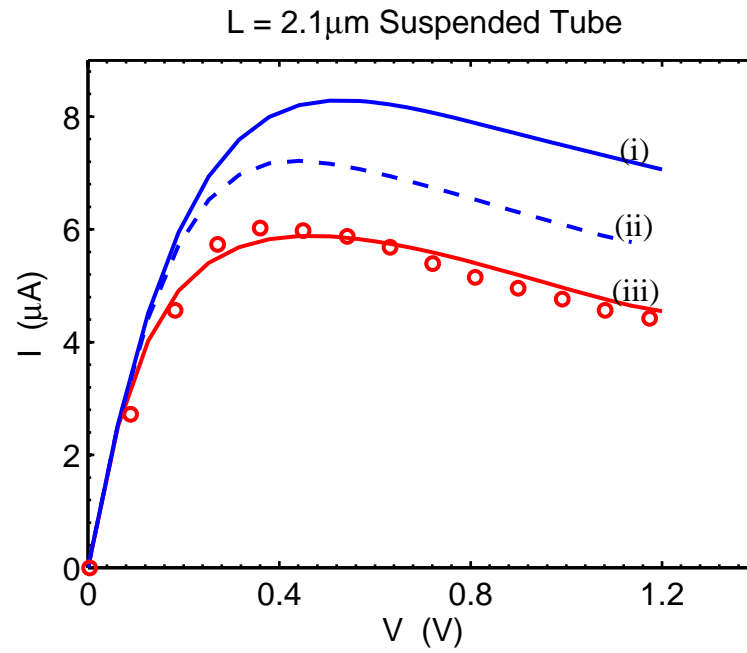


Fig. 4.8. Origin of NDR. (i) shows the I-V with the self-heating effect only. Here $\kappa_0 = 2800$ W/m/K, $d = 2nm$, $\tau = 0$ and $m = 2$ have been used. (ii) Similar calculation as (i) except $\kappa_0 = 2000$ W/m/K has been used. (iii) Both self-heating and hot-phonon are present with. Parameters are similar as (i) except, $\tau = 2.25ps$.

and hot-phonon effects are present, with self-heating being responsible for the NDR effect, and hot-phonon being responsible for the lowering of the current. Figure 4.9 shows the comparison of this model with experimental data. Following parameters have been used in the simulation: $\tau = 2.25ps$, $d = 2nm$, $g = 0$, $\kappa_0 = 2800Wm^{-1}K^{-1}$, and $m = 2$. A discussion on thermal conductivity exponent follows in Sec.4.7. Since, similar values of τ were also found in substrate supported tubes, we conclude that, the presence of substrate does not change the optical phonon lifetime significantly.

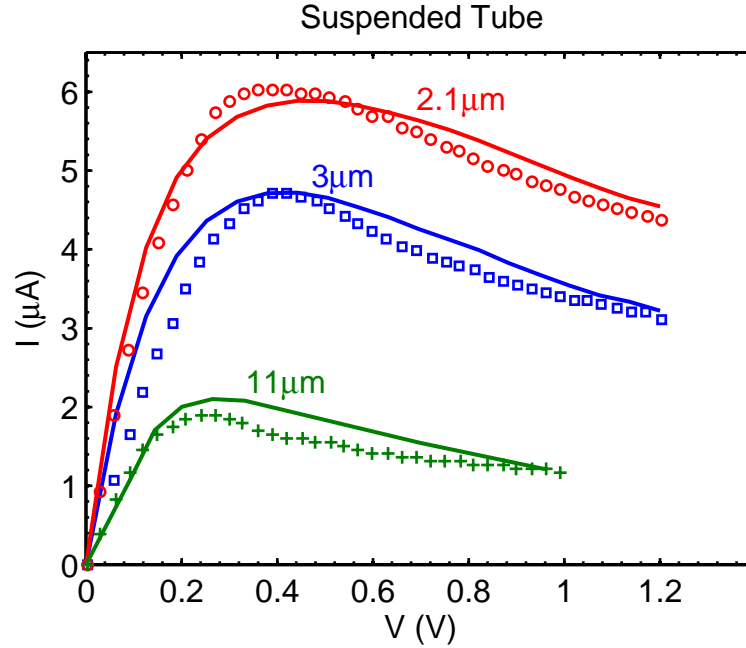


Fig. 4.9. Simulation of suspended tubes of various lengths. Symbols are experimental data [80], solid lines are simulation. Following parameters are used for the simulation: $d = 2nm$, $2nm$, and $3nm$ for $L = 2.1\mu m$, $3\mu m$ and $11\mu m$ tube. In all cases, $\tau = 2.25ps$, $\kappa_0 = 2800 W/m/K$, and $m = 2$ have been used.

4.7 Self-heating of the tube

The heating of the tube is discussed in this section. Consider the heat equation

$$\frac{d}{dx} \left(\kappa(T) \frac{dT}{dx} \right) - g(T - T_0) = -\frac{VI}{L}, \quad (4.12)$$

where, $\kappa(T) = \kappa_0 (T_0/T)^m$. For longer tubes on substrate, the diffusion term is negligible ($d/dx \rightarrow 0$), and Eq.4.12 simplifies to: $T \approx T_0 + VI/gL$. In long tubes, current saturate at high bias near burning. Using this saturation current, the burning bias for long tube can be expressed as

$$V_{BV} = \frac{(T_{BV} - T_0) gL}{I_{sat}}, \quad (4.13)$$

where, $T_{BV} = 850K$, is the oxidation temperature of carbon nanotube [86], and $I_{sat} \approx 20\mu A$. [46] Thus for longer tubes the burning bias scales linearly with length with g being proportional to the slope. Fitting a straight line through the burning bias data [81] g is estimated to be 0.18 W/m/K . This value of g is then used to predict the burning bias of smaller tubes, where neither the current saturates nor the diffusion term is negligible. The solid line in Fig. 4.10 shows the simulation result. Good agreement is found between the simulation and measured data. Having established the burning bias, this value of g is then used in the rest of the simulations for the on-substrate tubes.

Using the extracted value of g the temperature rise in substrate supported tube is examined. Figure 4.11a shows the temperature profile of a $700nm$ tube at $VI = 20\mu W$ Joule heating input. Thermal conductivity exponent, $m = 1$ is assumed for the purpose of illustration. Temperature distribution of a similar suspended tube is also shown by the dashed line in the same plot. Clearly the temperature increases dramatically in suspended tubes at the same power input (due to exponential dependence on Joule heating). In both cases peak temperature occurs at the middle. Figure 4.11b shows how the peak temperature scales with length. For on-substrate tube, at large lengths the peak temperature increases as $1/L$ as the tube length is shortened, reaching a maximum around $L \sim 500nm$. If tube length is shortened further temperature starts to drop down instead of increasing. This happens because if the length becomes too small (here $< 500nm$) diffusion through the contacts starts to dominate lowering the overall temperature. Thus the most severe self-heating effect for on-substrate tubes is expected to occur at $500nm$ length. We thus consider a $500nm$ tube at $1V$ bias, which should have current $\sim 20 - 40\mu A$ giving a Joule power of $\sim 20 - 40\mu W$.

At this power the peak temperature rises to $\sim 500K$ as seen in Fig. 4.11b, which gives a thermal population of 0.015 for the TO branch near zone boundary. This population is orders of magnitude smaller than the steady-state phonon population observed in similar tubes at 1V (see Fig. 4.7b). Thus self-heating should not have significant effect on the I-V of on-substrate tubes. At longer tube lengths, the electric field is smaller at same bias, leading to smaller scattering generated phonons population, however, temperature also falls off as $1/L$ giving a exponentially smaller contribution to the thermally excited phonons. Thus for on-substrate tubes the effect of self-heating on I-V is minimal.

For the suspended tube on the other hand, temperature increases exponentially (Eq. (4.12)) with tube length and Joule heating (4.12) as seen by the dashed lines in Fig. 4.11. It is this exponential rise in temperature at comparatively smaller bias, that is responsible for the NDR and reduced current in suspended tubes. Unlike the on-substrate tubes, the contribution of self-heating is always important in experimentally reported suspended tubes because: i) temperature is larger in suspended tubes even at smaller bias, giving a higher n_0 and ii) the electric field is smaller since the tubes under consideration are long; this reduces the scattering generated optical phonon component, $G_\alpha\tau$ of the steady-state population. Finally we consider the effect of thermal conductivity exponent, m . Starting with $\tau = 2.25ps$ and $m = 1$ for a $3\mu m$ long suspended tube, the top dashed line of Fig. 4.12 is produced; here the current is overestimated. Increasing phonon lifetime to $\tau = 5.5ps$ does not help as shown by the second dashed line in the same figure. Only by using $m = 2$ exponent in the thermal conductivity along with $\tau = 2.25ps$ fit with experimental data is obtained. Physically this means the thermal conductivity is limited by two phonon U process at higher temperatures; a feature also observed by Pop et al. [79].

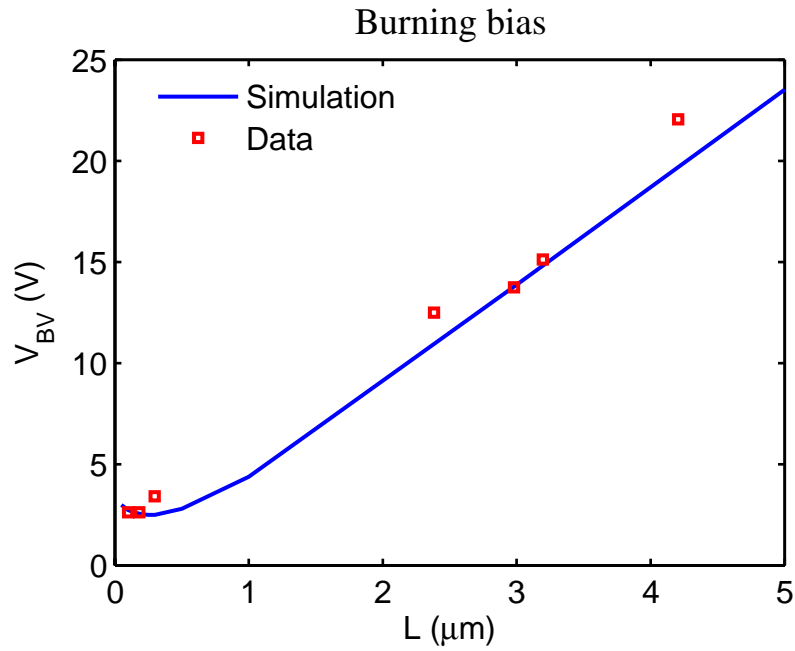


Fig. 4.10. Burning bias vs. tube length. Symbols are measured data [81], solid line is simulation. Value of thermal coupling parameter, g is extracted to be 0.18 W/m/K.

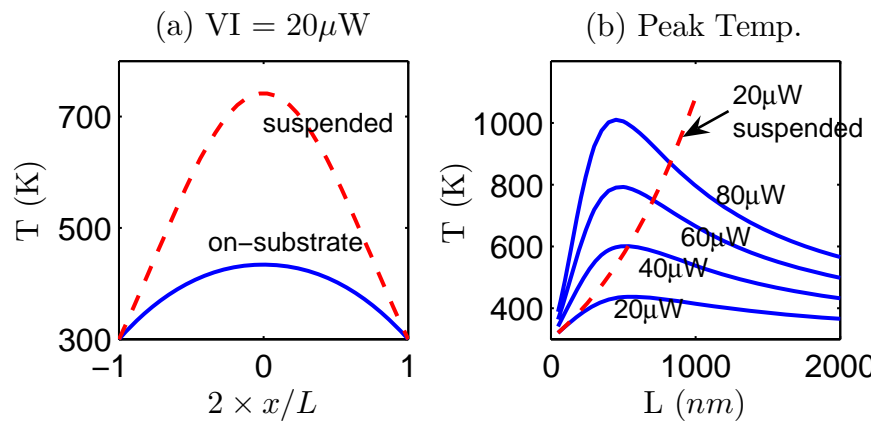


Fig. 4.11. (a) Temperature profile of 700nm on-substrate (solid line) and suspended (dashed line) tube at a fixed power input of $20\mu W$. (b) Scaling of peak temperature with length at various input power. Solid lines are for on-substrate tubes, and the dashed line is for suspended tube with $20\mu W$ power input. In all cases, $m = 1$ has been used in the heat equation (Eq. 4.10).

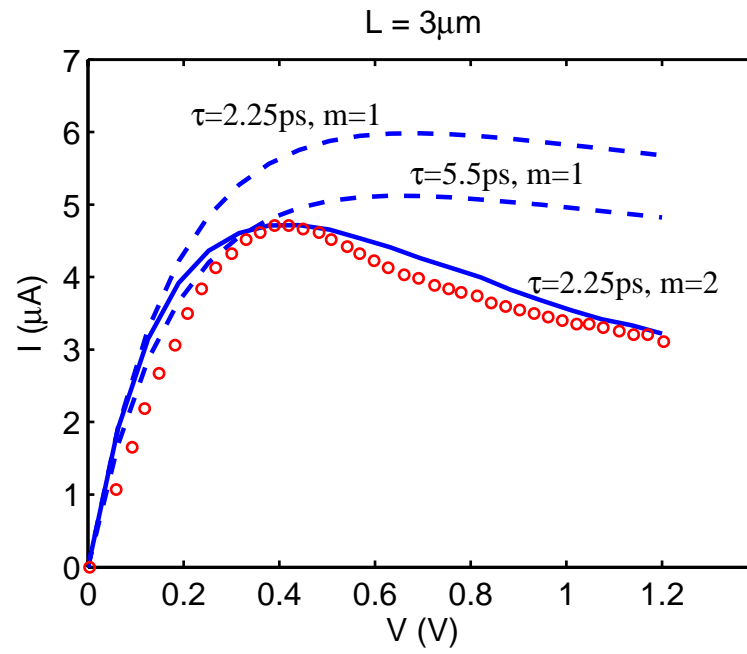


Fig. 4.12. Effect of thermal conductivity exponent. The top dashed lines are with $m = 1$ and the solid line is with $m = 2$. Symbols are experimental data.

4.8 Summary

To summarize, in this chapter we have considered metallic single walled carbon nanotubes, both sitting on a solid substrate and suspended over a trench. By using the calculated electron-phonon scattering rates and a single fitting parameter (optical phonon life-time) experimental data of substrate supported tube and suspended tubes of various lengths have been reproduced with good accuracy, using a full-band coupled electron-phonon BTE and heat transport equation. In particular It has been shown that, for tube on substrate, the current saturation observed in long tubes results from hot-phonon effects and that the optical phonon population is significantly out of equilibrium. Due to the presence of tube-substrate thermal coupling in substrate supported tubes, self-heating is not significant enough to affect the I-V characteristics. For suspended tube on the other hand, the observed NDR effect originates from the self-heating effect, and the hot-phonons generated from electron-phonon scattering reduces the overall current level. No significant change in phonon lifetime has been observed in suspended tubes. Analysis of the thermal model also show that the thermal conductivity varies as $1/T^2$ at high temperature indicating that the thermal conductivity is limited by two phonon U-process.

5. SIMULATION OF CARBON NANOTUBE MOSFETS INCLUDING HOT-PHONON AND SELF-HEATING EFFECTS

5.1 Introduction

Due to their superior transport properties, semiconducting carbon nanotubes (CNT) may have potential applications in future nanoelectronic systems. Phonon scattering is known to be very strong in CNTs under high bias [46], so in assessing the performance of a CNT MOSFET it is important to include the phonon scattering. A recent experiment on suspended metallic tubes [80] showed the role of non equilibrium phonon population (hot-phonon effect) on determining the IV characteristics of the tube. It was also suggested that, heating can become important [81] in short tubes because the power density can be particularly high. In the present work, we solve a coupled electron-phonon Boltzmann transport equation (BTE) and heat equation to include the effect of phonon scattering, hot-phonon effect and self-heating effect on assessing the performance of a short CNT MOSFETs.

5.2 Scattering in zigzag tubes

5.2.1 Bandstructure

For FETs, a bandgap of $\sim 1eV$ is preferable, so we consider a (13,0) zigzag tube with a bandgap of $\sim 0.8eV$. Figure 5.1 shows the bandstructure of the first subband. The full tight binding E-k (not effective mass) relationship has been used in this work which is [65]:

$$E = t_0 \sqrt{1 + 4 \cos\left(\frac{\pi m}{n}\right) \cos\left(\frac{3ka_{CC}}{2}\right) + 4 \cos^2\left(\frac{\pi m}{n}\right)} \quad (5.1)$$

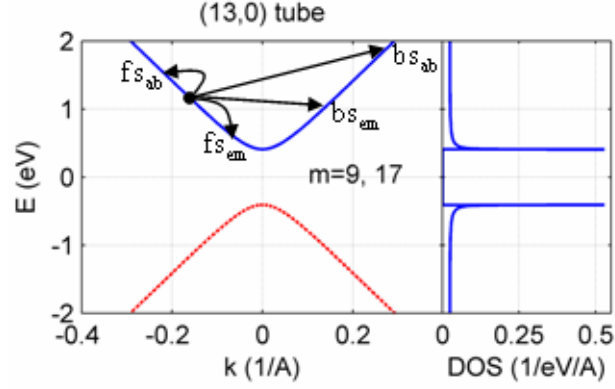


Fig. 5.1. First subband of a (13,0) tube is doubly degenerate and corresponds to subband indices are $m = 9$ and 17 . Four possible scattering mechanisms, fs_{ab} , fs_{em} , bs_{ab} , and bs_{em} are shown.

where, $t_0 = 2.6\text{eV}$, $m = 9$ or 17 , $n = 13$, and $a = 1.42 \times 10^{-10}\text{m}$. The second subband is $\sim 0.6\text{eV}$ above the first one, and is neglected in this work. The first subband is doubly degenerate and corresponds to subband indices of $m=9$ and 17 . The ‘zone center’ phonons belongs to $n=0$ phonon subband. These phonons cause intra-valley scattering where the electrons do not change their transverse momentum, thus keeping the subband index, m , unchanged after scattering ($9 \leftrightarrow 9$ or $17 \leftrightarrow 17$). On the other hand, the ‘zone boundary’ phonons, which belong to $n = (17 - 9) = 8$ phonon subbands, cause inter-valley scattering where the electrons scatter within the doubly degenerate 1st subbands ($9 \leftrightarrow 17$), and change their transverse momentum by $\sim \pm 4\pi/3\sqrt{3}a_{cc}$. Figures 5.2a and 5.2b show the phonon branches of $n = 0$ and $n = \pm 8$ phonon subbands, respectively. For each of these 12 phonon branches, there are 4 possible scattering processes, these are: forward scattering by emission (fs_{em}), forward scattering by absorption (fs_{ab}), backward scattering by emission (bs_{em}), and backward scattering by absorption (bs_{ab}) (see Fig. 5.2).

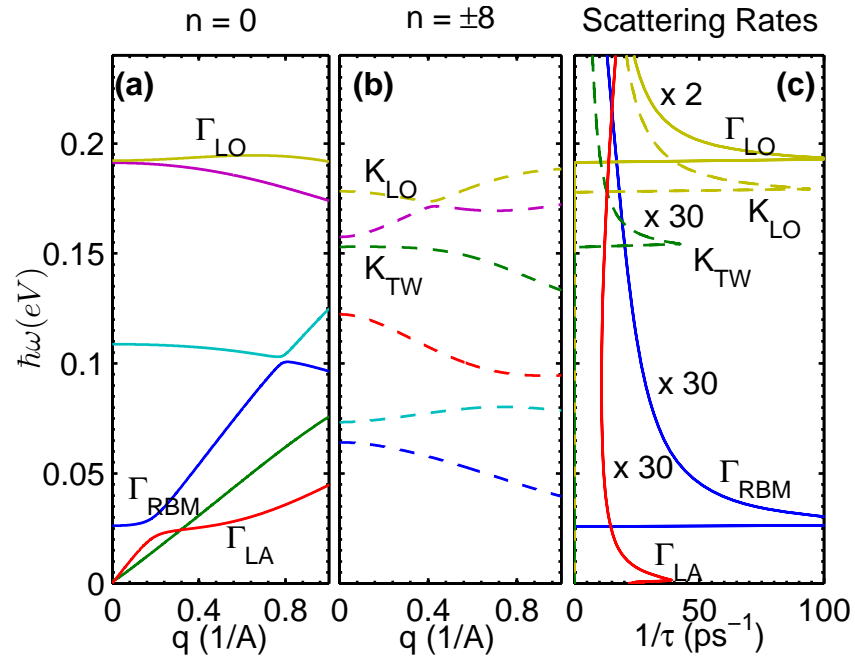


Fig. 5.2. Phonon dispersion branches of a (13,0) tube belonging to (a) $n=0$ phonon subband, and (b) $n=8$ phonon subbands. (c) Total backscattering rates ($bs_{em} + bs_{ab}$) at room temperature. For LA mode both emission and absorption rates contribute, while for all other modes absorption is negligible at 300K.

5.2.2 Scattering rates

The scattering rate corresponding to each of these processes discussed above is calculated using Fermi's golden rule [61]:

$$\frac{1}{\tau_{k,ab}} = \frac{2\pi}{\hbar} (J_1 |\Xi(k, k_{f,j})|)^2 DOS(E_{f,j}) n_{op}(q_j), \quad (5.2)$$

$$\frac{1}{\tau_{k,em}} = \frac{2\pi}{\hbar} (J_1 |\Xi(k, k_{f,j})|)^2 DOS(E_{f,j}) (1 + n_{op}(q_j)), \quad (5.3)$$

where, for emission processes, $j = 1, 2$, and for absorption processes, $j = 3, 4$, n_{op} is the population of the associated phonon mode ($q_j = k_{f,j} - k$), $J_1 = 5.5 \text{ eV}/\text{\AA}$ is the deformation constant [49], $\Xi(k, k_{f,j})$ is the matrix element for the particular transition, and $DOS(E_{f,j})$ is the density of states calculated at the final state. The final states $k_{i,j}$ are calculated using the electron and phonon branch dispersion relations in accordance with the momentum conservation rules. The matrix element $\Xi(k, k_{f,j})$ is calculated using the SSH scheme [49], which depends on initial and final electronic states and also on the phonon mode eigenvectors. Figure 5.2c shows the calculated backscattering rates ($bs_{em} + bs_{ab}$) at room temperature. Only five out of 12 phonon branches contribute to scattering: $0.195 \text{ eV } K_{LO}$ branch, $0.183 \text{ eV } \Gamma_{LO}$ branch, $0.156 \text{ eV } K_{TW}$ branch, $0.025 \text{ eV } \Gamma_{RBM}$ branch, and the Γ_{LA} mode (only acoustic branch).

5.3 Simulation approach

A coupled electron phonon BTE is solved to simulate electron and phonon transport. The BTEs are:

$$\begin{aligned} \partial_t f &= -v_k \partial_x f + \frac{q\mathcal{E}}{\hbar} \partial_k f + S \\ \partial_t n_\alpha &= -v_{q,\alpha} \partial_x n_\alpha + G - \frac{n_\alpha - n_{eq}(q, T)}{\tau} \end{aligned} \quad (5.4)$$

here, f , n_α are the electron and phonon distribution functions, v_k , $v_{q,\alpha}$ are electron and phonon group velocities, \mathcal{E} is the local electric field, S is the collision integral, G is the phonon generation rate, and τ , phonon decay time. The 5 phonon branches

are labeled by $\alpha = 1 \cdots 5$ and include both optical and acoustic modes. Each emission scattering creates a phonon while each absorption annihilates one, thus the net generation G is the emission minus absorption at each phonon mode. These BTEs are coupled with the heat and Poisson equations and are solved self-consistently according to the scheme outlined in Figure 5.3. The classical heat equation used in this work is shown below

$$A \frac{d}{dx} \left(\kappa_0 \frac{300}{T} \frac{dT}{dx} \right) - g(T - T_0) = -I \left(\frac{-dF_n}{dx} \right) \quad (5.5)$$

where, $\kappa_0 = 3600 \text{ W/m/K}$ [81] is the room temperature thermal conductivity of CNT, $A = \pi d \cdot 0.34 \times 10^{-9} \text{ m}^2$ is the heat conduction cross-section [81], and g is the tube-substrate thermal coupling. dF_n/dx in Eq. (5.5) is the change in electron quasi-Fermi level per unit length. Values of τ , and g are estimated from the measured data for metallic tubes as discussed in the next section.

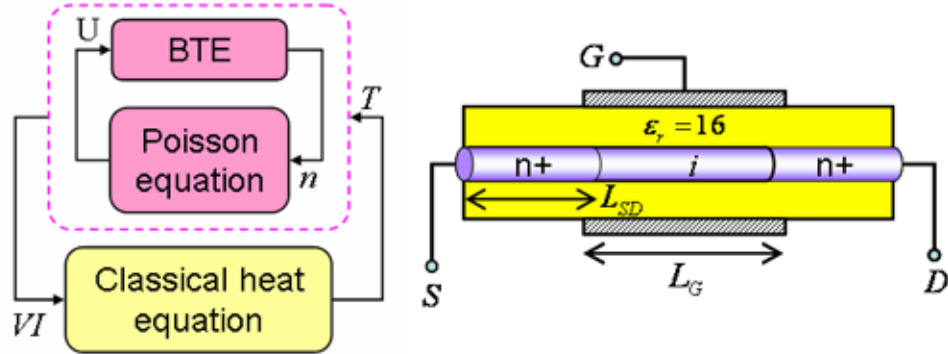


Fig. 5.3. (a) Flowchart of the simulation scheme. Electron and phonon BTE, and Poisson equation are solved until steady-state is reached. Steady-state power density, IdV/dx is then used to calculate new T from heat equation, and the whole procedure is repeated until steady-state is reached. (b) Device structure of an ideal CNT MOSFET. Doped source (S) and drain (D) of doping $10^9/m$ has been assumed which corresponds to ~ 1 dopants in every 100 carbon atoms. Channel length, L_G , and S/D extension lengths, L_{SD} are 20nm. Metal gate is used with workfunction 4.7eV and a 3nm thick HfO_2 gate dielectric ($\epsilon = 16$) is also assumed.

5.4 Comparison with experiment

For a long metallic tube, first term in Eq. (5.5) becomes negligible, and the temperature is given by,

$$(T - T_0) \approx \frac{VI}{Lg} \quad (5.6)$$

where, $T_0 = 300K$. At high bias, the current in a long metallic tube saturates around $20\mu A$ [46]. Using the saturation current in Eq. (5.6) and a burning temperature of $\sim 850K$ [81], we get $V_{BD} = (27.5)gL$, where, L is in microns. Figure 5.4a shows the burning voltage scales linearly with tube length ($L > 1\mu m$) and the slope of the straight line gives an estimate of g , which is found to be $0.18W/m/K$. Using $g = 0.18W/m/K$, and the scattering rates in metallic tubes, the electron BTE and heat equations are solved for a $300nm$ long metallic tube. This is the ‘equilibrium phonons simulation’, which gives much higher current compared to the measured data, as shown in Fig. 5.4b. When the phonon BTE is also solved to include the effect of non-equilibrium phonon population (hot phonon effect), a very good match between simulation and experiment is obtained. In this case, the phonon decay time, τ is used as a fitting parameter, and the best result is obtained for $\tau = 3ps$. Using $g = 0.18W/m/K$, and $\tau = 3ps$, the burning bias is next simulated. The solid line in Fig. 5.4a shows the simulated burning bias, which is in good agreement with experiment. Since, the difference between metallic and semiconducting tube is in their chirality, the value of g and τ obtained from metallic tubes should remain more or less the same for semiconducting tubes.

5.5 DC Characteristics of CNT MOSFETs

5.5.1 Hot phonon effect on Drain current

Although similar experimental data does not exist for semiconducting tubes, our calibrated model allows us to explore the effect of hot phonons on transistor performance. To examine how hot phonon effects influence the performance of a CNT

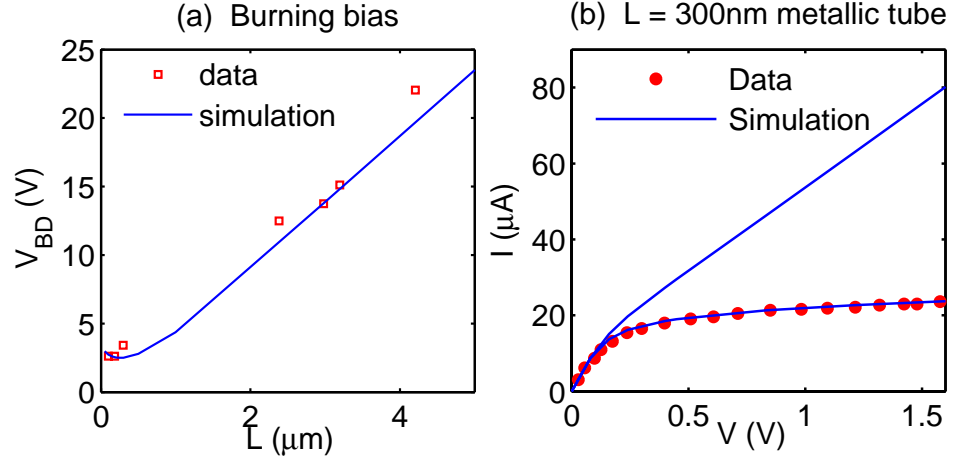


Fig. 5.4. (a) Bias needed to burn (V_{BD}) for metallic tube at different tube lengths. Symbols show experimental data from [81], and solid line is simulation assuming, $\tau = 3ps$, $g = 0.18W/m/K$. (b) I-V simulation for a 300nm long metallic tube. Symbols are measured data from [47], solid lines are simulation. Equilibrium phonon simulation is done assuming equilibrium phonon population at 300K, which results in unrealistically high current. For hot phonon simulation phonon decay time τ , is used as fitting parameter, and the best fit is obtained for $\tau = 3ps$ [78]

MOSFET, we begin with dc simulation. The effect of scattering (assuming equilibrium phonon population) on the drain current is examined first. Let us define the quantity, $\eta \equiv \mu_S - E_{C,top}$, where, μ_S is source Fermi level, and $E_{C,top}$ is the top of the channel barrier. At low V_{GS} , the potential barrier is high and η is small compared to optical phonon energy ($\sim 183\text{meV}$, K_{LO} branch, see Fig. 5.2); this leads to less optical phonon scattering, since most of the scattering events are blocked by the bandedge. As V_{GS} increases, the top of barrier is pushed down, (increasing η), and this allows more scattering events to take place within the channel. Note that scattering near the drain does not matter for DC current since, the carriers eventually get collected at drain because once scattered, they cannot surmount the big drain-channel barrier. Thus the ballisticity factor, defined as the ratio between current under scattering to the ballistic current, is expected to decrease with increasing gate bias (or *eta*), ballisticity is close to 100%, however, it gradually reduces to $\sim 75\%$ (assuming equilibrium phonon population) at $V_{GS} = 0.5V$. Figure 5.5a. At small value of η , ballisticity is close to 100%, however, it gradually reduces to $\sim 75\%$ (assuming equilibrium phonon population) at $V_{GS} = 0.5V$. Figure 5.5b shows the drain current with drain voltage under $V_{GS} = 0.5V$ condition ($\eta = 110\text{meV}$). The upper curve is for the ballistic current, the middle one is for current with scattering assuming equilibrium phonon, and the lowest one is with hot-phonon effect turned on. Phonon scattering reduces the current by 23%, while hot-phonon effect reduces the current by 33% from the ballistic limit.

5.5.2 Self heating and hot spot

Next we include the self heating effect in the simulation, however, we find no appreciable difference in drain-current. This is because, current in a single tube is smaller than the corresponding metallic tube current, and the applied bias is also smaller (metallic tube bias is usually $> 1V$), thus power density is not as high as is observed in metallic tubes. The temperature profile along the tube is shown in Fig.

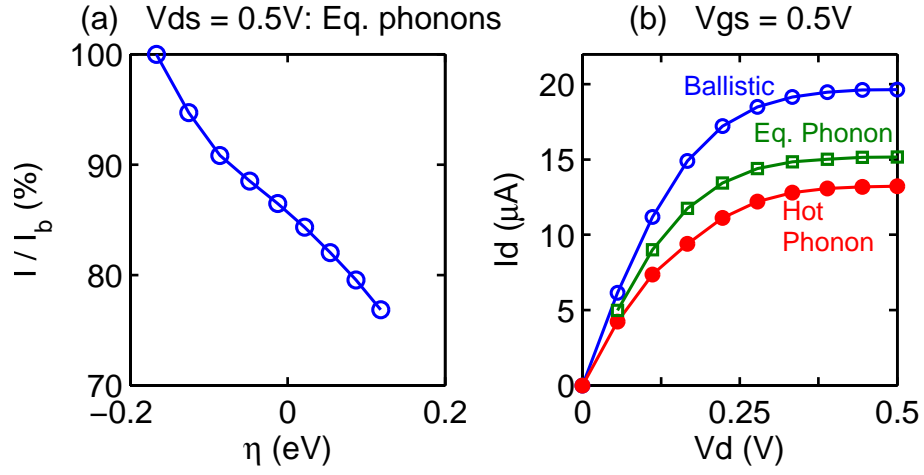


Fig. 5.5. (a) Ballisticity with η . Ballisticity gradually reduces with increasesing value of η and at $V_{GS} = 0.5$ V for which $\eta = 110$ meV ballisticity = 77%. (b) shows the output characteristics with scattering. The upper curve is ballistic, the middle one is with scattering assuming equilibrium phonons, and the lower one is with hot-phonons. At $V_{ds}=0.5$ V, ballisticity becomes 77% with equilibrium phonons, and 67% with hot-phonons.

5.6, and only an increase of 25K temperature is seen at on state ($V_{GS} = 0.5V$, $V_{DS} = 0.5V$). Figure 5.6 also shows the hot spot occurs near the channel-drain junction, consistent with the profile of the quasi-Fermi levels (see inset of Fig. 5.6).

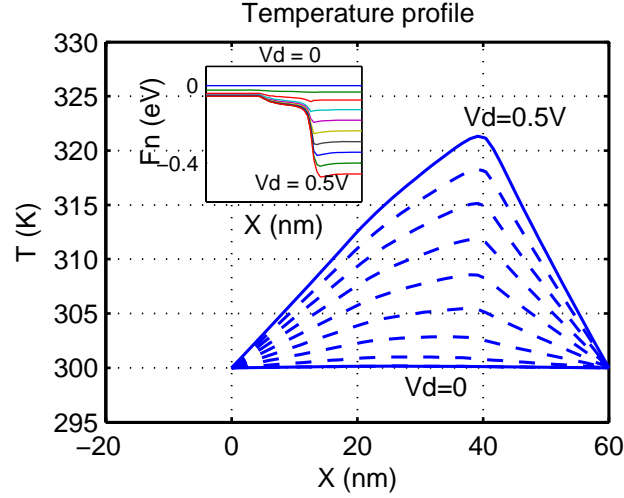


Fig. 5.6. Temperature profile along the tube. Gate voltage is fixed at $V_{gs}=0.5V$, and drain voltage is varied from 0-0.5V, with a step of 0.055V. Peak temperature occurs near drain channel junction where maximum voltage drop occurs. Inset shows the variation of quasi-fermi level, note that maximum voltage drop occurs near the drain-channel junction.

5.6 AC Characteristics

Finally, to establish the cut-off frequency of CNT MOSFETs, the large signal dynamic characteristics are examined. A 100mV high step signal is applied at gate under the on condition ($V_{GS} = 0.5V$, $V_{DS} = 0.5V$), and the corresponding drain current variation with time is simulated for the ballistic, equilibrium-phonon, and hot phonon cases, (see Fig. 5.7). A Fourier transform of the drain current is next performed to calculate the frequency specific transconductance as shown in Fig. 5.8. The numerical technique of calculating this Fourier transform is discussed in Hockney et al. [87]. At unity gain cut-off, the transconductance equals to the input admit-

tance, $\omega C_{ox} L_G$ (see Fig. 5.8 for values). Cut-off frequency, f_T , obtained for ballistic, equilibrium-phonon and hot-phonon cases are estimated as 1.26THz, 0.75THz, and 0.55THz, respectively. Note that the reduction in f_T due to equilibrium and hot phonon scattering is more than the reduction in their drain currents. For example, the ballistic current reduces by 23% and 33% for equilibrium phonon and hot phonon cases, where as reduction in f_T are 40% and 56% respectively. Since the quasi static $f_T = g_m/2\pi C_g$, and f_T reduces more than g_m ; this implies that the capacitance also increases with scattering. As the gate voltage changes, electrons try to follow the change, but due to multiple phonon scattering it takes electrons longer to respond to the gate signal; quasistatically which is equivalent to a larger gate capacitance. Since we are solving BTE for electrons, all the dynamic effects along with the effect of kinetic inductance are already included in these simulations.

5.7 Summary

The effect of phonon scattering and heating of CNT MOSFET is studied in this chapter. For single tubes, heating does not seem to be a problem, due to comparatively low operating bias of voltage and low current than metallic tubes. At high gate bias, hot-phonon effect can reduce the ballistic current by 33%, and the unit gain cut-off frequency by 56%. The unit gain cut-off frequency for a 20nm gate length co-axially gated device of Fig. 5.3b, is found to be 0.55THz.

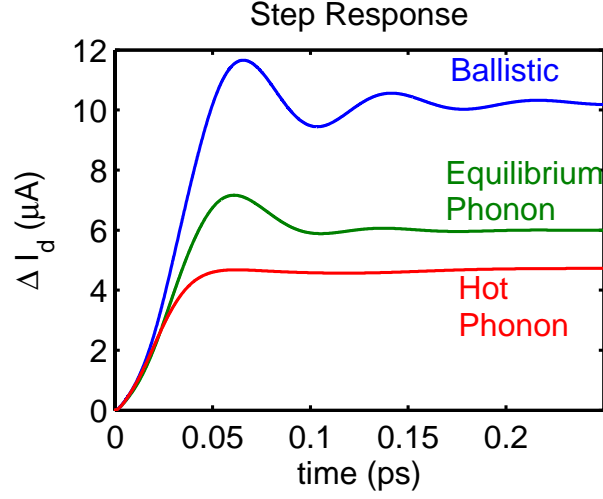


Fig. 5.7. Step response corresponding to a 100mV gate pulse under $V_{GS} = 0.5V$, $V_{DS} = 0.5V$ condition. Ballistic, equilibrium phonon, and hot phonon cases are considered separately.

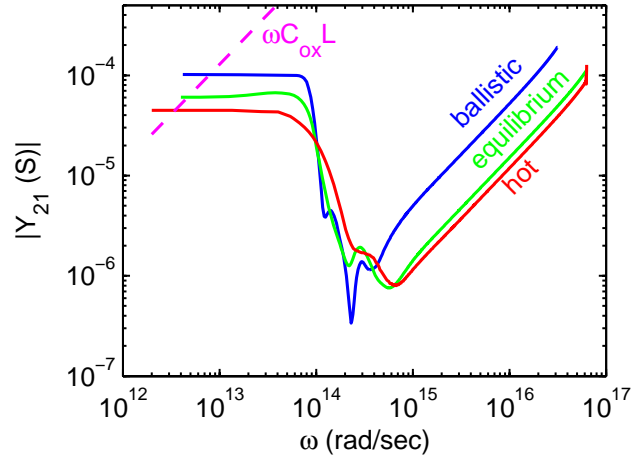


Fig. 5.8. Step response of the transconductance. Step calculated using the method of Hockney et al. [87]. The top curve is under ballistic transport, the middle one is with equilibrium phonon scattering and the bottom one is with hot-phonon scattering. The dashed line shows the idealized input admittance with frequency.

6. CONCLUSION AND FUTURE WORK

6.1 Summary

In this work the following has been done:

First a method of calculating the phonon modes has been developed incorporating the symmetry of the armchair and zigzag tubes. This method enables the calculation of phonon modes and their eigenvectors. According to the momentum conservation rule in electron-phonon scattering, only a few phonon subbands are of importance that contribute to the electron phonon scattering. Using this method, the dispersion and eigenvectors of the phonon branches of interest can be obtained directly. These eigenvectors are then used in Mahan's [49] approach to obtain the electron-phonon scattering matrix element over the entire Brillouine zone (BZ).

Next a full-band electron and phonon Boltzmann transport equation (BTE) solver has been developed for simulating the coupled electron-phonon transport. The coupled BTE solvers are then combined with the heat equation in a self-consistent manner that enables the assessment of heating in the device. Simulation of electron and phonon transport has been done without any approximation in their respective band-structure. Thus, for electrons no effective mass approximation has been done as is common in the previous works [53–56], and for the phonons, both the approximated linear acoustic branch and the approximated dispersionless optical phonon branches have been replaced by their actual phonon branches obtained by the phonon mode calculation. Since the BTEs are solved in time, the method can be used to study the AC behavior of CNT-MOSFET and interconnect in detail.

The method were first applied to the study of metallic tubes. It has been shown that, the electron phonon scattering quickly drives the optical phonons into non-equilibrium, and the added phonons contribute to the current saturation in the long

metallic tubes observed experimentally. For the suspended tubes, the self-heating, builds up due to the lack of tube-substrate thermal coupling, contributes to the negative differential resistance effect. The role of hot-phonon and self-heating effects in suspended tubes also has been clarified in chapter 4. The results showed that the measured data for tubes on a substrate and suspended above a substrate can be well described by theoretically calculated EPC and a phenomenological phonon decay time, which is in agreement experimental estimation.

After showing that the method can explain the metallic tube data for various experimental setup, it has been applied to the study of CNT-MOSFETs. The purpose is to study the effect of hot-phonon and self-heating in CNT-MOSFETs. For CNT-MOSFETs, since the tube is always in a close contact with the substrate the heating is not significant. Hot-phonons, however, have a significant effect. At 0.5V gate bias ($\eta \sim 1.25eV$), the ballisticity reduces to 60% due to hot-phonon effect and the unity gain cut-off frequency reduces from 1.26THz (for a 20nm gate length device) for the ballistic condition to 0.55THz with hot-phonon effect.

6.2 Future work

The following are the suggested future work:

The electron phonon coupling (EPC) plays an important role in determining the electronic transport as well as in the electroluminescence experiments. To study the diameter dependent experimental data, all chiralities belonging to same diameter need to be considered. The phonon mode and the EPC calculation method presented in this work only incorporates armchair and zigzag tubes. The method can be extended to incorporate arbitrary chirality. This is important in explaining the electroluminescence properties, which shows strong chirality dependence.

In the study of metallic tubes, the effect of non-linear bandstructure on very small and very long metallic tubes could be examined. The full band calculation provided in this work could serve as a benchmark for the commonly used linear band

approximations for the metallic tubes. A more ambitious extension could be the use of a microscopic scattering model for phonon transport. This should enable one to predict the anharmonic lifetime, which has been used as a fitting parameter in this work. If microscopic scattering model is used, the thermal conductivity ($\kappa = 2800 \text{ W/m/K}$ is assumed in this work) of carbon nanotubes can be predicted, which is of interest, since the extraction of thermal conductivity of nanotubes is difficult.

Finally in the study of semiconducting tubes, the full power of the time-dependent transport model has not been harnessed. Using a full-dynamic transport simulation with varying tube lengths, the effect of kinetic inductance could be observed, and the limits of the validity of the quasi-static approximation can be determined. The effect of kinetic inductance should become increasingly important as the tube length is increased.

LIST OF REFERENCES

LIST OF REFERENCES

- [1] G. E. Moore, "Progress in digital integrated electronics," *IEDM, Tech. Dig. - IEEE*, pp. 11–13, 1975.
- [2] D. Frank, R. Dennard, E. Nowak, P. Solomon, Y. Taur, and H.-S. P. Wong, "Device scaling limits of si mosfets and their application dependencies," *Proceedings of the IEEE*, vol. 89, no. 3, pp. 259 – 88, 2001.
- [3] Y. Taur, "Cmos design near the limit of scaling," *IBM Journal of Research and Development*, vol. 46, no. 2-3, pp. 213 – 22, 2002.
- [4] "International technology roadmap for semiconductors, semiconductor industry association, ca, <http://www.itrs.net/>," 2006.
- [5] R. H. Baughman, A. A. Zakhidov, and W. A. de Heer, "Carbon nanotubes - the route toward applications," *Science*, vol. 297, pp. 787–792, 2002.
- [6] P. Avouris, J. Appenzeller, V. Derycke, R. Martel, and S. Wind, "Carbon nanotube electronics," *International Electron Devices Meeting. Technical Digest (Cat. No.02CH37358)*, pp. 281 – 4, 2002.
- [7] P. Avouris, J. Appenzeller, R. Martel, and S. Wind, "Carbon nanotube electronics," *Proceedings of the IEEE*, vol. 91, no. 11, pp. 1772 – 84, 2003.
- [8] H. Dai, "Pushing to the performance limit of carbon nanotube electronics," *61st Device Research Conference. Conference Digest (Cat. No.03TH8663)*, pp. 165 –, 2003.
- [9] S. Heinze, J. Tersoff, and P. Avouris, "Carbon nanotube electronics and optoelectronics," pp. 381 – 409, 2005.
- [10] A. Javey and H. Dai, "Carbon nanotube electronics," *Proceedings. 19th International Conference on VLSI Design held jointly with 5th International Conference on Embedded Systems and Design*, pp. 6 pp. –, 2006.
- [11] T. Durkop, S. Getty, E. Cobas, and M. Fuhrer, "Extraordinary mobility in semiconducting carbon nanotubes," *Nano Letters*, vol. 4, no. 1, pp. 35–39, 2004.
- [12] S. J. Tans, A. R. M. Verschueren, and C. Dekker, "Room-temperature transistor based on a single carbon nanotube," *Nature*, vol. 393, no. 6680, pp. 49–52, 1998.
- [13] R. Martel, T. Schmidt, H. R. Shea, T. Hertel, and P. Avouris, "Single- and multi-wall carbon nanotube field-effect transistors," *Applied Physics Letters*, vol. 73, no. 17, pp. 2447–2449, 1998.

- [14] R. Martel, V. Derycke, J. Appenzeller, S. Wind, and P. Avouris, "Carbon nanotube field-effect transistors and logic circuits," *Proceedings 2002 Design Automation Conference (IEEE Cat. No.02CH37324)*, pp. 94 – 8, 2002.
- [15] M. Freitag and A. Johnson, "Nanoscale characterization of carbon nanotube field-effect transistors," *AIP Conference Proceedings*, no. 633, pp. 513 – 16, 2002.
- [16] J. Appenzeller, J. Knoch, V. Derycke, R. Martel, S. Wind, and P. Avouris, "Field-modulated carrier transport in carbon nanotube transistors," *Physical Review Letters*, vol. 89, no. 12, pp. 126801 – 1, 16 Sept. 2002.
- [17] J. Appenzeller, J. Knoch, R. Martel, V. Derycke, S. Wind, and P. Avouris, "Short-channel like effects in schottky barrier carbon nanotube field-effect transistors," *International Electron Devices Meeting. Technical Digest (Cat. No.02CH37358)*, pp. 285 – 8, 2002.
- [18] S. Heinze, J. Tersoff, R. Martel, V. Derycke, J. Appenzeller, and P. Avouris, "Carbon nanotubes as schottky barrier transistors," *Physical Review Letters*, vol. 89, no. 10, pp. 106801 – 1, 2 Sept. 2002.
- [19] S. Heinze, M. Radosavljevic, J. Tersoff, and P. Avouris, "Unexpected scaling of the performance of carbon nanotube schottky-barrier transistors," *Physical Review B (Condensed Matter and Materials Physics)*, vol. 68, no. 23, pp. 235418 – 1, 2003.
- [20] J. Appenzeller, J. Knoch, M. Radosavljevic, and P. Avouris, "Multimode transport in schottky-barrier carbon-nanotube field-effect transistors," *Physical Review Letters*, vol. 92, no. 22, pp. 226802 – 1, 2004.
- [21] A. Javey, Q. Wang, W. Kim, and H. Dai, "Advancements in complementary carbon nanotube field-effect transistors," *IEEE International Electron Devices Meeting 2003*, pp. 31 – 2, 2003.
- [22] M. Pourfath, E. Ungersboeck, A. Gehring, B. Cheong, W. Park, H. Kosina, and S. Selberherr, "Improving the ambipolar behavior of schottky barrier carbon nanotube field effect transistors," *Proceedings of the 34th European Solid-State Device Research Conference*, pp. 429 – 32, 2004.
- [23] B. Kim, T. Brintlinger, E. Cobas, M. Fuhrer, H. Zheng, Z. Yu, R. Droopad, J. Ramdani, and K. Eisenbeiser, "High-performance carbon nanotube transistors on $\text{Si}_3\text{N}_4/\text{Si}$ substrates," *Applied Physics Letters*, vol. 84, no. 11, pp. 1946 – 8, 2004.
- [24] S. Auvray, J. Borghetti, M. Goffman, A. Filoramo, V. Derycke, J. Bourgoin, and O. Jost, "Carbon nanotube transistor optimization by chemical control of the nanotube-metal interface," *Applied Physics Letters*, vol. 84, no. 25, pp. 5106 – 8, 2004.
- [25] A. Javey, J. Guo, D. Farmer, Q. Wang, E. Yenilmez, R. Gordon, M. Lundstrom, and H. Dai, "Self-aligned ballistic molecular transistors and electrically parallel nanotube arrays," *Nano Letters*, vol. 4, no. 7, pp. 1319–1322, 2004.
- [26] M. Pourfath, E. Ungersboeck, A. Gehring, B. Cheong, W. Park, H. Kosina, and S. Selberherr, "Optimization of schottky barrier carbon nanotube field effect transistors," *Microelectronic Engineering*, vol. 81, no. 2-4, pp. 428 – 33, 2005.

- [27] Y.-M. Lin, J. Appenzeller, J. Knoch, and P. Avouris, "High-performance carbon nanotube field-effect transistor with tunable polarities," *IEEE Transactions on Nanotechnology*, vol. 4, no. 5, pp. 481 – 9, Sept. 2005.
- [28] J. Guo, S. Datta, and M. Lundstrom, "A numerical study of scaling issues for schottky-barrier carbon nanotube transistors," *Electron Devices, IEEE Transactions on*, vol. 51, no. 2, pp. 172–177, 2004.
- [29] J. Appenzeller, "Ac and dc characteristics of carbon nanotube field-effect transistors," *Proceedings of the 2004 Bipolar/BiCMOS Circuits and Technology Meeting (IEEE Cat. No.04CH37593)*, pp. 192 – 3, 2004.
- [30] D. John and D. Pulfrey, "Switching-speed calculations for schottky-barrier carbon nanotube field-effect transistors," *J. Vac. Sci. Technol. A, Vac. Surf. Films (USA)*, vol. 24, no. 3, pp. 708 – 12, 2006.
- [31] P. Burke, "Luttinger liquid theory as a model of the gigahertz electrical properties of carbon nanotubes," *IEEE Transactions on Nanotechnology*, vol. 1, no. 3, pp. 129 – 44, Sept. 2002.
- [32] P. Burke, "An rf circuit model for carbon nanotubes," *IEEE Trans. Nanotechnol. (USA)*, vol. 2, no. 1, pp. 55 – 8, 2003.
- [33] P. Burke, "Ac performance of nanoelectronics: towards a ballistic thz nanotube transistor," *Solid-State Electronics*, vol. 48, no. 10-11, pp. 1981 – 6, 2004.
- [34] Z. Yu and P. Burke, "Microwave transport in metallic single-walled carbon nanotubes," *Nano Letters*, vol. 5, no. 7, pp. 1403 – 6, 2005.
- [35] Z. Yu and P. Burke, "Aligned array fets as a route toward thz nanotube transistors," *Proc. SPIE - Int. Soc. Opt. Eng. (USA)*, vol. 5790, no. 1, pp. 246 – 53, 2005.
- [36] S. Salahuddin, M. Lundstrom, and S. Datta, "Transport effects on signal propagation in quantum wires," *IEEE Trans. Electron Devices (USA)*, vol. 52, no. 8, pp. 1734 – 42, 2005.
- [37] J. Guo, S. Hasan, A. Javey, G. Bosman, and M. Lundstrom, "Assessment of high-frequency performance potential of carbon nanotube transistors," *IEEE Trans. Nanotechnol. (USA)*, vol. 4, no. 6, pp. 715 – 21, 2005.
- [38] S. Hasan, S. Salahuddin, M. Vaidyanathan, and M. Alam, "High-frequency performance projections for ballistic carbon-nanotube transistors," *IEEE Trans. Nanotechnol. (USA)*, vol. 5, no. 1, pp. 14 – 22, 2006.
- [39] C. Kane, E. Mele, R. Lee, J. Fischer, P. Petit, H. Dai, A. Thess, R. Smalley, A. Verschuere, S. Tans, and C. Dekker, "Temperature-dependent resistivity of single-wall carbon nanotubes," *Euro Physics Letter*, vol. 41, no. 6, p. 683, 1998.
- [40] R. A. Jishi, M. S. Dresselhaus, and G. Dresselhaus, "Electron-phonon coupling and the electrical conductivity of fullerene nanotubules," *Phys. Rev. B*, vol. 48, pp. 11385–11389, Oct 1993.
- [41] L. M. Woods and G. D. Mahan, "Electron-phonon effects in graphene and arm-chair (10,10) single-wall carbon nanotubes," *Phys. Rev. B*, vol. 61, pp. 10651–10663, Apr 2000.

- [42] T. Hertel and G. Moos, “Electron-phonon interaction in single-wall carbon nanotubes: a time-domain study,” *Phys. Rev. Lett.*, vol. 84, no. 21, p. 5002, 2000.
- [43] A. Bachtold, M. S. Fuhrer, S. Plyasunov, M. Forero, E. H. Anderson, A. Zettl, and P. L. McEuen, “Scanned probe microscopy of electronic transport in carbon nanotubes,” *Phys. Rev. Lett.*, vol. 84, pp. 6082–6085, Jun 2000.
- [44] J. Appenzeller, R. Martel, P. Avouris, H. Stahl, and B. Lengeler, “Optimized contact configuration for the study of transport phenomena in ropes of single-wall carbon nanotubes,” *Applied Physics Letters*, vol. 78, no. 21, pp. 3313–3315, 2001.
- [45] H. Suzuura and T. Ando, “Phonons and electron-phonon scattering in carbon nanotubes,” *Physical Review B (Condensed Matter and Materials Physics)*, vol. 65, no. 23, pp. 235412–1, 2002.
- [46] Z. Yao, C. L. Kane, and C. Dekker, “High-field electrical transport in single-wall carbon nanotubes,” *Phys. Rev. Lett.*, vol. 84, no. 13, p. 2941, 2000.
- [47] A. Javey, J. Guo, M. Paulsson, Q. Wang, D. Mann, M. Lundstrom, and H. Dai, “High-field quasiballistic transport in short carbon nanotubes,” *Phys. Rev. Lett.*, vol. 92, no. 10, p. 106804, 2004.
- [48] J. Y. Park, S. Rosenblatt, Y. Yaish, V. Sazonova, H. Ustunel, S. Braig, T. A. Arias, P. W. Brouwer, and P. L. McEuen, “Electron-phonon scattering in metallic single-walled carbon nanotubes,” *Nano Lett.*, vol. 4, no. 3, p. 517, 2004.
- [49] G. Mahan, “Electron-optical phonon interaction in carbon nanotubes,” *Phys. Rev. B (Condensed Matter and Materials Physics)*, vol. 68, no. 12, p. 125409, 2003.
- [50] M. Lazzeri, S. Piscanec, F. Mauri, A. C. Ferrari, and J. Robertson, “Electron transport and hot phonons in carbon nanotubes,” *Phys. Rev. Lett.*, vol. 95, no. 23, p. 236802, 2005.
- [51] G. Pennington and N. Goldsman, “Monte carlo study of electron transport in a carbon nanotube,” *IEICE Transactions on Electronics*, vol. E86-C, no. 3, p. 372, 2003.
- [52] G. Pennington and N. Goldsman, “Semiclassical transport and phonon scattering of electrons in semiconducting carbon nanotubes,” *Physical Review B*, vol. 68, no. 4, 2003.
- [53] G. Pennington and N. Goldsman, “Low-field semiclassical carrier transport in semiconducting carbon nanotubes,” *Physical Review B*, vol. 71, no. 20, 2005.
- [54] V. Perebeinos, J. Tersoff, and P. Avouris, “Electron-phonon interaction and transport in semiconducting carbon nanotubes,” *Phys. Rev. Lett.*, vol. 94, p. 086802, Mar 2005.
- [55] A. Verma, M. Z. Kauser, and P. P. Ruden, “Effects of radial breathing mode phonons on charge transport in semiconducting zigzag carbon nanotubes,” *Applied Physics Letters*, vol. 87, no. 12, p. 123101, 2005.

- [56] A. Verma, M. Z. Kauser, and P. P. Ruden, "Ensemble monte carlo transport simulations for semiconducting carbon nanotubes," *Journal of Applied Physics*, vol. 97, no. 11, p. 114319, 2005.
- [57] S. Hasan, J. Guo, M. Vaidyanathan, M. A. Alam, and M. Lundstrom, "Monte carlo simulation of carbon nanotube devices," *Journal Journal of Computational Electronics*, vol. 3, no. 3-4, pp. 333–336, 2004.
- [58] J. Guo and M. Lundstrom, "Role of phonon scattering in carbon nanotube field-effect transistors," *Applied Physics Letters*, vol. 86, no. 19, p. 193103, 2005.
- [59] S. Koswatta, S. Hasan, M. Lundstrom, M. Anantram, and D. Nikonov, "Ballistic of nanotube field-effect transistors: role of phonon energy and gate bias," *Applied Physics Letters*, vol. 89, no. 2, pp. 23125 – 1, 2006.
- [60] A. Javey, J. Guo, Q. Wang, M. Lundstrom, and H. Dai, "Ballistic carbon nanotube field-effect transistors," *Nature (UK)*, vol. 424, no. 6949, pp. 654 – 7, 2003.
- [61] M. Lundstrom, *Fundamentals of carrier transport. Second edition*. Cambridge University Press, 2000.
- [62] R. Jishi, L. Venkataraman, M. Dresselhaus, and G. Dresselhaus, "Phonon modes in carbon nanotubules," *Chemical Physics Letters*, vol. 209, no. 1-2, p. 77, 1993.
- [63] A. M. Rao, E. Richter, S. Bandow, B. Chase, P. C. Eklund, K. A. Williams, S. Fang, K. R. Subbaswamy, M. Menon, A. Thess, R. E. Smalley, G. Dresselhaus, and M. S. Dresselhaus, "Diameter-Selective Raman Scattering from Vibrational Modes in Carbon Nanotubes," *Science*, vol. 275, no. 5297, p. 187, 1997.
- [64] S. V. Goupalov, "Continuum model for long-wavelength phonons in two-dimensional graphite and carbon nanotubes," *Physical Review B*, vol. 71, no. 8, 2005.
- [65] R. Saito, *Physical Properties of Carbon Nanotubes*. World Scientific Publishing Company, 1998.
- [66] J. M. Ziman, *Electrons and Phonons : The Theory of Transport Phenomena in Solids*. Oxford University Press, USA, Reprint edition (April 5, 2001).
- [67] Y. N. Gartstein, "Vibrations of single-wall carbon nanotubes: lattice models and low-frequency dispersion," *Physics Letters A*, vol. 327, no. 1, p. 83, 2004.
- [68] L. Pietronero, S. Strässler, H. R. Zeller, and M. J. Rice, "Electrical conductivity of a graphite layer," *Phys. Rev. B*, vol. 22, no. 2, p. 904, 1980.
- [69] This value is obtained by fitting the tight-binding bandgap with the bandgap obtained from non-orthogonal Huckel treatment. The detail of the Huckel treatment can be found in D. Kienle et al., "Extended Huckel theory for band structure, chemistry, and transport. I. Carbon nanotubes" *Jour. of Applied Phys.*, vol. 100, number 4, pages 043714.
- [70] R. Al-Jishi and G. Dresselhaus, *Lattice-dynamical model for graphite*, vol. 26. American Physical Society, 1982.

- [71] S. Hasan, J. Guo, M. Vaidyanathan, M. Alam, and M. Lundstrom, "Monte-carlo simulation of carbon nanotube devices," in *2004 10th International Workshop on Computational Electronics, 24-27 Oct. 2004*, 2004 10th International Workshop on Computational Electronics (IEEE Cat. No.04EX915), (West Lafayette, IN, USA), pp. 190–1 BN – 0 7803 8649 3, IEEE, 2004.
- [72] K. Banoo, *Direct Solution of Boltzmann Transport Equation in Nanoscale Devices*. PhD thesis, Purdue University, West Lafayette, IN, 2000.
- [73] J. P. Kreskovsky, "A hybrid central difference scheme for solid-state device simulation," *IEEE Trans. Elec. Dev.*, vol. ED-34, no. 5, p. 1128, 1987.
- [74] B. Ridley, *Quantum processes in semiconductors, Fourth edition*. Oxford University Press, USA, 2000.
- [75] J. J. Sakurai, *Electrons and Phonons : The Theory of Transport Phenomena in Solids*. Addison Wesley, 1992.
- [76] G. B. Arfken and H. J. Weber, *Mathematical Methods For Physicists, Sixth edition*. Academic Press, 2005.
- [77] T. Kampfrath, L. Perfetti, F. Schapper, C. Frischkorn, and M. Wolf, "Strongly coupled optical phonons in the ultrafast dynamics of the electronic energy and current relaxation in graphite," *Phys. Rev. Lett.*, vol. 95, no. 18, p. 187403, 2005.
- [78] G. Lang, K. Karch, M. Schmitt, P. Pavone, A. P. Mayer, R. K. Wehner, and D. Strauch, "Anharmonic line shift and linewidth of the raman mode in covalent semiconductors," *Phys. Rev. B*, vol. 59, no. 9, p. 6182, 1999.
- [79] E. Pop, D. Mann, Q. Wang, K. Goodson, and H. Dai, "Thermal conductance of an individual single-wall carbon nanotube above room temperature," *Nano Lett.*, vol. 6, no. 1, p. 96, 2006.
- [80] E. Pop, D. Mann, J. Cao, Q. Wang, K. Goodson, and H. J. Dai, "Negative differential conductance and hot phonons in suspended nanotube molecular wires," *Phys. Rev. Lett.*, vol. 95, no. 15, p. 155505, 2005.
- [81] E. Pop, D. Mann, J. Reifenberg, K. Goodson, and H. J. Dai, "Electro-thermal transport in metallic single-wall carbon nanotubes for interconnect applications," *IEDM, Tech. Dig. - IEEE*, p. 11.2, 2005.
- [82] J. Jiang, R. Saito, G. G. Samsonidze, S. G. Chou, A. Jorio, G. Dresselhaus, and M. S. Dresselhaus, "Electron-phonon matrix elements in single-wall carbon nanotubes," *Phys. Rev. B*, vol. 72, no. 23, p. 235408, 2005.
- [83] M. Lazzeri and F. Mauri, "Coupled dynamics of electrons and phonons in metallic nanotubes: Current saturation from hot-phonon generation," *Phys. Rev. B*, vol. 73, no. 16, p. 165419, 2006.
- [84] M. A. Kuroda and J.-P. Leburton, "Joule heating induced negative differential resistance in freestanding metallic carbon nanotubes," *Applied Physics Letters*, vol. 89, no. 10, p. 103102, 2006.
- [85] A. Debernardi, S. Baroni, and E. Molinari, "Anharmonic phonon lifetimes in semiconductors from density-functional perturbation theory," *Phys. Rev. Lett.*, vol. 75, no. 9, p. 1819, 1995.

- [86] D. Mann, E. Pop, J. Cao, Q. Wang, K. Goodson, and H. Dai, “Thermally and molecularly stimulated relaxation of hot phonons in suspended carbon nanotubes,” *J. Phys. Chem. B*, vol. 110, no. 4, p. 1502, 2006.
- [87] R. W. Hockney and J. W. Eastwood, *Computer Simulation using Particles. New Ed edition*. Taylor and Francis, 1998.
- [88] G. Mahan and G. S. Jeon, “Flexure modes in carbon nanotubes,” *Physical Review B*, vol. 70, no. 7, p. 75405, 2004.

APPENDIX

A. CALCULATION OF DYNAMICAL MATRIX

The symmetry based phonon mode calculation method for armchair and zigzag tube is illustrated in this appendix.

A.1 Bond Triplets

A.1.1 Armchair tube

Ring 1

Each A and B atoms can be considered as connected (for the purpose of this treatment, we call them ‘bond’) with it’s 18 neighbors, which are on 4 nearest neighboring (NN) rings. Associated with each bond there are three unit vectors (‘bond triplet’) these are – i) along the direction of the bond, $\hat{\ell}$, ii) along the in-plane transverse direction, $\hat{\mathbf{t}}$, and iii) along the out of plane transverse direction, $\hat{\mathbf{o}}$. Below all the unit vectors are listed for the neighbors of A. To calculate the dynamical matrix, bond triplet associated with the neighbors of B atoms are not necessary. The first step in calculating these bond triplets is to identify the coordinates of the neighboring atoms on 2-d graphene plane and the azimuthal angle they make with the $\hat{\mathbf{x}}$ axis. Considering Fig. A.1 we see that there are three B atoms on the first NN ring with the following coordinates

$$\begin{aligned}\mathbf{r}_1 &= a\hat{\mathbf{y}} \\ \mathbf{r}_2 &= -a/2\hat{\mathbf{y}} + \sqrt{3}a/2\hat{\mathbf{z}} \\ \mathbf{r}_3 &= -a/2\hat{\mathbf{y}} - \sqrt{3}a/2\hat{\mathbf{z}}.\end{aligned}$$

Each a translation along $\hat{\mathbf{y}}$ creates an azimuthal angle of $\theta_a = 2\pi/3n$, at the center. Thus the azimuthal angles corresponding the above three vectors are: $\theta_a, -\theta_a/2, \theta_a/2$

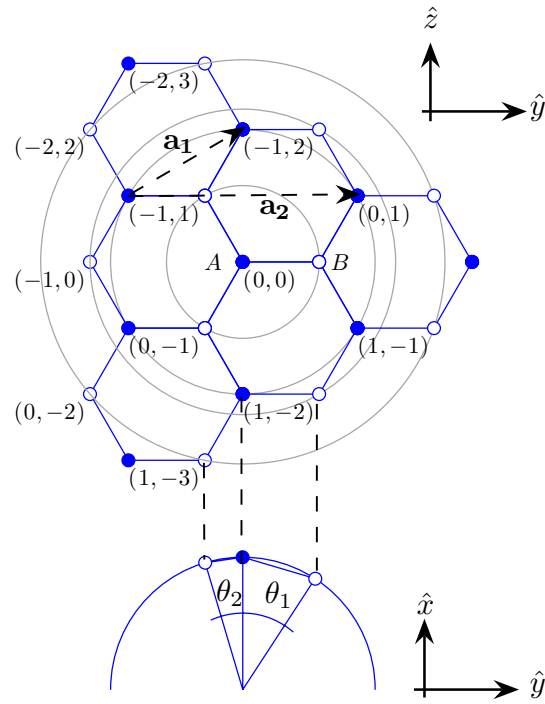


Fig. A.1. Upper panel shows an unrolled (n, n) armchair tube in the (y, z) plane. Lower panel shows the rolled tube in the (x, y) plane. Here $\theta_1 = 2\theta_2 = 2\pi/3n$, $\mathbf{a}_1 = \sqrt{3}a (\cos \frac{\pi}{6} \hat{y} + \sin \frac{\pi}{6} \hat{z})$, $\mathbf{a}_2 = 3a \hat{y}$, and $a = 1.42 \times 10^{-10} m$.

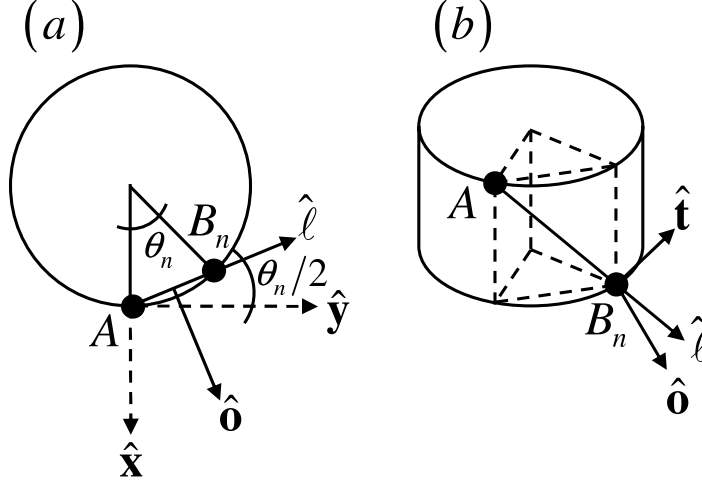


Fig. A.2. (a) If atom B_n creates θ_n angle with the x axis, then the associate bond creates, $\pi/2 + \theta_n/2$ angle with the x axis. Thus the x and y components of the bond are proportional to, $-\sin \theta_n/2$ and $\text{sign}(\theta_n) \cos \theta_n/2$. The $\hat{\mathbf{O}}$ direction makes an angle of $\theta_n/2$ thus its components are: $(\cos \theta_n/2, \sin \theta_n/2, 0)$. (b) Shows the bond from a different angle.

respectively. Using this angles, the out of plane transverse directions can be written as

$$\mathbf{O}_1 = o_{ni} = \begin{bmatrix} \cos \theta_a/2 & \sin \theta_a/2 & 0 \\ \cos \theta_a/4 & -\sin \theta_a/4 & 0 \\ \cos \theta_a/4 & -\sin \theta_a/4 & 0 \end{bmatrix}. \quad (\text{A.1})$$

Using Fig. A.2, the 2-d position vectors and the above azimuthal angles the unit vectors along the bonding directions can be written as

$$\mathbf{L}_1 = \ell_{ni} = \begin{bmatrix} -\sin \theta_a/2 & \cos \theta_a/2 & 0 \\ -1/2 \sin \theta_a/4 & -1/2 \cos \theta_a/4 & \sqrt{3}/2 \\ -1/2 \sin \theta_a/4 & -1/2 \cos \theta_a/4 & -\sqrt{3}/2 \end{bmatrix}. \quad (\text{A.2})$$

Formally the above can be obtained from

$$\hat{\ell} = \frac{(\mathbf{R}_n - \mathbf{R}_0)}{|\mathbf{R}_n - \mathbf{R}_0|},$$

where, $\mathbf{R}_0 = (0, 0, 0)$ is the 3D cartesian coordinate of the A atom at origin, and \mathbf{R}_n is the 3D cartesian coordinate of the neighboring atom on nanotube surface. If the atom

under consideration has 2D graphene coordinate of $\mathbf{r}_n = y_n \hat{\mathbf{y}} + z_n \hat{\mathbf{z}}$, then the angle that it makes at the center is, $\theta_n = 2\pi a/3ny_n$ for an (n, n) armchair tube. Defining $R = 3na/2\pi$ as tube radius, the 3D coordinates become $\mathbf{R}_n = (R \cos \theta_n, R \sin \theta_n, z_n)$. Finally using, Eqs. (A.1),(A.2) we calculate the in-plane transverse directions using the relationship $\hat{\mathbf{t}} = \hat{\mathbf{o}} \times \hat{\ell}$:

$$\mathbf{T}_1 = t_{ni} = \begin{bmatrix} 0 & 0 & 1 \\ -\sqrt{3}/2 \sin \theta_a/4 & -\sqrt{3}/2 \cos \theta_a/4 & -1/2 \\ \sqrt{3}/2 \sin \theta_a/4 & \sqrt{3}/2 \cos \theta_a/4 & -1/2 \end{bmatrix}. \quad (\text{A.3})$$

The azimuthal angles of the neighbors are:

$$\theta_{1n} = (\theta_a, -\theta_a/2, -\theta_a/2), \quad (\text{A.4})$$

and their relative phase with respect to the A atom are:

$$\beta_{1n} = (\beta\theta_a, qc - \beta\theta_a/2, -qc - \beta\theta_a/2), \quad (\text{A.5})$$

where, q, β are phonon q wavevector and it's azimuthal quantum numbers.

Ring 2

Bond triplet:

$$\mathbf{L}_2 = \begin{bmatrix} -\sqrt{3}/2 \sin(3\theta_a/4) & \sqrt{3}/2 \cos(3\theta_n/4) & 1/2 \\ 0 & 0 & 1 \\ -\sqrt{3}/2 \sin(3\theta_a/4) & -\sqrt{3}/2 \cos(3\theta_n/4) & 1/2 \\ -\sqrt{3}/2 \sin(3\theta_a/4) & -\sqrt{3}/2 \cos(3\theta_n/4) & -1/2 \\ 0 & 0 & -1 \\ -\sqrt{3}/2 \sin(3\theta_a/4) & \sqrt{3}/2 \cos(3\theta_n/4) & -1/2 \end{bmatrix}, \quad (\text{A.6})$$

$$\mathbf{T}_2 = \begin{bmatrix} 1/2 \sin(3\theta_a/4) & -1/2 \cos(3\theta_n/4) & \sqrt{3}/2 \\ 0 & -1 & 0 \\ -1/2 \sin(3\theta_a/4) & -1/2 \cos(3\theta_n/4) & -\sqrt{3}/2 \\ 1/2 \sin(3\theta_a/4) & 1/2 \cos(3\theta_n/4) & -\sqrt{3}/2 \\ 0 & 1 & 0 \\ -1/2 \sin(3\theta_a/4) & 1/2 \cos(3\theta_n/4) & \sqrt{3}/2 \end{bmatrix}, \quad (\text{A.7})$$

$$\mathbf{O}_2 = \begin{bmatrix} \cos(3\theta_n/4) & \sin(3\theta_a/4) & 0 \\ 1 & 0 & 0 \\ \cos(3\theta_n/4) & -\sin(3\theta_a/4) & 0 \\ \cos(3\theta_n/4) & -\sin(3\theta_a/4) & 0 \\ 1 & 0 & 0 \\ \cos(3\theta_n/4) & \sin(3\theta_a/4) & 0 \end{bmatrix}. \quad (\text{A.8})$$

Azimuthal angles:

$$\theta_{2n} = (3\theta_a/2, 0, -3\theta_a/2, -3\theta_a/2, 0, 3\theta_a/2). \quad (\text{A.9})$$

Relative phase:

$$\begin{aligned} \beta_{2n} = & (qc + 3\beta\theta_a/2, 2qc, qc - 3\beta\theta_a/2, \\ & -qc - 3\beta\theta_a/2, -2qc, -qc + 3\beta\theta_a/2). \end{aligned} \quad (\text{A.10})$$

Ring 3

Bond triplet:

$$\mathbf{L}_3 = \begin{bmatrix} -1/2 * \sin(\theta_a/2) & 1/2 \cos(\theta_a/2) & \sqrt{3}/2 \\ -\sin(\theta_a) & -\cos(\theta_a) & 0 \\ -1/2 * \sin(\theta_a/2) & 1/2 \cos(\theta_a/2) & -\sqrt{3}/2 \end{bmatrix}, \quad (\text{A.11})$$

$$\mathbf{T}_3 = \begin{bmatrix} \sqrt{3}/2 \sin(\theta_a/2) & -\sqrt{3}/2 \cos(\theta_a/2) & 1/2 \\ \sin(\theta_a/2) & \cos(\theta_a/2) & -1 \\ -\sqrt{3}/2 \sin(\theta_a/2) & \sqrt{3}/2 \cos(\theta_a/2) & 1/2 \end{bmatrix}, \quad (\text{A.12})$$

$$\mathbf{O}_3 = \begin{bmatrix} \cos(\theta_a/2) & \sin(\theta_a/2) & 0 \\ \cos(\theta_a) & -\sin(\theta_a) & 0 \\ \cos(\theta_a/2) & \sin(\theta_a/2) & 0 \end{bmatrix}. \quad (\text{A.13})$$

Azimuthal angles:

$$\theta_{3n} = (\theta_a, -2\theta_a, \theta_a). \quad (\text{A.14})$$

Relative phase:

$$\beta_{3n} = (2qc + \beta\theta_a, -2\beta\theta_a, -2qc + \beta\theta_a). \quad (\text{A.15})$$

Ring 4

Bond Triplet:

$$\mathbf{L}_4 = \begin{bmatrix} -5/2\sqrt{7}\sin(5\theta_a/4) & 5/2\sqrt{7}\cos(5\theta_a/4) & \sqrt{3}/2\sqrt{7} \\ -1/2\sqrt{7}\sin(\theta_a/4) & -1/2\sqrt{7}\cos(\theta_a/4) & \sqrt{3}/2\sqrt{7} \\ -2/\sqrt{7}\sin(\theta_a) & -2/\sqrt{7}\cos(\theta_a) & \sqrt{3}/2\sqrt{7} \\ -2/\sqrt{7}\sin(\theta_a) & -2/\sqrt{7}\cos(\theta_a) & \sqrt{3}/2\sqrt{7} \\ -1/2\sqrt{7}\sin(\theta_a/4) & -1/2\sqrt{7}\cos(\theta_a/4) & \sqrt{3}/2\sqrt{7} \\ -5/2\sqrt{7}\sin(5\theta_a/4) & 5/2\sqrt{7}\cos(5\theta_a/4) & \sqrt{3}/2\sqrt{7} \end{bmatrix}, \quad (\text{A.16})$$

$$\mathbf{T}_4 = \begin{bmatrix} \sqrt{3}/2\sqrt{7}\sin(5\theta_a/4) & \sqrt{3}/2\sqrt{7}\cos(5\theta_a/4) & 5/2\sqrt{7} \\ 3\sqrt{3}/2\sqrt{7}\sin(\theta_a/4) & 3\sqrt{3}/2\sqrt{7}\cos(\theta_a/4) & -1/\sqrt{7} \\ \sqrt{3}/\sqrt{7}\sin(\theta_a) & \sqrt{3}/\sqrt{7}\cos(\theta_a) & -2/\sqrt{7} \\ \sqrt{3}/\sqrt{7}\sin(\theta_a) & \sqrt{3}/\sqrt{7}\cos(\theta_a) & -2/\sqrt{7} \\ 3\sqrt{3}/2\sqrt{7}\sin(\theta_a/4) & 3\sqrt{3}/2\sqrt{7}\cos(\theta_a/4) & -1/\sqrt{7} \\ \sqrt{3}/2\sqrt{7}\sin(5\theta_a/4) & \sqrt{3}/2\sqrt{7}\cos(5\theta_a/4) & 5/2\sqrt{7} \end{bmatrix}, \quad (\text{A.17})$$

$$\mathbf{O}_4 = \begin{bmatrix} \cos(5\theta_a/4) & \sin(5\theta_a/4) & 0 \\ \cos(\theta_a/4) & -\sin(\theta_a/4) & 0 \\ \cos(\theta_a) & -\sin(\theta_a) & 0 \\ \cos(\theta_a) & -\sin(\theta_a) & 0 \\ \cos(\theta_a/4) & -\sin(\theta_a/4) & 0 \\ \cos(5\theta_a/4) & \sin(5\theta_a/4) & 0 \end{bmatrix}. \quad (\text{A.18})$$

Azimuthal angles:

$$\theta_{4n} = (5\theta_a/2, -\theta_a/2, -2\theta_a, -2\theta_a, -\theta_a/2, 5\theta_a/2). \quad (\text{A.19})$$

Relative phase:

$$\begin{aligned} \beta_{4n} = & (qc + 5\beta\theta_a/2, 3qc - \beta\theta_a/2, 2qc - 2\beta\theta_a, \\ & -2qc - 2\beta\theta_a, -3qc - \beta\theta_a/2, -qc + 5\beta\theta_a/2). \end{aligned} \quad (\text{A.20})$$

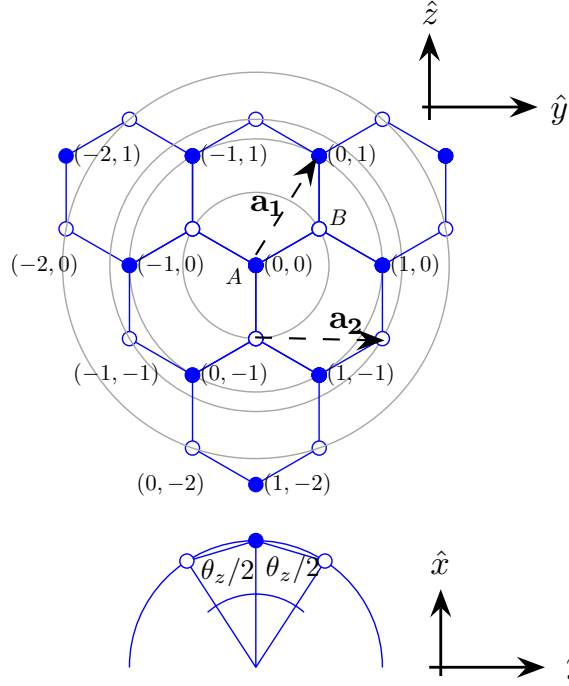


Fig. A.3. Upper panel: unrolled $(n,0)$ tube in the (y,z) . Lower panel: the rolled tube in the (x,y) plane. Here, $\theta_z = 2\pi/n$, $\mathbf{a}_1 = \sqrt{3}a (\cos \frac{\pi}{3}\hat{y} + \sin \frac{\pi}{3}\hat{z})$, $\mathbf{a}_2 = \sqrt{3}a\hat{y}$, and $a = 1.42 \times 10^{-10}m$.

A.1.2 Zigzag tube

Figure A.3 shows the geometry of a zigzag tube. Here we define the angle, $\theta_z = 2\pi/n$ for an $(n,0)$ zigzag tube. Note that, compared to a same diameter armchair tube, $\theta_z = \sqrt{3}\theta_a$.

Ring 1

Bond Triplet:

$$\mathbf{L}_1 = \begin{bmatrix} -\sqrt{3}/2 \sin \theta_z/4 & \sqrt{3}/2 \cos \theta_z/4 & 1/2 \\ -\sqrt{3}/2 \sin \theta_z/4 & -\sqrt{3}/2 \cos \theta_z/4 & 1/2 \\ 0 & 0 & -1 \end{bmatrix}, \quad (\text{A.21})$$

$$\mathbf{T}_1 = \begin{bmatrix} 1/2 \sin \theta_z/4 & -1/2 \cos \theta_z/4 & \sqrt{3}/2 \\ -1/2 \sin \theta_z/4 & -1/2 \cos \theta_z/4 & -\sqrt{3}/2 \\ 0 & 1 & 0 \end{bmatrix}, \quad (\text{A.22})$$

$$\mathbf{O}_1 = \begin{bmatrix} \cos \theta_z/4 & \sin \theta_z/4 & 0 \\ \cos \theta_z/4 & -\sin \theta_z/4 & 0 \\ 1 & 0 & 0 \end{bmatrix}. \quad (\text{A.23})$$

Azimuthal angles:

$$\theta_{1n} = \left(\theta_z/2, \quad -\theta_z/2, \quad 0 \right). \quad (\text{A.24})$$

Relative phase:

$$\beta_{1n} = \left(qa/2 + \beta\theta_z/2, \quad qa/2 - \beta\theta_z/2, \quad -qa \right). \quad (\text{A.25})$$

Ring 2

Bond Triplet:

$$\mathbf{L}_2 = \begin{bmatrix} -\sin \theta_z/2 & \cos \theta_z/2 & 0 \\ -1/2 \sin \theta_z/4 & 1/2 \cos \theta_z/4 & \sqrt{3}/2 \\ -1/2 \sin \theta_z/4 & -1/2 \cos \theta_z/4 & \sqrt{3}/2 \\ -\sin \theta_z/2 & -\cos \theta_z/2 & 0 \\ -1/2 \sin \theta_z/4 & -1/2 \cos \theta_z/4 & -\sqrt{3}/2 \\ -1/2 \sin \theta_z/4 & 1/2 \cos \theta_z/4 & -\sqrt{3}/2 \end{bmatrix}, \quad (\text{A.26})$$

$$\mathbf{T}_2 = \begin{bmatrix} 0 & 0 & 1 \\ \sqrt{3}/2 \sin \theta_z/4 & -\sqrt{3}/2 \cos \theta_z/4 & 1/2 \\ -\sqrt{3}/2 \sin \theta_z/4 & -\sqrt{3}/2 \cos \theta_z/4 & -1/2 \\ 0 & 0 & -1 \\ \sqrt{3}/2 \sin \theta_z/4 & \sqrt{3}/2 \cos \theta_z/4 & -1/2 \\ -\sin \theta_z/4 & \sqrt{3}/2 \cos \theta_z/4 & 1/2 \end{bmatrix}, \quad (\text{A.27})$$

$$\mathbf{O}_2 = \begin{bmatrix} \cos \theta_z/4 & \sin \theta_z/2 & 0 \\ \cos \theta_z/4 & \sin \theta_z/4 & 0 \\ \cos \theta_z/4 & -\sin \theta_z/4 & 0 \\ \cos \theta_z/2 & -\sin \theta_z/2 & 0 \\ \cos \theta_z/4 & -\sin \theta_z/4 & 0 \\ \cos \theta_z/4 & \sin \theta_z/4 & 0 \end{bmatrix}. \quad (\text{A.28})$$

Azimuthal angles:

$$\theta_{2n} = \begin{pmatrix} \theta_z & \theta_z/2 & -\theta_z/2 & -\theta_z & -\theta_z/2 & \theta_z/2 \end{pmatrix}. \quad (\text{A.29})$$

Relative phase:

$$\beta_{2n} = \begin{pmatrix} \beta\theta_z, & 3qa/2 + \beta\theta_z/2, & 3qa/2 - \beta\theta_z/2, \\ -\beta\theta_z, & -3qa/2 - \beta\theta_z/2, & -3qa/2 + \beta\theta_z/2 \end{pmatrix}. \quad (\text{A.30})$$

Ring 3

Bond Triplet:

$$\mathbf{L}_3 = \begin{bmatrix} 0 & 0 & 1 \\ -\sqrt{3}/2 \sin \theta_z/2 & -\sqrt{3}/2 \cos \theta_z/2 & -1/2 \\ -\sqrt{3}/2 \sin \theta_z/2 & \sqrt{3}/2 \cos \theta_z/2 & -1/2 \end{bmatrix}, \quad (\text{A.31})$$

$$\mathbf{T}_3 = \begin{bmatrix} 0 & -1 & 0 \\ 1/2 \sin \theta_z/2 & 1/2 \cos \theta_z/2 & -\sqrt{3}/2 \\ -1/2 \sin \theta_z/2 & 1/2 \cos \theta_z/2 & \sqrt{3}/2 \end{bmatrix}, \quad (\text{A.32})$$

$$\mathbf{O}_3 = \begin{bmatrix} 1 & 0 & 0 \\ \cos \theta_z/2 & -\sin \theta_z/2 & 0 \\ \cos \theta_z/2 & \sin \theta_z/2 & 0 \end{bmatrix}. \quad (\text{A.33})$$

Azimuthal angles:

$$\theta_{3n} = \begin{pmatrix} 0, & -\theta_z, & \theta_z \end{pmatrix}. \quad (\text{A.34})$$

Relative phase:

$$\beta_{3n} = \begin{pmatrix} qa, & -qa - \beta\theta_z, & -qa + \beta\theta_z \end{pmatrix}. \quad (\text{A.35})$$

Ring 4

Bond Triplet:

$$\mathbf{L}_4 = \begin{bmatrix} -\sqrt{27/28} \sin(3\theta_z/4) & \sqrt{27/28} \cos(3\theta_z/4) & \sqrt{1/28} \\ -\sqrt{3/7} \sin(\theta_z/2) & \sqrt{3/7} \cos(\theta_z/2) & \sqrt{4/7} \\ -\sqrt{3/7} \sin(\theta_z/2) & -\sqrt{3/7} \cos(\theta_z/2) & \sqrt{4/7} \\ -\sqrt{27/28} \sin(3\theta_z/4) & -\sqrt{27/28} \cos(3\theta_z/4) & \sqrt{1/28} \\ -\sqrt{3/28} \sin(\theta_z/4) & -\sqrt{3/28} \cos(\theta_z/4) & -\sqrt{25/28} \\ -\sqrt{3/28} \sin(\theta_z/4) & \sqrt{3/28} \cos(\theta_z/4) & -\sqrt{25/28} \end{bmatrix}, \quad (\text{A.36})$$

$$\mathbf{T}_4 = \begin{bmatrix} \cos(3\theta_z/4) & \sin(3\theta_z/4) & 0 \\ \cos(\theta_z/2) & \sin(\theta_z/2) & 0 \\ \cos(\theta_z/2) & -\sin(\theta_z/2) & 0 \\ \cos(3\theta_z/4) & -\sin(3\theta_z/4) & 0 \\ \cos(\theta_z/4) & -\sin(\theta_z/4) & 0 \\ \cos(\theta_z/4) & \sin(\theta_z/4) & 0 \end{bmatrix}, \quad (\text{A.37})$$

$$\mathbf{O}_4 = \begin{bmatrix} \sqrt{1/28} \sin(3\theta_z/4) & -\sqrt{1/28} \cos(3\theta_z/4) & \sqrt{27/28} \\ \sqrt{4/7} \sin(\theta_z/2) & -\sqrt{4/7} \cos(\theta_z/2) & \sqrt{3/7} \\ -\sqrt{4/7} \sin(\theta_z/2) & -\sqrt{4/7} \cos(\theta_z/2) & -\sqrt{3/7} \\ -\sqrt{1/28} \sin(3\theta_z/4) & -\sqrt{1/28} \cos(3\theta_z/4) & -\sqrt{27/28} \\ \sqrt{25/28} \sin(\theta_z/4) & \sqrt{25/28} \cos(\theta_z/4) & -\sqrt{3/28} \\ -\sqrt{25/28} \sin(\theta_z/4) & \sqrt{25/28} \cos(\theta_z/4) & \sqrt{3/28} \end{bmatrix}. \quad (\text{A.38})$$

Azimuthal angles:

$$\theta_{4n} = \left(3\theta_z/2, \theta_z, -\theta_z, -3\theta_z/2, -\theta_z/2, \theta_z/2 \right). \quad (\text{A.39})$$

Relative phase:

$$\beta_{4n} = \left(3\beta\theta_z/2, 2qa + \beta\theta_z, 2qa - \beta\theta_z, \right. \\ \left. -3\beta\theta_z/2, -2qa - \beta\theta_z/2, -2qa + \beta\theta_z/2 \right). \quad (\text{A.40})$$

A.2 Bond Deformation

Using the above unit vectors, the deformations of the 18 bonds along the 3 directions (a total of 54 interaction terms) can be calculated. Consider the first atom on the first NN, the bond deformation of which can be written as

$$\begin{aligned}\delta\ell_{11} &= \hat{\ell}_1 \cdot (Q_{B1} - Q_A) \\ &= \ell_{r1i} (U_{1ij} Q_{B1j} - Q_{Aj}) \\ &= \mathbf{L}_{11} \mathbf{U}_1 \mathbf{Q}_{B1} - \mathbf{L}_{11} \mathbf{Q}_A,\end{aligned}\tag{A.41}$$

$$\delta t_{11} = \mathbf{T}_{11} \mathbf{U}_1 \mathbf{Q}_{B1} - \mathbf{T}_{11} \mathbf{Q}_A,\tag{A.42}$$

$$\delta o_{11} = \mathbf{O}_{11} \mathbf{U}_1 \mathbf{Q}_{B1} - \mathbf{O}_{11} \mathbf{Q}_A.\tag{A.43}$$

Here, \mathbf{L}_{11} is the first row of the \mathbf{L}_1 matrix and so on. Also summation over repeated subscripts are assumed above. The $\mathbf{U}_1 = \mathbf{U}(\theta_{11})$ is the rotation matrix that converts the local cylindrical coordinate at \mathbf{R}_{B1} to the cartesian system. This transformation is given by (Eq. (2.12))

$$\mathbf{U}(\theta) = \begin{pmatrix} \cos \theta & -\sin \theta & 0 \\ \sin \theta & \cos \theta & 0 \\ 0 & 0 & 1 \end{pmatrix}.\tag{A.44}$$

To calculate this rotation matrix, U_{nij} , for the n^{th} atom on a particular ring, the phase angles defined before are used. To simplify the calculation of the dynamical matrix, we define

$$\Lambda_{rni} = L_{rni} U_{ij}(\theta_{rn})\tag{A.45}$$

$$\Theta_{rni} = T_{rni} U_{ij}(\theta_{rn})\tag{A.46}$$

$$\Omega_{rni} = O_{rni} U_{ij}(\theta_{rn}),\tag{A.47}$$

where, r stands for r^{th} NN ring, n is the n^{th} atom of that ring, and θ_{rn} is the azimuthal angle of the n^{th} atom.

A.3 Potential Energy

To calculate the net force on each atom, we first calculate the potential energy of atom A due to the deformation of its 18 bonds. Using the following force constants for each NN

$$\begin{aligned} K_r^\ell &= (365.0, \ 88.0, \ 30.0, \ -19.20) \text{ N/m} \\ K_r^t &= (245.0, \ -32.3, \ -52.5, \ 11.34) \text{ N/m} \\ K_r^o &= (98.2, \ -4.0, \ 1.5, \ -5.80) \text{ N/m}, \end{aligned}$$

where, K_1^ℓ , is the ℓ component of the force-constant tensor for the first NN ring.

A.3.1 Ring 1, 3, 4

For an n^{th} atom on r^{th} ring ($r \in (1, 3, 4)$) the deformation to a particular q, β phonon mode is

$$\begin{aligned} \delta\ell_{rn} &= \Lambda_{rnj} e^{i\beta_{rn}} Q_{Bj} - L_{rnj} Q_{Aj} \\ &= [-L_{rnj}, \ \Lambda_{rni} e^{i\beta_{rn}}] \begin{pmatrix} Q_{Aj} \\ Q_{Bj} \end{pmatrix} \\ &= M_{rnj}^\ell Q_j, \end{aligned} \tag{A.48}$$

where, β_{rn} is the phase angle of the neighboring atoms, which have been determined previously, $M_{rnj}^\ell \equiv [-L_{rnj}, \ \Lambda_{rni} e^{i\beta_{rn}}]$, and $Q_j = (Q_{A\rho}, Q_{A\theta}, Q_{Az}, Q_{B\rho}, Q_{B\theta}, Q_{Bz})^T$.

Potential energy of atom A due to this deformation is

$$\begin{aligned} U_{A,134} &= \sum_{r=1,3,4} \frac{1}{2} K_r^\ell \delta\ell_{rn} \delta\ell_{rn}^\dagger + \frac{1}{2} K_r^t \delta t_{rn} \delta t_{rn}^\dagger + \frac{1}{2} K_r^o \delta o_{rn} \delta o_{rn}^\dagger \\ &= \sum_{r=1,3,4} \frac{1}{2} K_r^\ell \mathbf{Q}^\dagger \mathbf{M}_r^{\ell\dagger} \mathbf{M}_r^\ell \mathbf{Q} + \frac{1}{2} K_r^t \mathbf{Q}^\dagger \mathbf{M}_r^{t\dagger} \mathbf{M}_r^t \mathbf{Q} + \frac{1}{2} K_r^o \mathbf{Q}^\dagger \mathbf{M}_r^{o\dagger} \mathbf{M}_r^o \mathbf{Q} \\ &= \sum_{r=1,3,4} \frac{1}{2} \mathbf{Q}^\dagger [K_r^\ell \mathbf{M}_r^{\ell\dagger} \mathbf{M}_r^\ell + K_r^t \mathbf{M}_r^{t\dagger} \mathbf{M}_r^t + K_r^o \mathbf{M}_r^{o\dagger} \mathbf{M}_r^o] \mathbf{Q}, \end{aligned} \tag{A.49}$$

where, for particular a NN ring, r , the matrix \mathbf{M}_r^ℓ is created by stacking the row vectors $[-L_{rnj}, \Lambda_{rni}e^{i\beta_{rn}}]$ for each bond on r^{th} . Matrices, \mathbf{M}_r^t and \mathbf{M}_r^o are created similarly. Defining,

$$\mathcal{D}_{\mathbf{A},134} \equiv [K_r^\ell \mathbf{M}_r^{\ell\dagger} \mathbf{M}_r^\ell + K_r^t \mathbf{M}_r^{t\dagger} \mathbf{M}_r^t + K_r^o \mathbf{M}_r^{o\dagger} \mathbf{M}_r^o] \quad (\text{A.50})$$

we get,

$$U_{A,134} = \frac{1}{2} \mathbf{Q}^\dagger \mathcal{D}_{\mathbf{A},134} \mathbf{Q}. \quad (\text{A.51})$$

Since, the A and B atoms are symmetric, their energy are also same, thus, $\mathcal{D}_{A,134} = \mathcal{D}_{B,134}$.

A.3.2 Ring 2

For ring 2, the nearest neighbors are also of type A, and the bond deformation is

$$\begin{aligned} \delta\ell_{2n} &= \Lambda_{2nj}e^{i\beta_{2n}}Q_{Aj} - L_{2nj}Q_{Aj} \\ &= [-L_{2nj} + \Lambda_{2ni}e^{i\beta_{2n}}]Q_{Aj}, \\ &= M_{2nj}^\ell Q_{Aj}. \end{aligned} \quad (\text{A.52})$$

Thus 2NN deformation potential of atom A does not couple with the motion of atom B. Similarly the potential energy due to 2NN deformation of atom B does not involve atom A. Thus potential energy due to 2NN deformation is

$$U_{A,2} = \frac{1}{2} \mathbf{Q}_A^\dagger \mathcal{D}_0 \mathbf{Q}_A, \quad (\text{A.53})$$

$$U_{B,2} = \frac{1}{2} \mathbf{Q}_B^\dagger \mathcal{D}_0 \mathbf{Q}_B, \quad (\text{A.54})$$

where,

$$\mathcal{D}_0 \equiv [K_2^\ell \mathbf{M}_2^{\ell\dagger} \mathbf{M}_2^\ell + K_2^t \mathbf{M}_2^{t\dagger} \mathbf{M}_2^t + K_2^o \mathbf{M}_2^{o\dagger} \mathbf{M}_2^o]. \quad (\text{A.55})$$

In order to use the combined phonon coordinate, \mathbf{Q} , we define $\mathcal{D}_{\mathbf{A},2}$ and $\mathcal{D}_{\mathbf{B},2}$ in the following way

$$\mathcal{D}_{\mathbf{A},2} = \begin{bmatrix} \mathcal{D}_0 & \mathbf{0} \\ \mathbf{0} & \mathbf{0} \end{bmatrix}, \quad \mathcal{D}_{\mathbf{B},2} = \begin{bmatrix} \mathbf{0} & \mathbf{0} \\ \mathbf{0} & \mathcal{D}_0 \end{bmatrix}. \quad (\text{A.56})$$

Now the potential energy expression becomes

$$U_{A,2} = \frac{1}{2} \mathbf{Q}^\dagger \mathcal{D}_{A,2} \mathbf{Q}, \quad (\text{A.57})$$

$$U_{B,2} = \frac{1}{2} \mathbf{Q}^\dagger \mathcal{D}_{B,2} \mathbf{Q}. \quad (\text{A.58})$$

A.4 Dynamical Matrix

To calculate the force on the unit cell, we first calculate the total potential energy of the unit cell due to interaction with the 4NNs. This is

$$\begin{aligned} U &= (U_{A,123} + U_{B,123}) + U_{A,2} + U_{B,2}, \\ &= \frac{1}{2} \mathbf{Q}^\dagger [\mathcal{D}_{A,134} + \mathcal{D}_{B,134} + \mathcal{D}_{A,2} + \mathcal{D}_{B,2}] \mathbf{Q}, \\ &= \mathbf{Q}^\dagger \left[\mathcal{D}_{A,134} + \frac{1}{2} \mathcal{D}_{A,2} + \frac{1}{2} \mathcal{D}_{B,2} \right] \mathbf{Q}. \end{aligned} \quad (\text{A.59})$$

The force along one of the 6 phonon coordinates, j , can be obtained by $-\partial U / \partial Q_j^\dagger$ [88]. Here these directions are along: $\mathbf{u}_{A\rho}$, $\mathbf{u}_{A\theta}$, $\mathbf{u}_{A\mathbf{z}}$, $\mathbf{u}_{B\rho}$, $\mathbf{u}_{B\theta}$, and $\mathbf{u}_{B\mathbf{z}}$. Thus total force

$$\begin{aligned} \mathcal{F} &= - \left[\mathcal{D}_{A,134} + \frac{1}{2} \mathcal{D}_{A,2} + \frac{1}{2} \mathcal{D}_{B,2} \right] \mathbf{Q}, \\ &= -\mathcal{D}(q, \beta) \mathbf{Q}, \end{aligned} \quad (\text{A.60})$$

here,

$$\mathcal{D}(q, \beta) = \left[\mathcal{D}_{A,134} + \frac{1}{2} \mathcal{D}_{A,2} + \frac{1}{2} \mathcal{D}_{B,2} \right], \quad (\text{A.61})$$

is the dynamical matrix.

A.5 Phonon Dispersion

Applying Newton's law on the unit cell, and putting, $\mathbf{Q}(\mathbf{t}) = \mathbf{Q}_\omega e^{-i\omega t}$, we get

$$\begin{aligned} m_c \frac{d^2}{dt^2} \mathbf{Q}(\mathbf{t}) &= \mathcal{F} = -\mathcal{D}(\mathbf{q}, \beta) \mathbf{Q}(\mathbf{t}), \\ m_c \omega^2 \mathbf{Q}_\omega &= \mathcal{D}(\mathbf{q}, \beta) \mathbf{Q}_\omega. \end{aligned} \quad (\text{A.62})$$

Eigenvalues and eigenvectors of the above equation are the phonon dispersion and the phonon polarization. To facilitate analysis it is convenient to define the following unitary transformation

$$U_{cm} = \frac{1}{\sqrt{2}} \begin{bmatrix} 1 & & & 1 & & \\ & 1 & & & 1 & \\ & & 1 & & & 1 \\ 1 & & & -1 & & \\ & 1 & & & -1 & \\ & & 1 & & & -1 \end{bmatrix}, \quad (\text{A.63})$$

which, transforms the phonon coordinates to its center of mass ('cm') coordinates. The new coordinates are defined as

$$\text{RBM: } Q_\rho = (Q_{A\rho} + Q_{B\rho}) / \sqrt{2}$$

$$\text{TW: } Q_\theta = (Q_{A\theta} + Q_{B\theta}) / \sqrt{2}$$

$$\text{LA: } Q_z = (Q_{Az} + Q_{Bz}) / \sqrt{2}$$

$$\text{oRBM: } q_\rho = (Q_{A\rho} - Q_{B\rho}) / \sqrt{2}$$

$$\text{TO: } q_\theta = (Q_{A\theta} - Q_{B\theta}) / \sqrt{2}$$

$$\text{LO: } q_z = (Q_{Az} - Q_{Bz}) / \sqrt{2}.$$

Here, the first three modes are acoustic modes, and the last three are optical modes. Inserting this transformation in Eq. (A.4) we obtain

$$\begin{aligned} m_c \omega^2 \mathbf{U}_{\text{cm}}^\dagger \mathbf{U}_{\text{cm}} \mathbf{Q}_\omega &= \mathbf{U}_{\text{cm}}^\dagger \mathbf{U}_{\text{cm}} \mathcal{D} \mathbf{U}_{\text{cm}}^\dagger \mathbf{U}_{\text{cm}} \mathbf{Q}_\omega \\ m_c \omega^2 \{ \mathbf{U}_{\text{cm}} \mathbf{Q}_\omega \} &= \mathbf{U}_{\text{cm}} \mathcal{D} \mathbf{U}_{\text{cm}}^\dagger \{ \mathbf{U}_{\text{cm}} \mathbf{Q}_\omega \}. \end{aligned} \quad (\text{A.64})$$

This is the eigenvalue equation that we solve to obtain phonon dispersion in carbon nanotubes.

VITA

VITA

Sayed Hasan was born in 1974, in Dhaka, Bangladesh. He received his B.Sc. in Electrical and Electronic Engineering (EEE) from Bangladesh University of Engineering and Technology (BUET) in 1998. After serving two years as a lecturer in the department of EEE, at BUET, he joined the department of ECE, Purdue University, West Lafayette, IN, as a direct Ph.D. student. After graduating from Purdue, he will join the device research group at Texas Instruments, Dallas, Texas.